Computational fluid dynamics - A clinician's tool for femoral artery stenosis?

A DISSERTATION PRESENTED

BY

LENNART VAN DE VELDE

TO

THE DEPARTMENT OF SCIENCE & TECHNOLOGY

IN PARTIAL FULFILLMENT OF THE REQUIREMENTS

FOR THE DEGREE OF

MASTER OF SCIENCE

IN THE SUBJECT OF

TECHNICAL MEDICINE

UNIVERSITY OF TWENTE

ENSCHEDE, THE NETHERLANDS

FEBRUARY 2018

Thesis advisors: prof. AM Versluis, dr. MMPJ Reijnen Lennart van de Velde

Computational fluid dynamics - A clinician's tool for femoral artery stenosis?

Abstract

Occlusive disease of the femoral artery is a frequent cause of disabling muscle pain during walking and may progress to non-healing skin ulcers of the foot and leg. The underlying disease process, atherosclerosis, is related to the shearing stress of blood on the vessel wall. One way to assess blood's motion near the vessel wall is by computational fluid dynamics (CFD), in which the governing equations of blood flow are solved by numerical techniques. The application of CFD in clinical decision making has thus far been limited mainly to coronary artery stenosis. This thesis presents translational work to assess the potential use of CFD in the diagnosis and treatment of femoral artery stenosis. Two applications are investigated: (1) quantification of the pressure drop over tandem stenoses of varying shapes, and (2) the prediction of stent thrombolization in the Viabahn covered stentgraft in patient-specific geometries.

The SimVascular finite element solver was used with CTA-based flow geometries and duplex ultrasound derived boundary conditions. Validation of the simulations in a femoral bifurcation with and without an upstream 75% stenosis demonstrated velocity fields that matched well with experimental flow visualization for the majority of the cycle, with deviations in jet breakdown and flow reversal that need further investigation. Steady flow simulations in serial stenoses of idealized geometries showed a pronounced contribution of stenosis eccentricity, in contrast to an earlier experiment performed at lower Reynolds numbers. The relative rotation of two serial eccentric lesions was additionally shown to augment the pressure drop if it induced strong helical flows. For stent thrombolization, unsteady flow simulations in one retrospective patient case showed a region of low wall shear stress at the inflow region of the stent, while CTA and duplex had shown no abnormalities. Occlusion of the stentgraft was observed half a year later, highlighting the potential ability of CFD to predict stentgraft complications. The results warrant the application of CFD in prospective cohort studies of patients with peripheral artery disease to generate clinical evidence needed for improved decision making.

Contents

Listing of figures

This thesis is dedicated to my parents.

Acknowledgments

Little did I know. When I started working on this thesis, my experience with computational fluid dynamics was limited to a theoretical course in finite difference methods. I grew fascinated by applying these flow simulation techniques in medicine, knowing that I was to face significant challenges. What I did not know was how fortunate I was to be hosted by two excellent research groups at Ghent University and Stanford university in the past year. Without the lessons I learned there, this thesis would have been discussing many procedural and technical difficulties, instead of the present, more clinical focus.

Charlotte, thank you for your guidance and interactive lectures on image-based hemodynamical simulations. You have made my stay in Ghent both a tremendously useful and enjoyable one. Federico, Darya, Mathias, Viviana, Alessio, thanks for answering my many questions. And for inviting me to join the mixed Italian/FEops soccer team, it was a blast. Prof. Joris Degroote, thanks for your inspiring lectures on fluid-structure interaction. Prof. Patrick Segers, thank you for hosting me at biommeda and for your useful advice.

Alison, it was a great pleasure to visit your lab in Stanford and get to know part of the team behind SimVascular. You have been very generous in hosting me and your contributions to cardiovascular modeling are phenomenal. Justin and Aekaansh, thank you both for a crash course in cluster communication. Gabriel, thanks for introducing me to Stanford life and the Dutch community, I hope your machine learning efforts will end up serving patients well. Jan-Renier and Wieneke, thank you for showing me around Stanford, the Bay area, as well as to the other, minuscule side of atherosclerosis, the endothelial cells in your lab. Hopefully our research efforts into wall shear stress and atherosclerosis will augment one another. Finally, Hongzhi, a tremendous thanks for your patience and help with compiling SimVascular on our cluster at Twente University. Similarly, Bas and Vamzi, thanks for your help with using the cluster.

While abroad, work at the Twente flowlab did not stop and I owe a great deal of thanks to Jeanette, Marije and Tom. Your hard work for improving the casting process of arterial phantoms has made the validation chapter possible. Not to mention lab technicians Henny en Gerben, without your never-ending help I would not even have been able to solder a connector of a flow sensor, let alone 3D-print stenotic geometries.

Back home at the Rijnstate hospital in the Netherlands, I thoroughly enjoyed participating in

surgery operations and endovascular interventions, as well as learning how to acquire a patient's medical history at the inpatient and outpatient clinic. Luuk, Steven, Jan-Willem, Cora, and all surgical residents, your willingness to share your expertise has greatly augmented my clinical knowledge, thanks a lot.

Michel, your relentless spirit for innovation in surgery never fails to motivate me. Your comments are always to the point and have done a great job in keeping me on track. Thank you for your enthusiastic support and guidance, both in research and in the clinic. Erik, during our weekly Skype calls when I was abroad, you have done a great job in helping me keep focus. Back home, I thoroughly enjoyed our days as lab partners in crime. Michel, your questions on flow physics have been very useful by regularly exposing me to new perspectives on a problem. Besides, your contacts in the field and swift response in relation to administrative paperwork has made my foreign visits possible, for which I am very grateful.

I gratefully acknowledge the Netherlands Heart Foundation for supporting my research abroad, as well as for allowing me to present part of the results at the VEITH Vascular symposium in New York.

Mom, dad, I dedicate this work to you. You have always encouraged me to explore the world around me and supported me in everything I do. The same goes for my brother.

Last of all, Stefan, you've been a fantastic help with cover design and proofreading for this thesis. Your comments were both useful and hilarious. But most of all, I have very much enjoyed our talks in the past year on life, the universe and everything else. Let's keep them flowing!

0 Introduction

Occlusive disease of the arteries supplying the lower limbs is a major health issue for the elderly in developed countries. In the Netherlands, roughly 1 out of 5 of individuals aged 65 and older have a significant obstruction in one of the arteries that supply the legs.[1] Within this group, 1 out of 10 individuals experience muscle pain when walking a few hundred meters or less, of which a subset develops critical limb ischemia. Moreover, these individuals have a 4x higher risk on cardiac arrest and stroke compared to the general elderly population.[2] The basis for this increased risk is the common disease process atherosclerosis, which typically develops in a select set of arteries that includes the arteries supplying the heart, the brain and the legs.

Atherosclerosis refers to the formation of plaques at the inner vessel wall, which grow slowly over the years and can gradually impede bloodflow to the organs mentioned. The localization of atherosclerosis is intrinsically linked with the local behavior of blood's motion at these sites. Visualizing how a fluid like blood flows on a local scale is challenging, both with our own eyes and with more advanced imaging equipment. Accomplishing this task in a clinical setting is nonetheless a key step in improving our ability to predict the progression of the disease and to advance the success of its treatment. In the last decade, the rise of endovascular treatment options has greatly benefited patient comfort, as these procedures are far less invasive for the patient than traditional surgery. However, the endovascular devices that are deployed have a rather high failure rate and more often require additional interventions compared to surgery. Also here, the manner in which stents interact with local blood flow seems to play a key role. For understanding these interactions and anticipating them, it is imperative to develop novel methods of local blood flow visualization suitable for clinical use.

Owing to collaborations between clinicians and engineers with a fluid mechanical background, exciting developments in this field are currently ongoing. These include the use of ultrasound and magnetic resonance imaging, and computational tools to simulate the motion of blood on a local level. The field of computational fluid dynamics (CFD) deals with the latter, which employs simulation techniques that are in long-standing use for the design of aircraft and vehicles. Efforts to translate the use of this technique to the field of surgery have been ongoing, but a major challenge is that its application requires both an appreciable understanding of the technical complexities involved, as well as affinity with the clinical situation at hand. This thesis is an effort to bridge expertise from both worlds to develop a tool that has potential for clinical applicability, to subsequently apply it to three questions relevant to occlusive disease of the femoral artery.

Organization of this thesis is as follows. The first chapter introduces the clinical aspects of peripheral artery disease, its relation with local blood flow patterns, the physics of blood's motion and an introduction to the field of computational fluid dynamics. In the second chapter, a pipeline for clinical CFD simulations is outlined, which has been largely inspired by counseling the expertise from biomedical CFD labs at Ghent and Stanford university. The third chapter compares the predictions of the CFD pipeline with experimental flow visualization techniques in a laboratory setting, as well as detailing the highly pulsatile flow through idealized geometries of a normal and stenosed femoral bifurcation.

The subsequent two chapters address the investigation of two clinical questions with CFD simulations. Chapter 4 addresses how two arterial stenoses in close proximity interact in idealized geometries under steady flow, representative of patients with critical limb ischemia. Chapter 5 reports on a pilot study that aims to elucidate the mode of failure of a covered stentgraft in the superficial femoral artery. Simulations of two patient-specific geometries are presented that demonstrate CFD's ability to predict complications and the possibility of simulating the altered hemodynamics after a virtual intervention. The final two chapters explore other potential applications of CFD in vascular surgery and conclude on the lessons learned.

1 Background

Cardiovascular disease is the world's leading cause of death, accounting for 31% of global mortality in 2015 (WHO annual report 2017). The prime pathophysiologic mechanism is blockage of blood flow by atherosclerotic plaques. Risk factors for plaque formation either function on a systemic or local level. Systemic risk factors are well-known and include lifestyle and aging. Local risk factors relate to the interactions between blood and the arterial wall, and it is here that the near-wall movement of blood plays a central role. This work centralizes on quantification of blood flow through computational means in a specific site of atherosclerotic disease, the femoral artery. The primary goal is to assess the potential of computational simulations in the diagnosis and treatment of femoral artery disease. This chapter will therefore review contemporary diagnostic and treatment techniques for femoral artery disease, arterial fluid mechanics relevant to atherosclerosis and a brief introduction to computational fluid dynamic techniques for blood flow.

1.1 Femoral artery occlusive disease

Occlusive disease that partially or fully obstructs one of the arteries that supply the leg is defined as peripheral artery disease, or PAD. The sites where occlusion most often leads to clinical symptoms are the iliac and femoral arteries. Individuals experiencing symptoms in the Netherlands are commonly scored with the Fontaine classification (the Rutherford classification[3] is more common in other countries). Symptoms usually start with claudicatio intermittens, which refers to muscle pain during exercise (Fontaine II). The muscles involved depend on the artery effected, with the calf muscle most often giving complaints due to occlusive disease of the superficial femoral artery

that supplies the lower leg. The evolution of the disease typically involves the narrowing of existing lesions or the onset of new plaques on the one hand, and the recruitment of new collateral arterial pathways on the other hand. The symptoms may worsen to a stage of critical limb ischemia, which is incrementally categorized as muscle pain during rest (Fontaine III) or the presence of non-healing wounds due to insufficient blood supply (Fontaine IV).

The prime diagnostic for PAD is the ankle-brachial index (ABI), which is measured by taking the ratio of systolic blood pressure at the ankle compared to the arm. An ABI lower than 0.9 is the clinical definition of PAD,[4] although 50-75% of patients with an ABI lower than 0.9 are asymptomatic and fall under the Fontaine I category.[5,6] Patients with PAD have a significantly increased morbidity and mortality from concurrent coronary and cerebrovascular disease (annual event rate of 5-7%[4]), and are therefore referred for cardiovascular risk management through lifestyle changes and drug treatment.

For patients with intermittent claudication supervised walking exercise is the most cost-effective treatment. It helps patients in significantly extending their pain-free walking distance by a factor of 2-4x, and for the majority of patients no additional invasive treatment is needed.[6] Exercise benefits several pathophysiologic mechanisms in PAD, including muscle metabolism, endothelial vasodilator function and gait biomechanics.[7] For patients whose symptoms remain disabling after exercise treatment, or those with more severe symptoms in the Fontaine III and IV groups, revascularization through surgical or endovascular therapy is indicated.[6]

The first step in treatment decision is locating the lesion(s) and quantifying its severity. Diagnostic modalities include duplex ultrasound and contrast enhanced CT or MRI-scanning, as well as invasive angiography for complex cases. Duplex ultrasound is the only modality able to directly assess hemodynamic severity of a stenosis by quantifying its effect on peak velocity and is therefore the first choice in centers with experienced vascular ultrasonographers.[5] If reliable ultrasound investigation of the trajectory of interest is not possible, or if precise measurements of arterial anatomy are needed for endovascular stenting, a CT scan with intravascular contrast is usually made. The choice between a surgical repair involving open cutdown of the artery or endovascular repair depends on many factors and frequently evolves over time, as innovation in endovascular devices is rapid. Currently for the femoral artery, plaques located in the common femoral artery or at its bifurcation are generally treated through a surgical endarterectomy, and plaques in the superficial artery generally through endovascular ballooning and stenting.[8] If for the latter endovascular techniques are contraindicated or fail due to stent occlusion, a more invasive surgical bypass with autologous or synthetic material may be necessary to restore blood supply to the lower extremity. The most notable recent endovascular achievements in the superficial femoral artery are the patency rates of the closed-cell bare metal Supera stent,[9] the drug-eluting Zilver PTX stent,[10] both for stenotic lesions, as well as the covered Viabahn stent for long and fully occluded lesions.[11] Still, even for these best-in-class

treatments, after one year about one out of five treated lesions show restenosis in or near the stented region, possibly due to blood's flow dynamics in the stented region.[12]

1.2 Pathophysiology

Atherosclerosis is a complicated and chronic disease of the arterial wall, spanning the fields of biology, fluid mechanics and a variety of medical specialisms. Current concepts of the initiation of plaque development postulate an initial qualitative change of the endothelial cells lining the inner wall surface, after which they express adhesion molecules that capture leukocytes on their surfaces. These may develop into macrophages, which can start a complicated process of lipid uptake from blood, vessel wall inflammation and interaction with smooth muscle cells.[13] Plaque formation is not uniformly found throughout the arterial system, but in four major sites (Fig. 1.1a: the coronary arterial bed, the carotid arteries, visceral branches of the aorta, and the distal abdominal aorta and its peripheral arteries.)[14]

The preferential localization of atherosclerosis is linked to the role of hemodynamics.[17] In figure 1.1b, the flow through a carotid bifurcation model during systole is shown by hydrogen bubble flow visualization. It is at the outer side of the bifurcation where plaques commonly develop (white arrows), which is thought to be due to relative flow stasis and a lack of flow directionality in this region. These flow features are also observed in other preferential locations near branches, bifurcations and curvature (Fig. 1.1a). Two parallel pathways have been considered to relate the regions of flow stasis to the pathophysiology of atherosclerosis: the prolonged residence time of particles like lipids and white blood cells near the wall[18] and the shearing stress of blood on endothelial cells[19,20]. This wall shear stress (WSS) is defined as

$$\boldsymbol{\tau}_{\mathbf{w}} = \mu(\dot{\gamma})\frac{\partial \boldsymbol{V}}{\partial \boldsymbol{r}} \tag{1.1}$$

with μ blood's viscosity, $\boldsymbol{V}$ blood's velocity parallel to the wall and $\boldsymbol{r}$ the inward radial direction from the wall. Blood's viscosity is generally strain-rate $\dot{\gamma}$ dependent, making it a non-Newtonian fluid. Graphically, WSS equals the slope or derivative of the velocity curve at the wall in figure 1.2. In-vitro studies have strenghtened support for the contribution of hemodynamics to atherogenesis by showing that endothelial cells change their alignment and morphology in response to wall shear stress. Endothelial cells exposed to a uniform wall shear stress show a stretched alignment in the direction of flow, whereas in the absence of a dominant shear direction they take on a round shape and show a more rapid cell turnover. Moreover, in the presence of uniform wall shear stress of physiologic levels, the cells express genes known to be atheroprotective. Physiologic in-vivo levels of arterial WSS are not well-defined with the lack of sensitive measurement methods, but are suggested to be in the range of 1-7 Pa.[16] The relationship between wall shear stress and in-vivo plaque forma-

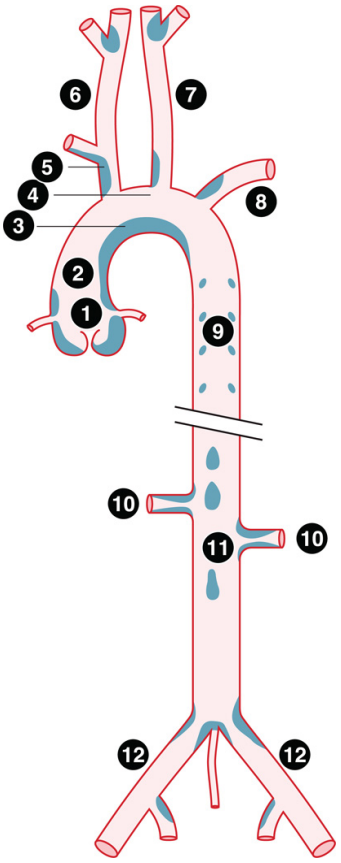

(a) Preferential sites of atherosclerosis

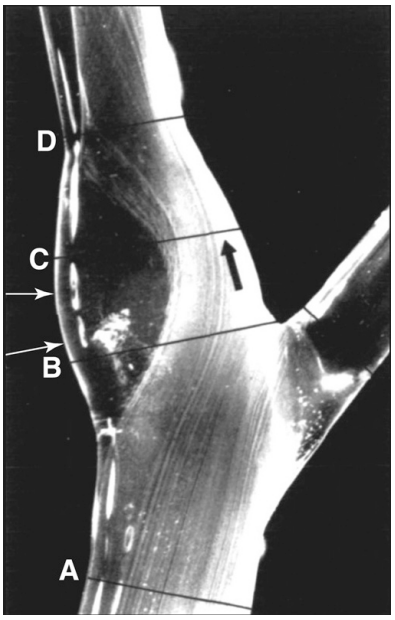

(b) Flow in a carotid bifurcation

Figure 1.1: Arterial fluid mechanics and atherosclerosis. Reproduced from Ku & Giddens [15] and Chiu & Chien [16]

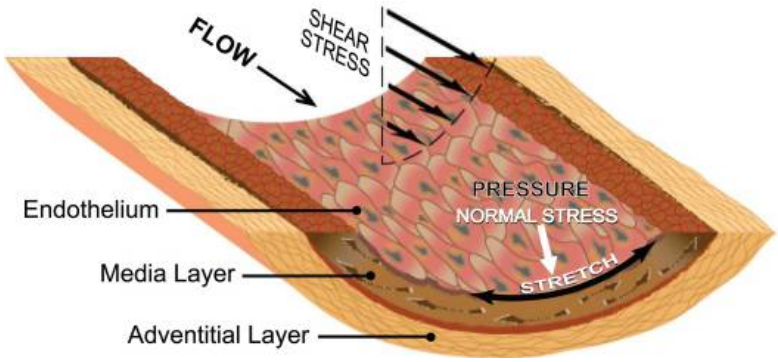

Figure 1.2: Wall shear stress is the shearing force of the moving blood on the endothelial cells of the blood wall. [16]

tion and progression warrants further research, however. [21] Large-scale population studies are needed to generate in-vivo evidence, but these studies remain unfeasible until an easy and reliable method of measuring wall shear stress in patients has been established.

Of the peripheral arteries, the superficial femoral artery is particularly susceptible to atherosclerosis, especially at its origin downstream of the femoral bifurcation and at its trajectory through the adductor channel. Flow in the peripheral arteries is normally triphasic with a substantial part of the cycle showing backflow, [22] which in general causes continuous and strong oscillation in the direction of wall shear stress, an important feature that differentiates it from other common sites like the coronary and carotid arteries. For the femoral bifurcation, similar regions of fluid stasis as in the carotid bifurcation (Fig. 1.1b) are a likely initiation site of atherosclerosis, but flow patterns here have not yet been experimentally visualized in high resolution. The second common site, its trajectory through the adductor channel, does not appear to be related to more frequent localized plaque formation, but more so to the inability for the vessel wall to compensatorily enlarge in diameter in this region. [23,24] Besides, the superficial femoral artery is characterized by a high degree of tortuosity and curvature, especially in men, which may also contribute to adverse flow profiles. [25]

1.3 Arterial fluid dynamics

The cardiovascular system is comprised of many intertwining physical phenomena on a breadth of spatial scales. The cardiac pump creates a highly pulsatile flow coordinated by electrophysiologic and myocardial stress-strain relationships. The pulsatile energy is spread throughout the arterial system, which adaptively distributes blood to target organs and, through its capacitative properties, transforms the pulsatile energy in a more constant perfusion pressure of end organs. Blood, the transported medium, is a mix of water, red blood cells, platelets, proteins and many other substances that may interact with the vessel wall. The clinical area of interest dictates the relevance of each of

these topics. For the development of atherosclerotic disease, the relation between atherosclerosis and local blood flow justifies a focus on local mechanical interaction between blood and the vessel wall. An overview of the fluid mechanics relevant to velocity patterns in blood flow will therefore be given, with some examples for curved and bifurcating arteries.

When studying the motion of a fluid on large scales, the principles of conservation of mass and momentum form the general analysis framework. Along with the constitutive equation for a Newtonian fluid, for which shear stress equals a constant viscosity times the shear rate, Claude Louis Navier and George Edward Stokes independently derived the momentum equation for fluids. Combined with the conservation of mass these form the Navier-Stokes equations for an incompressible, Newtonian fluid

$$\begin{aligned} \rho\frac{\partial \boldsymbol{v}}{\partial t} + \rho\boldsymbol{v}\cdot\nabla\boldsymbol{v} &= \mu\triangle\boldsymbol{v} + \nabla p + \boldsymbol{g} \\ \nabla\cdot\boldsymbol{v} &= 0 \end{aligned} \tag{1.2}$$

with ρ the fluid density, $\boldsymbol{v}$ the fluid velocity, t time, μ the fluid's dynamic viscosity, p the pressure and $\boldsymbol{g}$ the external body force. The upper equation represents conservation of momentum, the lower conservation of mass. The first is best understood as Newton's second law of motion ($F = m\frac{\partial v}{\partial t}$) applied to a fluid volume, with pressure and body force per volume included in the force term, and the left-hand side representing both time and spatial changes in fluid momentum. The spatial change in fluid momentum is often referred to as convective acceleration and occurs for instance when blood flows through a stenosis, where the lumen area decreases and blood velocity has to increase to satisfy the momentum and mass conservation.

Two results of dimensional analyses are particularly relevant for the pulsatile nature of blood flow. The first is the well-known Reynolds number, which relates the size of inertial effects to the fluid's viscous effects

$$\mathrm{Re} = \frac{\text{inertial effects}}{\text{viscous effects}} = \frac{\rho v}{\mu/L} = \frac{vD}{\nu} \tag{1.3}$$

with L a characteristic length scale, for which in blood flow the diameter D is the conventional measure and $\nu = \frac{\mu}{\rho}$ the kinematic viscosity. In the arterial system, Re ranges from 1 for arterioles up to 4000 in the largest vessel, the aorta.[26] The Reynolds number differentiates between laminar and turbulent flow, which exhibit strongly different characteristics. For pipe flow, viscous effects stabilize flow patterns up to $\mathrm{Re} \approx 2040$,[27] creating a stable velocity field in which fluid typically flows in parallel layers or laminae (Fig. 1.3), hence its classification as laminar flow. With higher Re, the dominance of inertial forces leads to transitional and eventually sustained turbulent flow, a complex chaotic state of fluid flow with stochastic variations of velocity and pressure, formation of eddies,

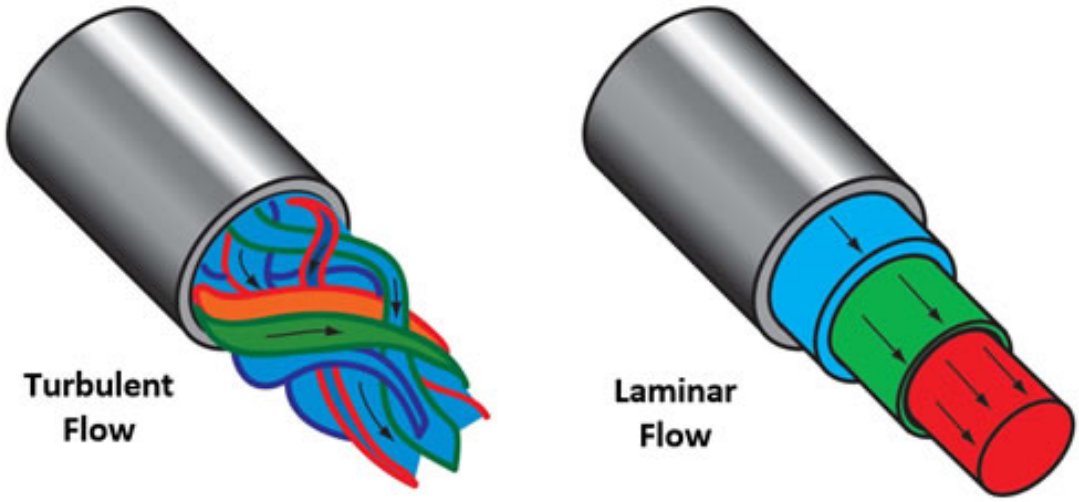

Figure 1.3: A visualization of turbulent and laminar flow. In fully developed laminar pipe flow, fluid flows in parallel layers with small differences in velocity and fluid mixing between these layers is not present.

increased mixing of momentum and particles, and elevated wall shear stress. With abrupt changes in geometry, such as the area increase downstream of a stenosis, localized turbulence can be present in arteries at much lower Reynolds numbers, e.g. at Re = 1000 in the post-stenotic jet breakdown of a 75%-area stenosis.[28]

It is important to discriminate between the fluid mechanical definition of turbulence outlined here and the medical use of the term. In medicine, where the sound waves produced by turbulence (murmurs) have traditionally been used in cardiac auscultation to diagnose valvular disease[29], turbulence has since been commonly used to describe any disturbed flow with circulating features. These flows may still be non-chaotic and therefore laminar, in which case they are much easier to analyze and simulate with computational fluid dynamics.

The Womersley number α is the second non-dimensional parameter relevant to bloodflow. For laminar pulsatile flow, it relates the relative strength of unsteady forces, arising due to the pressure oscillations, to the viscous forces

$$\alpha = \sqrt{\frac{\text{transient inertial effects}}{\text{viscous effects}}} = \sqrt{\frac{\rho\omega v}{\mu v/L^2}} = \frac{D}{2}\sqrt{\frac{\omega}{\nu}} \tag{1.4}$$

with ω the heart rate in angular frequency and L the characteristic length, which is defined as the radius for pipeflow, in contrast to the diameter in the Reynolds number. The viscous effects now include the term $\frac{v}{L}$ to express their time characteristics and ensure dimensionality of α. For $\alpha << 1$, the viscous forces dominates, the velocity profile is parabolic in fully developed flows and the flow rate oscillates in phase with the pressure. For $\alpha >> 10$, unsteady forces dominate causing the flow

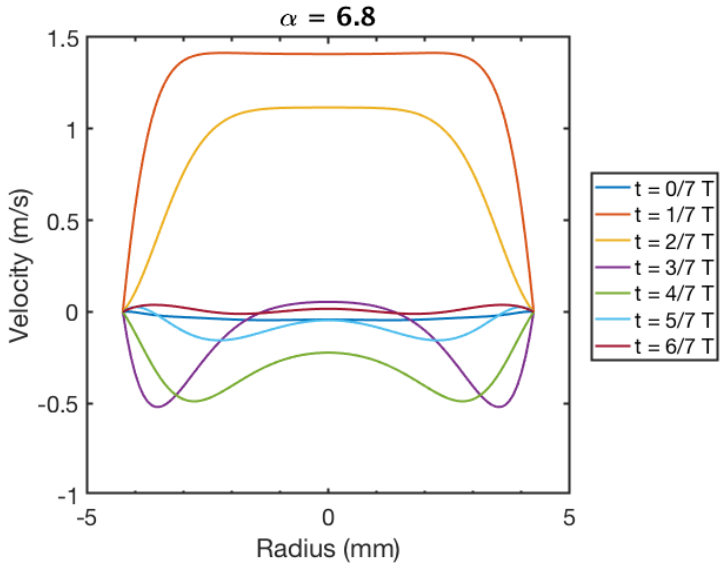

Figure 1.4: Fully developed Womersley profiles in triphasic femoral artery flow. Flow reversal is prominent at the near-wall region, due to the fluid's fierce inertia at the center region during systole.

to have a plug-like profile and the flow rate lags the pressure oscillation by 90°. For arterial flow, diameter is the main determinant of α, with values of 14 in the ascending aorta (D=25mm) and 6 in medium-sized arteries like the femoral artery (D=9mm). Fig. 1.4 presents Womersley flow for a typical triphasic flow profile in the common femoral artery, highlighting the pronounced near-wall flow reversal typical of flow with an intermediate Womersley number.

This section concludes with examples of how inertial and viscous effects affect arterial flow in three idealized geometries that are prone to atherosclerosis: a sudden increase in vessel lumen, a curved artery and a bifurcation.

1.3.1 Blood flow dynamics in geometries prone to atherosclerosis

Lumen expansion When bloodflow experiences an expansion in lumen area, such as in the carotid sinus, downstream of a stenosis or in an aneurysm, flow reversal near the wall typically occurs. This may be explained by Bernouilli's principle, which states that pressure in a decelerating fluid increases. As the fluid (Fig. 1.5) enters an area-expansion region, its velocity decreases with an associated increase in pressure. This sets up an adverse pressure gradient, which causes near-wall fluid with an already low velocity to reverse in direction. In steady flow, this effect leads to a stable region of recirculating flow, a vortex, which can be associated with secondary vortices downstream in an assymmetric area-expansion, e.g. an eccentric stenosis (Fig. 1.5). In pulsatile flow, the vortex cyclically expands and reduces in size, and may be periodically shed with the flow during the acceleration

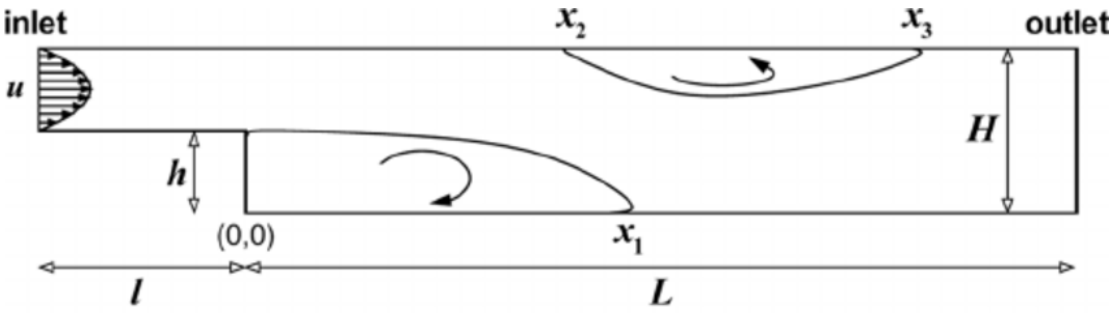

Figure 1.5: When flow encounters an area-expansion, separation of the boundary layer typically occurs, giving rise to one or multiple vortices with recirculating flow. [31]

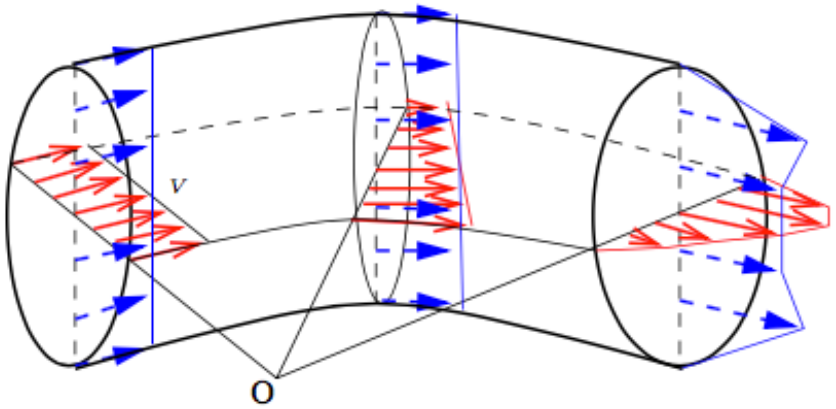

Figure 1.6: Axial velocity profiles in entrance flow of a curved artery. Inertial effects first shift peak flow to the inner wall, after which viscous effects create an M-like peak flow pattern located at the outer wall. Reproduced from lecture notes by F.N. van de Vosse and M.E.H. van Dongen.

phase, generating a series of downstream vortices. [30]

Curved artery Curvature is another omnipresent characteristic of arteries and a source of secondary flows and possibly flow separation. Secondary flow is used to describe velocities in the axial plane that are perpendicular to the primary flow direction. In curved arteries, both viscous and inertial effects generate secondary flows in opposing directions. The inertial effect is best explained by considering a plug-like flow profile entering a curved artery. A centripetal force must be present to bend blood's momentum through the curve, which is delivered by a transaxial pressure gradient with high pressure at the outer wall and low pressure at the inner wall. This gradient generates a secondary flow where fluid moves radially inward in the axial plane, causing peak velocity to shift to the inner curvature.

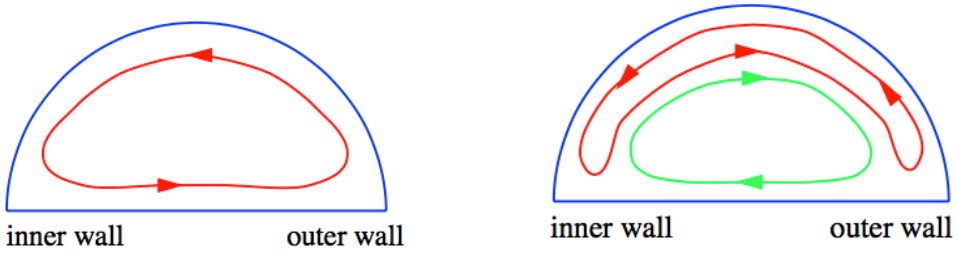

(a) Steady flow **(b)** Oscillatory flow

Figure 1.7: Streamlines of secondary flows in a curved artery.

The viscous forces in a curved artery generate secondary flows in reversed direction through its effects in the boundary layer. The viscous forces retard flow in the boundary layer while the pressure gradient that functions as centripetal force is essentially unaltered. The slower moving fluid at the walls is therefore pushed inward at the upper and lower walls, which is balanced by fluid moving from the inner to the outer wall through the center plane of curvature. Two counter-rotating vortices in the axial plane are therefore formed, of which one is shown in Fig. 1.7a. These secondary flows shift peak flow to the outer wall, which one may intuitively consider as the fluid with highest velocity taking the outside bend. The net effect of the primary and secondary flow by this viscous effect is a helical particle motion.

The viscous effect is dominant in steady developed flow (Fig. 1.7a), such as curves in vessels with relatively continuous flow like the renal, visceral and carotid arteries. The inertial effect is dominant for entry curvature flow with a plug-like inlet profile, where the boundary layer hasn't developed yet, as in the first half of the aortic arch during the systolic upstroke. In oscillatory flows, both effects are usually relevant[32] and may combine to form the secondary flow shown in Fig. 1.7b, with viscous effects generating near-wall vortices in the wall region, and inertial effects generating counter-rotating vortices in the inviscid center region.

Bifurcation In bifurcating arteries, the nature of flow becomes more complicated with dependencies on the flow rate, the bifurcation angle and the diameters of the mother and daughter vessels[33]. Flow is split in a region called the flow divider, where pressure gradients split and diverge momentum into the two daughter branches. The bifurcation can be seen as the junction of two curved vessels, where secondary flow in the form of one or multiple counter-rotating vortices are created by viscous and inertial forces, forcing the fluid to move in complex helical paths in the proximal daughter branches. In a T-junction, which shares similar features with the femoral bifurcation, flow separation and recirculation commonly occur at two locations at the outer sides of the bifurcation, e.g. S1 and S2 in Fig. 1.8b. Region S1 is caused by the sharp angle that the flow has to take, region S2 on the other hand is caused by the pressure gradient that is set up to push part of the flow into ves-

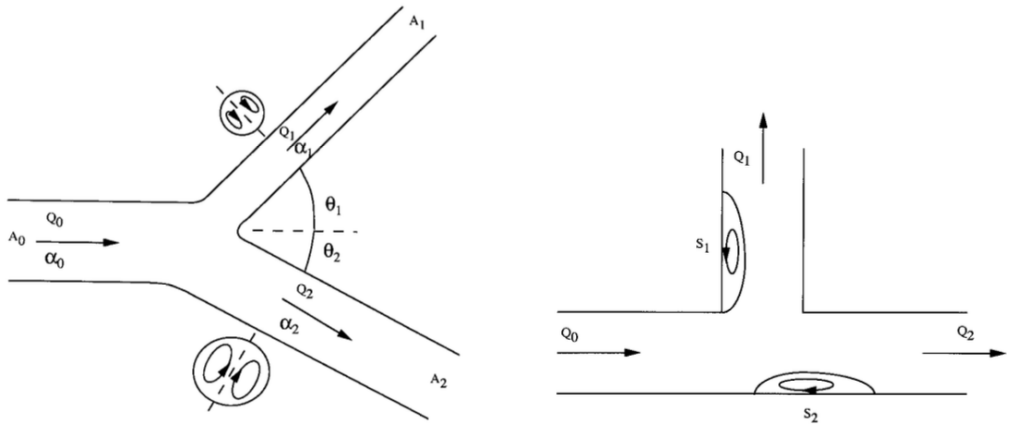

(a) Secondary flow due to branching vessel curvature **(b)** Flow separation in a T-junction

Figure 1.8: An arterial bifurcation creates secondary flows akin to a curved vessel and distinct regions of flow separation.[33]

sel 1. This creates a high pressure at the wall near region S2, resulting in an adverse pressure gradient that causes flow reversal at the wall.

1.4 Computational fluid dynamics

CFD is a specialist field of mathematics and a branch of fluid mechanics, the study of motion of liquids and gases. It is extensively used in shape optimization and safety tests for aircraft and vehicle design and its adoption in biomechanics is increasing.[34] CFD is a valuable tool in addition to fluid mechanical experiments or measurements by providing additional data and allowing for a rapid simulation of the effect of changes in the geometry or boundary conditions. This section will briefly discuss the current position of CFD in medicine and provide a very basic introduction to the two most common techniques, the finite volume and finite element methods.

In the context of blood flow, CFD can provide data on the pressure field which can typically only be measured through an invasive catheter. As an example of CFD's ability to investigate clinically relevant model modifications, CFD can be used to assess the effects of an increase in blood flow, or the effects of a changes in anatomy due to a surgical or endovascular intervention. However, the physics of fluid flow is complex, even more so in the biophysical context of blood flow, where vessel wall movement and blood's non-Newtonian behavior may significantly impact the physical behavior of fluid flow. When devising a CFD approach for a particular area of clinical interest, many simplifications and, at present, user-dependent choices have to be made. Careful and rigorous validation of the CFD results is therefore necessary to generate confidence in the accuracy and reliability of the CFD model. Currently, CFD for cardiovascular medicine is mainly used in bioengineering research

and medical device design, with very limited use in clinical decision making. For the latter, the only known use is the service of the HeartFlow company (Redwood City, CA, USA), whose CFD model accurately predicts the pressure drop over a coronary stenosis from a CT-scan, data that was previously only available from invasive catheter measurements.[35]

1.4.1 The fundamental approach

The main idea of CFD for blood flow is to solve the Navier-Stokes equations (Eq. 1.2) in a well-defined domain. For blood flow in an artery, these involve the geometry characterization, typically part of the full length of one or more arteries, and defining blood's behavior at the boundary of the domain, e.g. the vessel wall and the inflow and outflow parts. For a CFD model with appropriate simplifications and discretization techniques, these choices are the main determinants of the final solution, and further attention to them will be given in chapter 2. The two most fundamental discretization techniques used in 3D blood flow modeling are the finite volume and finite element methods. The finite volume technique has a slightly longer history and is used in most current commercial CFD packages. It has the advantage of having a more intuitive description. The finite element method is a more general approach and has originated from simulating the mechanics of solids, such as vessel wall movement. Its application for fluid mechanics is more common in academia at present.

Both these methods do not discretize the differential or strong form of the Navier-Stokes equations, but its integral form. The common finite volume formulation results from integrating equation 1.2 over a control volume and applying Gauss' theorem for the convective and stress terms

$$\begin{gathered}\rho\frac{\partial}{\partial t}\int_V \boldsymbol{v}\mathrm{d}V + \rho\oint_A \boldsymbol{v}(\boldsymbol{v}\cdot\boldsymbol{n})\mathrm{d}A = \oint_A (\mu\nabla\cdot\boldsymbol{v} - p)\cdot\boldsymbol{n}\mathrm{d}A + \int_V \boldsymbol{g}\mathrm{d}V \\ \oint_A \boldsymbol{v}\cdot\boldsymbol{n}\mathrm{d}A = 0\end{gathered} \tag{1.5}$$

with V the volume of the domain, A the surface enclosing the domain and n the surface normal vector. After splitting the full domain in a large set of finite volumes, these equations are set up for every subvolume to discretize the Navier-Stokes equations for the full domain. An example for the discretization of the conservation of mass for a cubic volume is shown in Fig. 1.9. Discretization of the momentum conservation follows an analogous route, now also requiring the computation of the viscous and pressure stress terms at the faces, requiring more elaborate interpolation techniques. In general, many types of control volume shapes may be used, but by far the most common for blood flow are tetrahedral elements, as these are most easily implemented in algorithms to mesh complex arterial geometries.

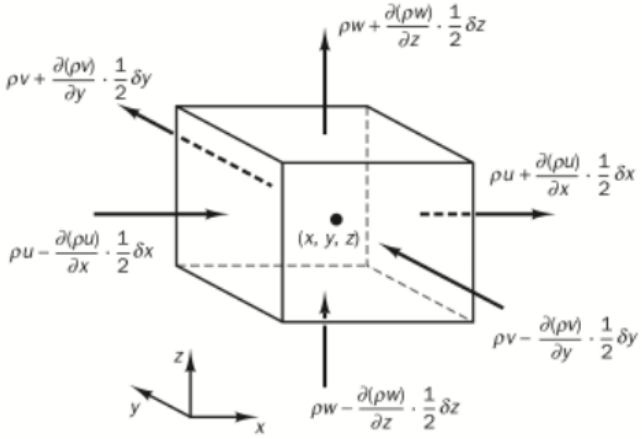

Figure 1.9: A visualization of the finite volume discretization for the mass conservation. The full geometry may be subdivided into tiny volumes, in this example cubes. For an incompressible fluid like blood, the sum of the fluxes through the six sides of the square have to equal zero up to an accepted tolerance for a converged solution.

The finite element method solves a weak form of the Navier-Stokes equations, obtained after multiplying equation (1.2) by a weighting function $w(x)$ and integrating over a volume.

$$\begin{aligned} \int_V \left(\rho \frac{\partial \boldsymbol{v}}{\partial t} + \rho \boldsymbol{v} \cdot \nabla \boldsymbol{v} - \mu \triangle \boldsymbol{v} - \nabla p - \boldsymbol{g} \right) w(\boldsymbol{x}) \mathrm{d}V = 0 \\ \int_V \left(\nabla \cdot \boldsymbol{v} \right) w(\boldsymbol{x}) \mathrm{d}V = 0 \end{aligned} \tag{1.6}$$

Following the method's terminology, these volumes are called elements, but they serve the same function as volumes in the finite volume method. For the nodes of an element, velocity and pressure are approximated by linear combinations of basis functions, commonly taken as polynomial functions locally defined within one element. For one node, a global shape function is constructed by assembling the basis functions of the elements that the node is part of. The solution is built by multiplying the global shape functions with the coefficients that are computed by the FEM solver. For CFD codes of complex geometries of blood flow, piecewise first-order or linear basis functions are almost exclusively used at present. Figure 1.10 illustrates a basic example in one dimension of piecewise linear shape functions.

In the computation of the coefficients, the choice of the weighting function w is fundamental for the resulting discretization scheme. In fact, for a particular family of weighting methods, the subdomain collocation, with a uniform weight function within the subdomain and zero outside, the finite element construction is equal to the basic finite volume method.[36,37] The weighting function typically used when referred to the finite element method for fluids is the Petrov-Galerkin weighting.

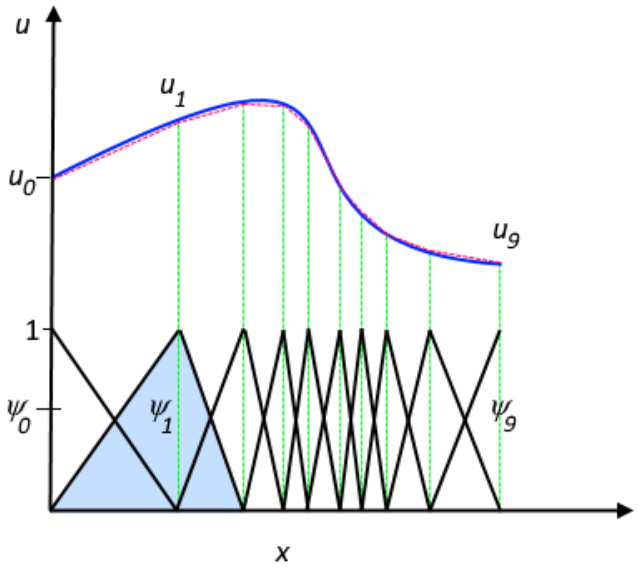

Figure 1.10: In the finite element method, the solution approximation is built by multiplying the global shape function of the nodes ($\psi_1 - \psi_9$) by its computed coefficients ($u_1 - u_9$) and summing the contributions of all nodes.

In this weighting scheme, which takes the convective nature of the flow physics into account, the weight function is dependent on the cell Péclet number, which depends on the ratio of convective and diffusive forces. For the finite volume method, somewhat analogous upwinding schemes are used to produce discretization schemes that reproduce physical flow behavior.

Both techniques involve a substantial body of technicalities regarding mesh topology, pressure-velocity coupling and time stepping, which are fully detailed by Versteeg & Malalaserkera [38] for the finite volume method and by Zienkiewicz et al. [37] for the finite element method. On top of that, the matrix-system of equations set up by both methods is of such substantial size that, for pulsatile blood flow problems, specialized parallellized computing resources and techniques, in combination with efficient numerical solver schemes, form a prerequisite for achieving simulation times within the order of hours or days. These will not be touched upon in this work.

Essentially, all models are wrong, but some are useful.

George E.P. Box

2

Design of a clinical CFD pipeline

This methodological chapter deals with the steps needed to construct and run a CFD simulation of a patient-specific anatomy and boundary conditions. For different arterial sites and the clinical problem at hand, the appropriate modeling choices may naturally differ, as well as the available anatomical and functional imaging modalities. The overall method presented here is geared towards the femoral artery, but the techniques used translate easily to other arterial domains. Clinical applications in mind during the development of the method were the non-invasive prediction of wall shear stress and pressure drops in the femoral bifurcation and its major branches.

The methodology is presented in four distinct phases: (1) segmentation of patient anatomy, (2) determination of patient-specific boundary conditions, (3) volume meshing strategies, (4) constitutive models and (5) CFD solver considerations.

2.1 Segmentation of a patient's anatomy

For CFD on 3D patient-specific geometries, computed tomographic angiography (CTA) and magnetic resonance angiography (MRA) are commonly used as image acquisition tool.[34] For MRA, some sequences (contrast enhanced) are more suitable than others (time of flight and phase contrast) for subsequent image segmentation, as most segmentation tools assume the intensity to be directly related to blood content (and not velocity).[39] A relatively novel imaging method that could be of interest in endovascular settings is the rotational angiogram. This technique extends on a traditional angiogram by having the source and flat-panel sink make a semicircle rotation (180-200 degrees) while intra-arterial contrast is continuously injected upstream. A subsequent volume reconstruc-

tion can be made using similar techniques as in CT-scanning, which has been used as input for CFD simulations. [40]

One of the current clinical research focuses was to perform CFD simulations of a stented femoral artery, as treated in chapter 5. However, for PAD patients with endovascular procedures of the femoral artery, post-operative CTA's or MRA's are generally unavailable, as these are not part of routine clinical follow-up. To acquire a patient's post-operative geometry, rotational angiography may be an alternative with only a minor contrast, ionization and clinical workflow burden compared to CTA. For this particular cohort, performing a rotational angiogram in a hybrid operating room immediately after stent placement was a hypothesized alternative to CTA. Together with the radiology team, several rotational angiograms were tried peri-operatively with the current Philips Xper FD20 system with 3D-RA software. However, practical issues with the scanner's motion bodyguards in an active operating room setting limited the success rate to 1 out of 3 procedures, in which the catheter was not optimally positioned to deliver contrast medium to the profunda femoral artery. With further practice this may be improved, but experience from other centers shows that mainly new Philips software or equipment (the VesselNavigator software or an Azurion workstation) is likely to boost the feasibility of rotational angiography.

Segmentation Reconstruction of arterial anatomy from 3D imaging data is a fast developing field, featuring many different underlying mathematical approaches. [41] Important aspects for clinical CFD simulations are that user input in the segmentation process is minimal and that the segmented geometry is of sufficient smoothness, which can be challenging for noisy imaging data. Table 2.1 summarizes three approaches from different software suites that I experimented with. I have chosen to work mainly with the approach incorporated in VMTKlab, primarily due to the minimal amount of user input throughout the various steps.

Table 2.1: Segmentation software

Name	Method	Considerations
Mimics	Region-growing	Fast and robust. Sensitive to noise and contrast inhomogeneities.
SimVascular	Centerline and cross-section contours (2D); wave propagation (3D)	High level of user control. Wide toolset and open-source. 2D-segmentation time-consuming.
VMTKlab	Implicit active contours	Elegant approach with minimal user input. Some software instabilities.

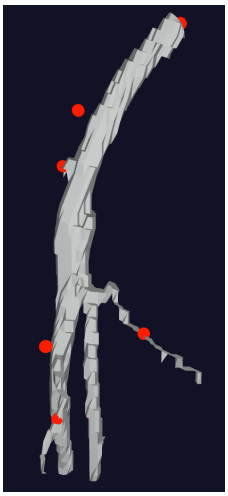

(a) Surface initialization by wave propagation

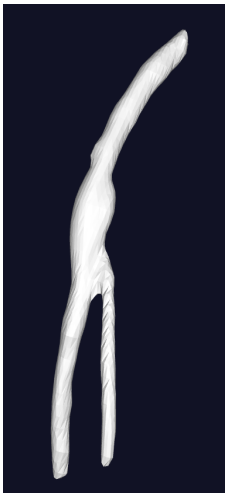

(b) Surface regularization by advection to the vessel wall and smoothing constraints

Figure 2.1: Segmenting a femoral bifurcation in VMTKlab. The red dots are user-defined endpoints. Small side-branches are intentionally lost during the regularization due to internal smoothing forces.

The VMTK software is anchored on the level-set technique of implicit active surfaces.[39] First, an initial level set function ϕ_0 with zero-level isosurface $S(t)$ is formed based on wave propagation from user-defined seed points, with a wave speed determined by local image intensity. Second, deformation of the isosurface $S(t)$ due to evolution of the level set function by image and shape-based forces is modeled by the PDE

$$\frac{\partial \phi}{\partial t} = -w_1 \frac{1}{1+|\nabla I|}|\nabla \phi| + 2w_2 \nabla \cdot \left(\frac{\nabla \phi}{|\nabla \phi|} \right) |\nabla \phi| - w_3 \nabla |\nabla I| \cdot \nabla \phi \tag{2.1}$$

with ∇I the image intensity gradient and w_i user-set weighting terms from 0 to 1. The terms associated with the weights model, respectively, shape inflation inversely proportional with the image gradient (w_1), smoothing of the model shape based on its mean curvature (w_2), and advection of the shape towards the ridges of the image gradient magnitude (w_3), the vessel wall. For very clean image data, evolving the surface by just the advection force may prove sufficient. For most image data, however, applying the smoothing force is necessary. The smoothing based on mean curvature is likely to shrink the surface to some extent, which should be adjusted for by compensating with the inflation term.[39] Conversely, the surface shrinking effect, especially pronounced for tiny vessels, can be used to cut small side-branches during segmentation, as has been done in figure 2.1.

2.2 Patient-specific boundary conditions

Boundary conditions dictate the velocity, flow rate, pressure or a relation between flow and pressure at the inlet and outlet(s) of the model. Various combinations of these are possible in formulating a well-posed problem in combination with the Navier-Stokes equations on the flow domain. Accurate boundary conditions are essential for realistic CFD predictions, but deriving representative boundary conditions for an individual patient is challenging.

Inlet At the inlet, a velocity distribution (Dirichlet boundary) or pressure waveform (Neumann boundary) can be prescribed. Typically, only clinical information on flow rate can be reasonably acquired, as pressure cannot be measured sufficiently accurate by non-invasive means and velocity distributions in an axial plane is at present only available through PC-MRI, not available in most clinics. The mapping of a known flowrate to a velocity distribution requires additional assumptions. Commonly, flow is assumed to be fully developed at the inlet, so that the velocity field can be derived from Womersley's analytical solution, also for slightly non-circular cross-sections by trivial linear rescaling.[42] Assuming a fully developed flow instead of a patient's measured velocity profile was shown to effect wall shear stress and oscillatory shear index by 5-10% in a carotid bifurcation, where the Womersley number is 4 on average.[43]

Outlets For the outlets, numerous types of boundary conditions are possible. Traditional boundary conditions imposing time-dependent velocity or pressure at the outlets are impractical, as these are hard to acquire clinically and tough to apply in a manner consistent with pressure propagation due to wall motion.[44] Constant-pressure boundaries (traction-free boundaries) are quite often seen in literature, even in the case of multiple outlets as for the femoral bifurcation,[45] but these assume that the distal vascular beds have equal impedance,[46] which is rarely the case. Boundary conditions more suited to reflect the distal vasculature enforce a well-matched impedance, i.e. pressure-flow relationship, at the boundary. These range from a simple resistive relation ($\frac{P}{Q}$ = constant), or the Windkessel RCR-model, to more complex impedance functions. Only the latter two can realistically model wave propagation, as the resistive condition forces flow and pressure to be in phase.[44] For the carotid bifurcation, a resistance boundary condition compared to a well-tuned RCR-model produces wall shear stress and oscillatory shear values that deviate by about 10-30%.[47]

The femoral bifurcation For patients with PAD, duplex ultrasound data is commonly available, whereas PC-MRI is not. After a femoral-popliteal duplex examination, time-varying peak velocity in the distal common femoral, proximal profunda, and proximal, mid and distal superficial femoral artery is typically stored. After transforming these into flow rates, discussed in the next

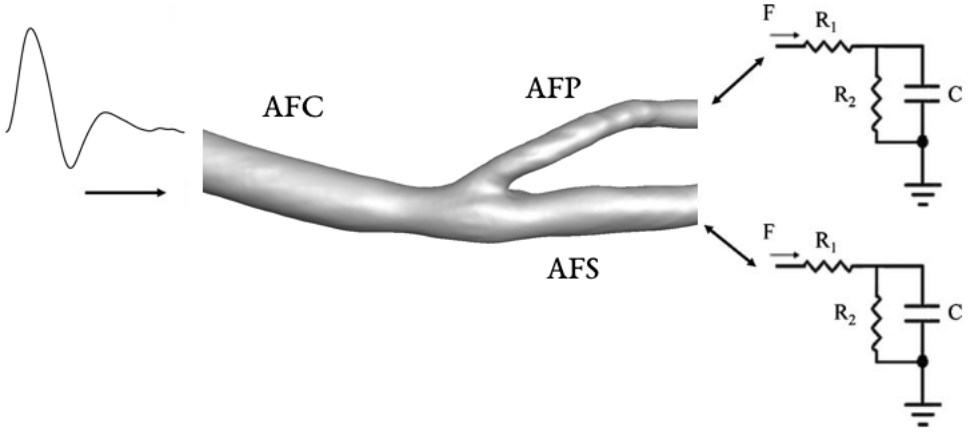

Figure 2.2: The conditions applied to the boundaries of the femoral bifurcation. A time-varying flowrate is enforced on the inlet and a pressure-flow relationship is enforced on the outlet, through RCR-models of the distal vasculature.

section, two observations underline the need of individual patient-tuned impedance boundary conditions. First, after measuring flowrates in a set of young individuals (7 people aged 20-30 years, not reported in this thesis), it became apparent that substantial natural variation in both the mean flow distribution towards the AFS and AFP, as well as variation in the level of flow pulsatility existed. Second, PAD patients who need femoral artery treatment typically show co-existing disease in the popliteal or one or more tibial arteries, in response to which collaterals stemming from the AFP may develop.[48] These can significantly impact the flow rate distribution towards the AFP and AFS.

To be able to model these variations, RCR-models are chosen as outlet boundaries. Resistive boundaries cannot model differences in pulsatility between the AFP and AFC, and do not yield realistic pressure profiles, a prerequisite for additional simulation of vessel wall motion. For the inlet, the flowrate derived from duplex measurements is imposed as time-varying velocity distribution based on the Womersley profile. Fig. 2.2 displays the modeling approach of the boundary conditions. The RCR-values have to be tuned such that, when the inflow is set by the known AFC profile, the flow rate profiles in the AFS and AFP resemble the profiles measured by duplex. The following approach is taken: (1) compute the combined total resistance based on mean flow and pressure values ($R_t = \frac{\bar{P}}{\bar{F}}$), (2) determine the proximal AFP and AFS resistance R_1 as measured by Westerhof and colleagues[49], then the R_2 values can also be calculated, (3) calculate a total compliance value that produces a physiologic pulse pressure, (4) tune the individual contribution of the AFP and AFS compliance to match the measured AFP and AFS flow profiles. For the last step, a parallel RCR-model in SimuLink was built. The proximal R_1 values may additionally be tuned in case of proximal stenoses in the AFP or AFS or when a substantial phase shift is present between the AFP and AFS flowrates that cannot be modeled by differential compliance alone.

2.2.1 Deriving flow rate from duplex ultrasound

Two approaches were tested in volunteers to compute a time-varying flow rate from duplex measurements. The first approach employs a wide ultrasound beam for uniform insonofication of a full axial arterial cross-section.[50] The average of all measured velocities then equals the axially-averaged velocity, which is calculated by the Doppler device and multiplied by the ultrasound determined cross-sectional area. The second approach instead directs a narrow ultrasound beam into the vessel and collects a small volume sample from the central lumen, in order to record the peak velocity in the centerline.[51] By assuming a fully developed flow profile, a corresponding flow rate is computed through Womersley's theory[52,53]

$$\begin{aligned} Q(t) &= \sum_{k=0}^{\infty} \hat{Q}_k \cdot \exp(\mathrm{i}k\omega t) \\ \hat{Q}_k &= \pi R^2 \hat{u}_k \frac{J_0(\mathrm{i}^{3/2}\alpha_k) - \frac{2}{\mathrm{i}^{3/2}\alpha_k} J_1(\mathrm{i}^{3/2}\alpha_k)}{\mathrm{i}^{3/2}\alpha_k - 1} \end{aligned} \tag{2.2}$$

with Q and $\hat{Q}$ the flow rate and its Fourier coefficients, $\hat{u}$ the Fourier-coefficients of the centerline velocity, R the vessel radius, J_x the Bessel-function of the first kind of order x, and α_k the frequency-dependent Womersley parameter, equal to Eq. 1.4 multiplied by $\sqrt{\omega}$.

The first method is more optimal in that it makes no assumptions on the flow profile. The second method is more practical because it can be applied on routine duplex measurements of the femoral artery, also retrospectively. As the ultrasound manufacturer could not give access to the raw data, a Matlab GUI (Fig. 2.3) was built to extract velocity tracings from duplex image data. In an in-vitro setup, the first method provides a level-of-accuracy of about 5-10% for flow rates of 500 mL/min, but in the anatomically more challenging femoral arteries, both inter- and intra-observer variabilities of 15-20% are reported[54], with an exceptional 40% variability for the PFA. The variability originated mostly from the mean velocity component and less so from the diameter estimation. In our sample measurements (7 with method 2, 1 with method 1), similar high levels of variability were seen for both methods, and on average only 80% of total volume flow in the AFC was recorded in the AFS and AFP measurements.

2.3 Volume meshing

After segmenting a patient's geometry, the vessel lumen must be discretized into many tiny volumes to create a volumetric mesh. The edge size of one volume typically ranges from 0.3-1.0mm, generating meshes of a few 100.000 to over 10 million cells for a femoral bifurcation (mesh size grows

Figure 2.3: A Matlab GUI was designed to retrieve time-varying velocity data from clinical duplex measurements, for which raw data could not be extracted. The GUI features color filtering and pixel tresholding as image pre-processing and traces the curve by taking the pixels farthest from the zero-velocity line. Smoothing of the result is implemented by reconstruction in the frequency domain with a user-controlled number of fundamental frequencies.

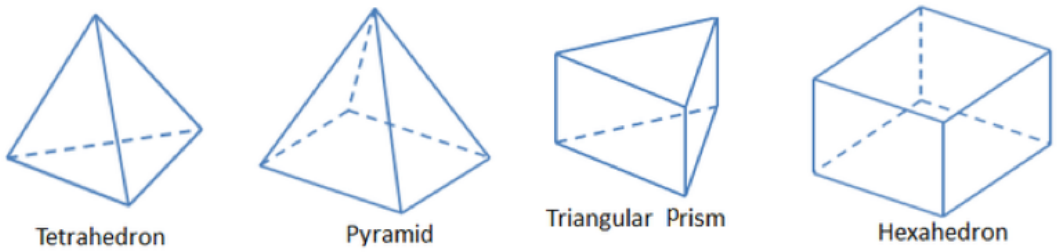

Figure 2.4: Common building blocks for a CFD mesh. A pyramid can be made by joining two tetrahedrals, a prism by three tetrahedrals and so on.

with the inverse cube of edge size). Meshing is an important step in simulations, as it can greatly impact the accuracy of the solution. After meshing, the CFD solver discretizes the conservation laws through the procedure described in section 1.4.1, which produces discretization errors that relate to the mesh edge size. Commonly the error increases linearly or with the square of the mesh size (1st or 2nd-order scheme). It is therefore imperative to assess if a mesh has reached convergence, meaning that the discretization error has shrunk to acceptable limits. This is done by inspecting the effect of subsequent mesh refinements on the quantity of interest in the final solution; if the quantity no longer changes appreciably with further refinement, the mesh is converged. As this is very time consuming to compute for pulsatile flow, usually the case of steady flow is taken as substitute.

Table 2.2: Meshing software

Name	Meshing method	Considerations
Ansys ICEM	Unstructured	Supports a hybrid mesh with hexahedral core.[55] Many steps involved.
SimVascular	Unstructured	Fast and easy, no hybrid meshing.
pyFormex	Structured	Specialized module for structural meshing of arterial bifurcations[40]

For cardiovascular models, two main meshing approaches exist: structured meshing with hexahedrals, or unstructured meshing with tetrahedrals. A structured mesh has tremendous advantages in computation time and accuracy, but is rather difficult to generate for complex geometries like an artery. Conversely, decent and fast meshing algorithms exist for tetrahedral meshing, at the cost of longer computation times for similar levels of accuracy. For this work I have opted for the latter.

As wall shear stress is a derivative measure of near-wall velocity, its accuracy benefits from a high spatial resolution in the normal direction of the wall. For that purpose, the boundary region is

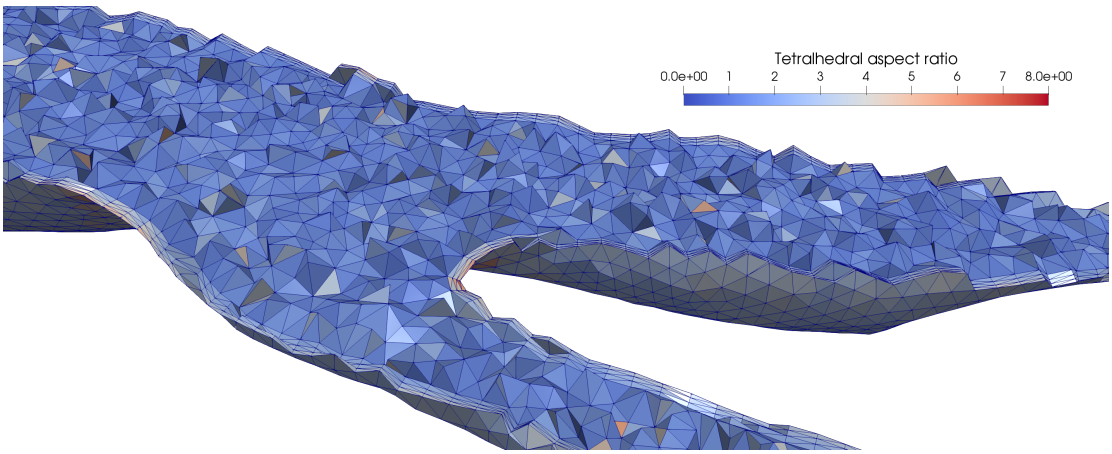

Figure 2.5: Example of a coarse tetrahedral mesh, created with SimVascular, of the segmentation of the femoral bifurcation shown in Fig. 2.1. The area near the wall has been meshed with three prismatic layers to improve wall shear stress accuracy.

meshed with a stacked layer of three prisms, see Fig. 2.5.

2.4 Constitutive models

To complete the physical description of the system, material properties for blood, and possibly the vessel wall, have to be specified. These include a constitutive model, which describe the stress-strain relationship, and material constants. In the Navier-Stokes equations given in Eq. 1.2, it was implicitly assumed that blood has a constant viscosity. Blood is in fact a non-Newtonian fluid with shear-thinning behavior relevant to flow in large arteries, owing to the influence of red blood cells. This can be modeled by specifying viscosity as a non-linear function of shear rate through increasingly complex relations like a power law, Casson, and Carreau-Yasuda models.[56] The effects of different viscosity models have been documented in several studies on patient-specific flow in the carotid bifurcation and were shown to change wall shear stress magnitude by 5-10% without changing its qualitative distribution over the vessel wall.[57,58,59] As the non-Newtonian effect is of smaller magnitude than the accuracy of geometric segmentation, outflow conditions and wall motion, blood is approximated as Newtonian in this work.

The material constants that need estimation for a Newtonian model are blood density and viscosity. As dimensional analysis of the Navier-Stokes equations shows, it is the ratio of the two that determines a fluid's behavior (kinematic viscosity $\nu = \frac{\mu}{\rho}$, see Eq. 1.3). As clinical measurements of hematocrit are routinely available, this is the most practical input to estimate these constants on a patient level. Blood density is rather constant and depends on hematocrit to a small degree, ranging from 1045-1060 kg.m^{-3} for hematocrit ranging from 0.35-0.55.[60] Viscosity of blood varies consid-

erably more with hematocrit content, ranging from 3-6 mPa.s for the same hematocrit range. [61] For current purposes, it can be approximated by Batchelor's formula [56]

$$\mu_{\text{blood}} = \mu_{\text{plasma}}(1 + 2.5\epsilon + 6.2\epsilon^2) \tag{2.3}$$

with ϵ the volumetric cell fraction of blood, considered equal to hematocrit, and the viscosity of plasma equal to 1.2 mPa.s. [56] Blood viscosity will be estimated by this formula, whereas blood density will be assumed constant at 1059 kg.m^{-3}.

2.5 CFD solvers

After meshing the domain and defining the conditions at the boundary of the domain and the material properties, the solver discretizes and solves the Navier-Stokes equations on the mesh. For the present goal of computing flow in the femoral artery, the applicability of two different solvers has been assessed, both on the range of physical phenomena they can model and on practical grounds. CFD solvers are typically either commercial software, an open-source initiative developed by multiple research groups or in-house schemes used by an academic group. A brief review of relevant solver terminology is first given here, after which the commercial solver Ansys Fluent and the open-source SimVascular solver are compared. A number of other solvers that have been aplied to blood flow has been reviewed by Randles et al. [62]

For the computation of blood flow in a 3D-domain, the resulting system of equations generally cannot be solved by a direct method due to unreasonably high memory and computational time requirements. [63] Solvers therefore use an iterative approach, in which several iterations of a numerical scheme produce an increasingly accurate approximation of the solution at one time-step. For each timestep, solvers can be set to perform a set amount of iterations, keep performing iterations until the accuracy reached a defined treshold, or a combination of both. Certain physical phenomena like turbulence or backflow at an outlet may limit the solver's ability to converge towards an accurate solution for parts of the cardiac cycle. The behavior of the residual (i.e. the solution's deviation from the conservation of momentum and mass) must therefore be assessed on convergence over all steps of the cardiac cycle during or after the computation.

Fluent is a widely used commercial solver based on the finite volume method. Its approach is generic, making it applicable to many flow regimes. Owing to its universality, application-specific boundary conditions like RCR-outlets are not a default option, but these can be added through user-defined functions. Typical of a commercial solver, the software's features are thoroughly documented, but the in-depth implementation of the solver's algorithms is unknown and cannot be changed, as this information is proprietary. SimVascular is an open-source software that has at its basis the PHASTA finite element code for incompressible flows, [64] a generic-purpose code that sup-

Table 2.3: CFD solvers

Name	Discretization	Considerations
Ansys Fluent	Finite volume	Implementation of turbulence models, full FSI through coupling with structural solvers.
SimVascular	Finite element	Full cardiovascular modeling pipeline, dedicated cardiovascular boundary conditions, backflow stabilization, cost-effective wall modeling, open-source.

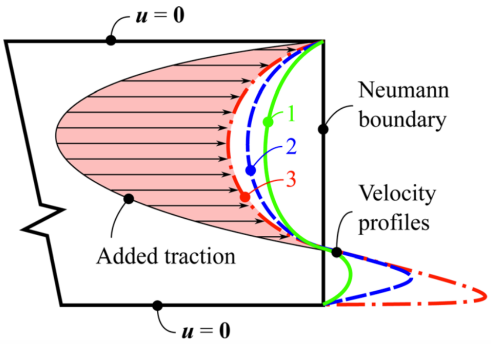

Figure 2.6: Partial flow reversal at an outlet, as can occur if a stenosis is present upstream. During solver iterations, the solution can evolve from the first to the third velocity profile, as all three profiles satisfy mass conservation. This may predispose to divergence of the computational solution, which can be prevented by adding an artificial traction proportional to velocities directed inwards into the domain. Reproduced from Marsden & Esmaily-Moghadam [66]

ports basis functions of linear and higher orders and which has been applied to laminar, turbulent and multi-phase flows. SimVascular has adopted the code for linear basis functions and extended and optimized its use for cardiovascular flows through the addition of backflow stabilization,[65] multiscale coupling with physiologic boundary models,[66] a coupled momentum method[67] and improved numerical algorithms.[63]

Backflow stabilization The consideration of backflow is particularly relevant, as the femoral artery is characterized by flow reversal at the start of diastole, which involves phases of partial and full flow reversal at the outlets. Another situation where partial flow reversal occurs is when upstream structures like stenoses create vortices that flow through the outlet. As outlined in Fig. 2.6, partial flow reversal at a Neumann (pressure) boundary creates ambiguity in the velocity profile solution. Information on the velocity profile outside of the boundary is by definition unavailable, so the inward velocities are not constrained in their value as there is no unique velocity profile that satisfies the conservation of mass. Especially velocities in the direction tangent to the boundary are

unrestricted for backflow, as these do not impact the mass flow through the outlet. This situation typically impedes convergence of a solver and some form of stabilization is needed. Most commercial solvers including Fluent restrict velocity at the outlet to have non-zero value only in the direction normal to the boundary, which works sufficiently for cases in which no strong secondary flow occurs near the outlet. However, if the outlet is in a region of vessel curvature, or not normal to the primary flow direction, this method cannot represent the secondary flows and may lose stability.[65] A common solution then is to extend the outlet with a straight tube in which flow can return to a developed profile. A more cost-effective way that has been shown to work for a variety of challenging conditions is adding artificial traction, which can be interpreted as pushing backflow at the outlet slightly in the direction of the outward normal. This is the stabilization approach used by SimVascular.

Transitional flow Second, the onset of transitional flow, like a post-stenotic jet breakdown, puts upper-bounds on the spatial and time resolution for which the flow's turbulent behavior can be appropriately captured. The spatial mesh must have a resolution that resolves the Kolmogorov-scale, the scale at which the chaotic velocity fluctuations in turbulent flow are finally balanced and dissipated by viscous forces. If this scale is resolved, the simulations are termed direct numerical simulations (DNS) of turbulence. For a 3D-mesh, the number of nodes required roughly equals $Re^{9/4}$ for fully turbulent flow,[38] which, combined with the additional constraints on the timestep, currently requires the use of the world's best computing clusters for small Reynolds numbers of 2300-4000. Still, for not very critical stenoses (say $<$85% area-reduction) that produce transitional flow in these Reynold orders, a direct numerical approach with a regionally refined mesh in SimVascular compared favorably to an in-vitro counterpart.[68] The turbulent flow irregularities were found to decrease with increasing mesh resolution, making mesh convergence hard to assess.

Alternatively, the turbulent behavior can be approximated by a turbulence model. SimVascular currently does not include turbulence models, whereas several common models can be applied in Fluent. Normal spatial and timescales can then be used, and the increased turbulent energy loss is modeled by adding a flow-dependent turbulent viscosity. Turbulent characteristics are very flow and thus problem-dependent, however, making it hard to choose a turbulent model and its parameters when faced with a patient's unique anatomy and boundary conditions. For Reynolds numbers up to 500, classical Wilcox turbulence models seem to perform adequately for predicting pressure drops and velocity profiles.[69] For the case of post-stenotic jet breakdown downstream of a 75%-area stenosis, several commonly applied turbulence models fell short in predicting the site and nature of jet breakdown when compared to a DNS benchmark, however.[70] More complex large-eddy simulations[71,72] were better able to capture this flow regimen. All in all, reliably capturing the wall-shear stress patterns of strong post-stenotic turbulence in patient-specific cases seems out of reach for CFD

at present, but realistic pressure drops may be attainable.

Wall motion For the simulations in this thesis, the wall is simply modeled as rigid. Yet for future extensions of the simulation method, it is relevant to address the solver's capabilities for additional simulation of wall motion. Several approaches are possible for implementing the effect of wall motion on the dynamics of blood flow. These are collectively called fluid-structure interaction models and range from the embedding of part of the structural mechanics into the Navier-Stokes equations up to coupling of a full structural solver with the fluid solver, effectively running two simulations that exchange information with one another. These are called partitioned approaches, as the full problem is distributed over two solvers. The associated computational cost and modeling expertise required are often substantial, but the advantage is that common, well-developed solvers can be used, allowing a wide variety of complex models if needed. Ansys provides coupling algorithms for connecting its Fluent solver to its structural Mechanical solver, which for instance has been used to model fluid-structure interaction that differentiates between the mechanical properties of the arterial and venous side of a shunt.[73] Wall motion did not change the qualitative distribution of wall shear stress, however, so a structural solver is probably not clinically relevant in this case. The use of an additional structural solver may only be necessary in problems where plaque or wall rupture are relevant.

If the structural mechanics themselves are not important, but only their effect on the mechanics of blood are of interest, relatively simple and cheap schemes in terms of computational resources are able to model the compliant behavior of the vessel wall and the propagation of pressure waves. SimVascular has embedded such an approach, the coupled momentum method (Fig. 2.7).[67] In this method, fluid at the wall nodes is no longer restricted to zero velocity (the no-slip condition), but is allowed to have momentum directed radially outward of the domain. The elastic mechanics of the wall are modeled linearly by adding a traction that provides a counterpressure against the outward movement of fluid flow. By including several further strategies like stabilization by transverse shear modes, this interaction can be incorporated into the weak form of the Navier-Stokes equations and solved by a fluid solver. Such a monolithic technique solves or combines the equations of fluid and structural mechanics at once, usually limiting them to more simplified models of the interaction but requiring less computational time. Modeling wall motion with SimVascular for example doubles the computational time for walls with uniform properties, whereas more complex partitioned approaches may require ten times the simulation time or more.

Practical considerations Other considerations of choosing an appropriate solver include the simulation time and the ease of stepping through and reviewing all stages of a patient-specific CFD simulation. An important determinant of simulation time for cardiovascular models is the

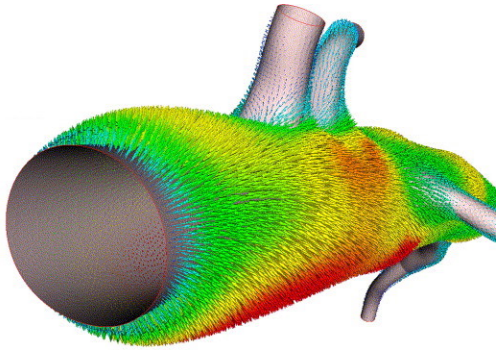

Figure 2.7: An exemplification of the coupled momentum method employed by SimVascular to model wall motion. The wall is modeled as a thin elastic membrane and allowed to move under fluid pressure. The fluid's momentum at the boundary is coupled with the wall's momentum, which effectively models the artery's compliant behavior, storing fluid in systole as shown here. Reproduced from Figueroa et al. [67]

numerical approach of the boundary models. In most cases, the resistance of the microvasculature, modeled by the RCR boundaries, is orders of magnitude higher than the resistance of the arterial anatomy in the 3D-computational domain. Consequently, in a situation with two outlets the mass flow rate distribution and therefore the overall solution is dominated by the boundary conditions, which translates to an ill-conditioned matrix and slow convergence of iterative techniques if not accounted for. SimVascular compensates for the boundaries' dominant effect by pre-conditioning the matrix,[74] likely giving it substantial speed benefits over Fluent with user-defined RCR's. A second and more general requirement for simulation speed is parallellization, the effective distribution of the computational work over multiple cores. In this regard, Fluent appears to perform adequate with 70% strong-scaling at 512 cores[75], yet SimVascular's code has demonstrated 90% strong-scaling up to 30.000 cores.[76] Although a fair comparison of solution times should be based on the same flow problem, which to my knowledge has not been reported in the literature, it is likely that SimVascular is the faster solver for most blood flow problems. Another considerable advantage of SimVascular is the integration of segmentation, meshing and solver capabilities into one streamlined software pipeline, which enhances the overview of a patient-specific project and decreases the learning curve of the full simulation cycle.

Conclusion As addressed in following chapters, clinical problems of interest in this work are the computation of pressure drops over subcritical stenoses and the prediction of wall shear stress in patient geometries. Turbulence models and full structural simulation of wall motion are not relevant to these cases, limiting the advantages of the Fluent solver. SimVascular, in contrast, has many readily available customizations that make it a very fast and stable solver for blood flow and it embeds cost-effective strategies for modeling backflow and wall motion. Further advantages include its

modeling pipeline that follows the steps of segmentation, meshing and modeling outlined within this chapter. SimVascular is therefore employed as solver (and mesher) for the simulations in this work. It has been compiled on the POF cluster in Twente that hosts two nodes of each 64 processing cores, formed by 4 AMD Opteron 16-core central processing units.

If you thought that science was certain - well, that is just an error on your part.

R.P. Feynman

3

Flow through the femoral artery bifurcation

3.1 Introduction

Atherosclerotic disease commonly affects the arterial vessels supplying the lower limbs.[14] The prevalence of peripheral artery disease (PAD) is highly age-dependent and rises over 10% among patients in their 60's and 70's.[2] With half of PAD patients having lesions in the femoro-popliteal trajectory,[77] the femoral artery is the most common site of occlusive disease. Lesions often present downstream of the femoral bifurcation or at the femoral artery's passage through the adductor channel.[24]

A likely contributor to the abundance of atherosclerotic plaques in the distal arteries is the oscillatory nature of flow. Below the level of the renal arteries, substantial reverse flow develops at the end of systole. This leads to regions of low and oscillatory shear stress on the vessel wall, associated with plaque formation.[19] The combination of a high vessel compliance with a high peripheral resistance for the distal vasculature combined with a low compliance and resistance for the renal arteries is an elegant way to model the flow reversal in the region distal to the infrarenal aorta.[22]

To what extent a differential contribution of peripheral arteries to overall peripheral compliance affects flow features in branching sites has to our knowledge not been previously assessed. When considering the simple case of two outflow RCR-boundaries, a common assumption if time-dependent outflow division is unavailable is to set the compliance ratio inversely equal to the peripheral resistance ratio, effectively mimicking an equal RC-time that will cause outflow rates to be in phase and of similar pulsatility. For the femoral bifurcation, 4D-MRI has shown that outflow in

the profunda femoral artery (PFA) and superficial femoral artery (SFA) is typically out of phase in healthy participants, with an onset of peakflow in the PFA earlier in time compared to the SFA.[78] Phase differences between outflow profiles alter the instantaneous flow division during key parts of the cardiac cycle and can impact the onset and growth of recirculation zones seen at bifurcations, especially at T-like junctions where the pressure gradient that forces momentum into the (almost) right-angled daughter branch creates recirculating flow during flow deceleration (see Fig. 1.8b). It may therefore be an influential modeling choice for outflow boundary conditions.

A clinically relevant topic is the interaction of mild stenotic lesions with flow at bifurcation sites. When lesions at the femoral bifurcation are present, often all three common, superficial and deep femoral arteries end up developing significant plaque. In a previous study, the effect of a downstream SFA stenosis on flow in the bifurcation was simulated.[45] It possibly augmented flow separation at the bifurcation in case of biphasic or triphasic flow, but comparison with a control model without stenosis was not performed. A stenosis located in the common femoral artery, upstream of the bifurcation, is hypothesized to more severely impact flow separation at the bifurcation due to jet formation.[79] If true, a common femoral artery (CFA) stenosis, also if asymptomatic, may enhance plaque development or progression in the bifurcation and proximal daughter vessels, perhaps warranting earlier interventions than in current clinical practice.

Therefore, we studied how a stenotic lesion in the CFA impacts flow in the femoral bifurcation with computational fluid dynamics and particle image velocimetry. A second goal was to validate the SimVascular solver in complex conditions of transitional flow through a bifurcating artery. A control model and a stenotic model with different outflow conditions in terms of RCR compliance were investigated.

3.2 Methods

For two idealized geometries, experimental flow visualization and computational fluid dynamics were used to assess flow features. With a pulsatile flow setup mimicking physiologic flow observed in healthy participants, biplane particle image velocimetry was performed to experimentally measure 3D flow vectors in a line approximating the central lumen line of the CFA and SFA arteries. From the experimental visualization, boundary conditions were collected and used to simulate the the three-dimensional pulsatile flow with the finite element SimVascular solver. The measured vectors on the central lumen line were compared between the experimental and numerical predictions to validate the CFD method for the simulation of pulsatile flow in a bifurcating artery, with regimens of post-stenotic transitional flow during systole.

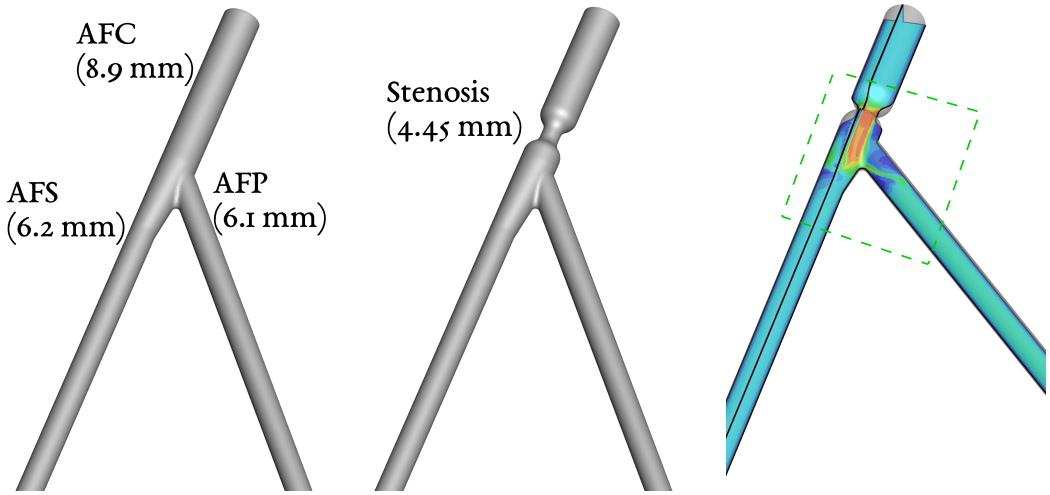

(a) Model 1 - control model **(b)** Model 2 - 75%-area stenosis **(c)** Biplane PIV measurement

Figure 3.1: The two femoral bifurcation models investigated in this study. Experimental flow visualization for the two models is performed using particle image velocimetry in the orthogonal planes drawn in the rightmost figure. The camera window size of approximately 3x3 cm is illustrated for the coronal plane.

3.2.1 Geometry

Reference values for diameters and take-off angles of the common (CFA), superficial (SFA) and profundis (PFA) femoral arteries were based on a literature study by Technical Medicine student Jeanette Tas. Only take-off angles in the plane of the bifurcation were considered, to facilitate flow visualization with particle image velocimetry. The curvature of the upstream iliac artery was not modeled due to restrictions on model size. The final geometry is shown in Fig. 3.1. Lengths of the vessels were 44, 210 and 126 mm for the CFA, SFA and PFA respectively.

A stenotic lesion was placed 0.5D (vessel diameter) upstream of the bifurcation in the second model. The stenosis was concentric in shape and had a length of 1D, with half of its length enticing the full narrowed diameter and the other half modeled as lofted transition between healthy and stenotic diameter with SolidWorks 2017 [Dassault Systèmes Solidworks Corp, Waltham, MA]. A diameter reduction of 50% was set, leading to a clinically significant area-reduction of 75%.

3.2.2 Experimental flow visualization

Transparent flow phantoms were constructed in a two-step production process. The models were printed with Acylonitrile Butadiene Styrene (ABS), over which a dearated silicone elastomer (Sylgard 184; Dow Corning GmBH, Wiesbaden, Germany) was cast. A flow loop with circulating acetone was used to clear the ABS material from the mixture and create a flow lumen in the silicone.

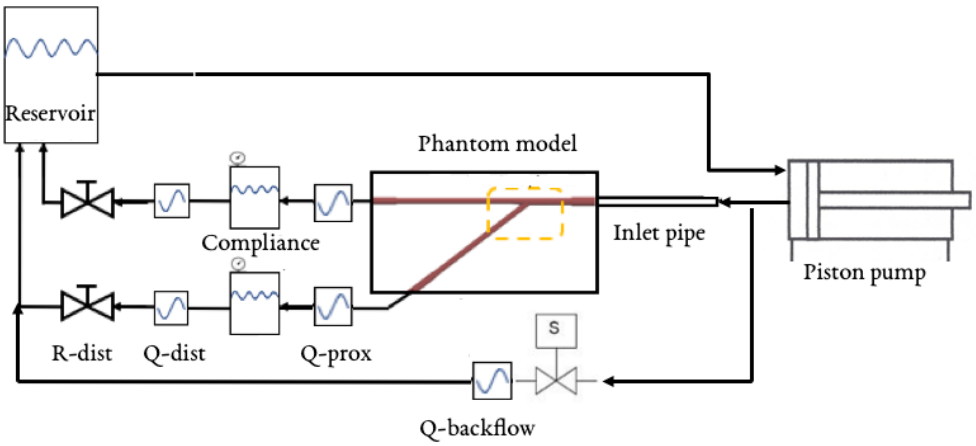

Figure 3.2: Experimental flow circuit. Q represents a flowsensor.

Next, the model was placed in a controlled flow setup, displayed in Fig 3.2. At the inlet, a hydraulic piston pump (SuperPump, ViVitro labs, Victoria, Canada) was used to enforce time-varying forward flow. Distal vascular beds were modeled as RCR-components (the proximal R was inadvertently modeled by the high resistance of the proximal flowmeters). During the backflow phase, the pump closes the inlet valve and sends a trigger signal to the solenoid valve to allow reverse flow driven by the pressurized compliance chambers, in a sense analogous to the reverse flow from the femoral artery into the renal arteries.[22] The distal flow sensors were used to set the distal resistances to desired levels and the proximal flow sensors were used to tune the compliances. A blood-mimicking fluid composed of water, glycerol and sodium iodide (47.4:36.9:15.7 weight-ratio) was used to match blood viscosity and silicone refractive index. A cone rheometer was used to confirm and determine the linear viscosity of the solution under steady, increasing shear up to strain rates of 100 s^{-1}.

Similar to our previous experiments,[80] fluorescent particles were added to the fluid and particle image velocimetry with a sheet of laserlight and a high-speed camera (1024 x 1024 resolution at an imaging plane of approximately 5x5 cm) was used to capture flow vectors. Model 1 was captured with 2000 fps, model 2 was recorded at 4000 fps with a short shutter time to capture the fast post-stenotic flow with minimal particle smearing. To be able to reconstruct three-dimensional vectors on a line approximately coinciding with the center lumen line of the SFA, a biplane measurement was performed for each setting. Image data was processed with the PIVlab toolbox[81] in Matlab. A two-pass FFT cross-correlation analysis (first pass interrogation window 64x64 pixels with 50% overlap, second pass 32x32) was performed, providing a 2D velocity vector field with approximately 0.7 mm interspacing between vectors. The vector field was ensemble-averaged over 10 cycles to produce the final PIV-result.

3.2.3 Boundary conditions

Time-dependent volumetric flow rates in healthy femoral geometries have not previously been reported. To the best of our knowledge, only data for diseased populations is available in the literature. Duplex measurements in 7 healthy volunteers aged 20-30 years (4 male) were performed to obtain normal volumetric flowrates in the CFA, PFA and SFA arteries. Time-varying volumetric flow was computed based on centerline velocity measurements, by assuming a fully developed developed and using Womersley's formula (Eq. 2.2).

A fully developed, triphasic profile was set at the inflow, based on the subject-averaged CFA inflow profile. The amplitude of the pump was set such that a flow volume of 14.6 mL was ejected during forward flow. The downstream vasculature was modeled at the outlets with 0D RCR conditions.[44] Total resistance was set such that a backflow volume through the valve of 5 mL per stroke was achieved, while the ratio of the two distal resistances was set to achieve a mean flow distribution of 40:60 for the SFA:PFA. The proximal flowmeters at the SFA and PFA turned out to have a rather high resistance due to two nozzle sections with an internal diameter of approximately 3 mm. To reach the desired backflow volume, the distal resistances had to be put at high levels to have sufficient pressure build-up in the compliances that drive backflow during the pump's retraction phase. Mean pressures of 150-200 mmHg were tolerated as the experiment focused on flow patterns.

In the duplex signals, two characteristic situations were observed. During the backflow phase in the CFA, either (1) both SFA and PFA showed concomittant backflow, or (2) backflow was dominant from the SFA, with the PFA showing minimal reversed flow. These conditions were reconstructed by distributing total compliance over the SFA and PFA outlets roughly in the same ratio as total resistance (compliance setting 1), or with distal compliance of the SFA roughly twice as high as the PFA (compliance setting 2). Model 1 was analyzed with both compliance settings, the stenotic model 2 only with compliance setting 1.

Although helpful in monitoring the experimental boundary conditions, the resolution (1000 pulses/L for the distal and backflow sensor, 4000 pulses/L for the proximal sensors) of the flow sensors was inadequate to extract accurate boundary conditions for the CFD model. The PIV vector field in the coronal plane was instead used to derive inlet and outlet flows. Near the inlet and outlets, the velocity profile over a cross-sectional line was integrated over the radius and angle according to

$$Q(t) = \int_{-\pi/2}^{\pi/2} \int_{-R}^{R} u(r,t)|r| \, \mathrm{d}r \, \mathrm{d}\theta \tag{3.1}$$

with Q the flowrate, R the radius of the cross-section, u the velocity normal to the plane, r the radius and θ the angle. Thus, the 2D velocity profile in the PIV-plane was assumed to represent the 3D cross-sectional profile. This does not imply full axisymmetry of flow, but limited axisymmetry over a semi-circle. Due to the PFA's angle in the imaged view, only lines of vectors angled to the pri-

mary flow direction were available after analysis. Flux through a plane angled to the primary flow direction was therefore evaluated, modifying Eq 3.1 to account for the elliptical area over which integration was performed.

3.2.4 Computational fluid dynamics

Mesh generation and numerical simulations were performed with the open-source SimVascular software, [42] which uses a stabilized finite element method [64] to solve the incompressible Navier-Stokes equations (body force term emitted)

$$\begin{aligned} \frac{\partial \boldsymbol{v}}{\partial t} + \boldsymbol{v} \cdot \nabla \boldsymbol{v} &= \nu \triangle \boldsymbol{v} + \frac{\nabla p}{\rho} \\ \nabla \cdot \boldsymbol{v} &= 0 \end{aligned} \tag{3.2}$$

with $\boldsymbol{v}$ the velocity field, ρ the pressure field and ν the kinematic viscosity of blood (assumed constant). The transient boundary-value problem is set with a Womersley profile imposed at the inlet, time-varying pressures at the RCR-outlets [44] and a no-slip condition at the vessel wall ($\boldsymbol{v}_{wall} = 0$). The solver uses a backflow stabilization method [65] to handle the expected mass flow reversal at the outlets. The blood vessel is modeled as a rigid wall, similar to the flow phantoms in the experimental setup.

The meshing strategy for model 1 consisted of a regular TetGen mesh with three prism layers near the vessel wall. Mesh convergence was judged by running static simulations at an inflow rate of 15 mL/s, equal to the mean of the absolute triphasic inflow (Fig. 3.3) and was considered converged when the area-averaged WSS changed no more than 1% when doubling the mesh size. For model 2, the converged mesh settings from model 1 were applied to produce an initial mesh, but the mesh was locally refined in a sphere region covering the stenosis and the downstream bifurcation. The local mesh refinement was increased until mesh convergence was reached. The model exhibited transitional flow for a steady inflow corresponding to a Reynolds number of 620, impeding mesh convergence judgment. A time-averaged solution was instead used to assess mesh convergence.

3.2.5 Comparison of piv and cfd

Results of experimental and computational flow evaluation were qualitatively compared by their in-plane velocity contours and quantitatively by a simple error comparison of velocity vector magnitude along the line that bisects the orthogonal image planes ($E = S - D$, with S the simulated result and D the measured result). [82] For the transitional post-stenotic flow in model 2, a Reynolds

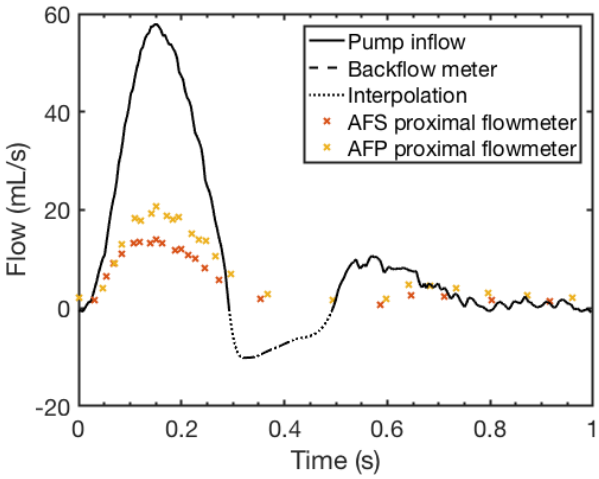

Figure 3.3: Boundary flow conditions measured by the pump and flow sensor output for the first model with compliance setting 1.

decomposition approach was taken by comparing time-averaged data over 8 cycles from the CFD solver with the time-averaged data of 10 PIV flow cycles.

3.3 Results

3.3.1 Boundary conditions

The measured inflow and outflow conditions for the PIV setup with compliance settings 1 are shown in figure 3.3. The pump's flow output for its forward moving phase has been plotted, along with the backflow sensor's discernible peak signal during the retraction phase of the piston pump. The time response of the used flowmeters was inadequate to accurately capture the backflow phase. The backflow sensor behind the valve reported non-zero flowsignals almost throughout the cardiac cycle, whereas the valve in front of it was only opened 0.2s of the cardiac cycle. In contrast, the proximal flow sensors gave no discernible peak during backflow (the sensors did not sense directionality of the flow). During the measurements, the backflow volume was therefore evaluated by watching the drop in mean flow through the distal SFA and PFA flowsensors when the backflow valve was allowed to cyclically open compared to a continuous closed state.

For the same model and flow settings, the boundary flow conditions as evaluated by the surface integral of the PIV velocity vectors (Eq. 3.1) is shown in figure 3.4 The sum of the outflow signals is additionally plotted, showing that the estimated inflow is higher than the estimated outflow. The peak inflow value is lower (40 mL/s) compared to the pump's output (almost 60 mL/s), whereas the diastolic peak is slightly higher (13 vs 11 mL/s). For the boundary conditions of the computational

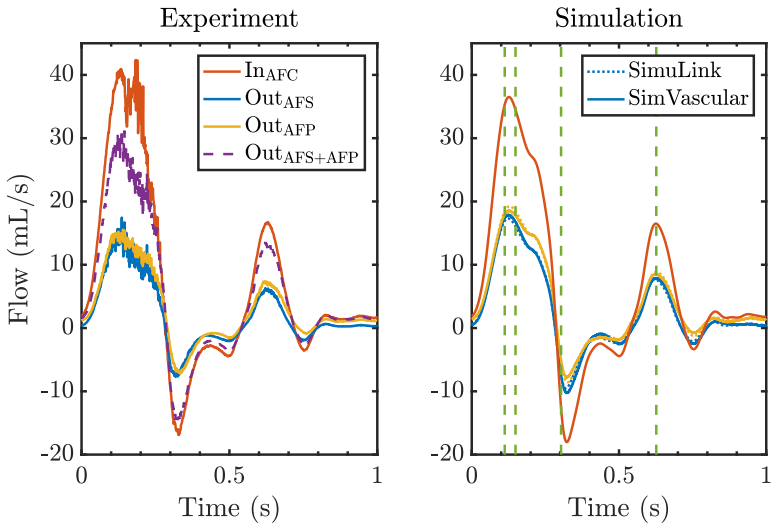

Figure 3.4: Boundary flow conditions measured by the surface integral of PIV vectors for the first model with compliance setting 1 (left). Simulated boundary conditions with a 0D-SimuLink RCR-model and the SimVascular 3D-flowsolver (right).

flow simulations, the sum of the outflow rates was used as it appeared to be less affected by noise during peak systole. The outflow sum was scaled to match amplitude of the inflow signal and RCR values were tuned to match the outflow curves in shape, as shown in the right side of Fig. 3.4.

Boundary conditions for the same model with compliance settings 2 (increased AFS compliance and decreased AFP compliance) are shown in figure 3.5. A phase shift with earlier peaking of AFP flow is present, as well as increased pulsatility of the AFS and decreased pulsatily of the AFP. Also for this compliance setting, the inflow signal is higher than net outflow, and input for the simulation was based on the net outflow signal scaled to the amplitude of the inflow.

For the stenotic model (model 2), the PIV-based boundary conditions are plotted in Fig. 3.6. These boundary conditions do satisfy mass conservation except for a slight defect at systolic deceleration. Tuning the RCR-settings of the corresponding simulation model proved difficult here, as the flow division in the 3D flowsolver deviated substantially from the 0D-RCR model in SimuLink with more flow going into the AFS (middle plot in Fig. 3.6). Tuning had therefore to be performed by running full transient flow simulations in the 3D-flowsolver with different RCR-settings to iteratively approach the measured BC.

These plots represent the BC measured in the coronal PIV-plane measurements. The AFP was not present in the sagittal measurement planes, so inflow and outflow characteristics during measurements in the sagittal plane could not be similarly assessed. For comparison with the sagittal planes, the time-averaged mean of combined outflow at the AFS and AFP for all measurements is listed in table 3.1. Outflow rates between the models and the imaging plane were variable with devia-

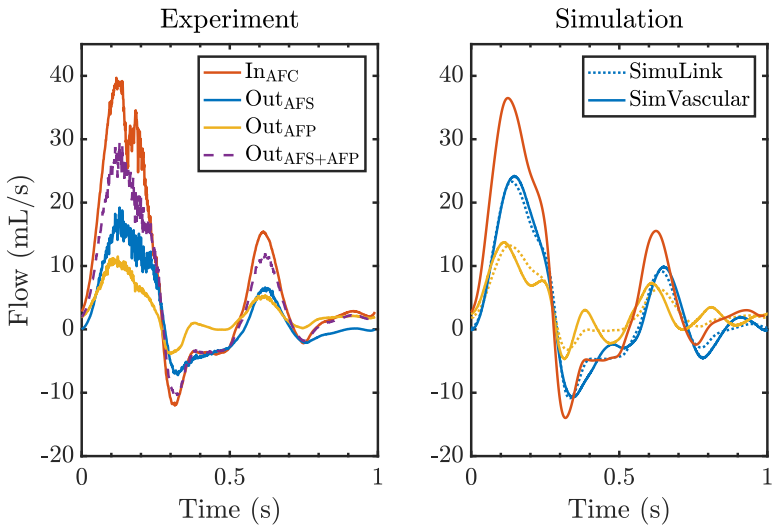

Figure 3.5: Boundary flow conditions measured by the surface integral of PIV vectors for the first model with compliance setting 2 (left). Simulated boundary conditions with a 0D-SimuLink RCR-model and the SimVascular 3D-flowsolver (right).

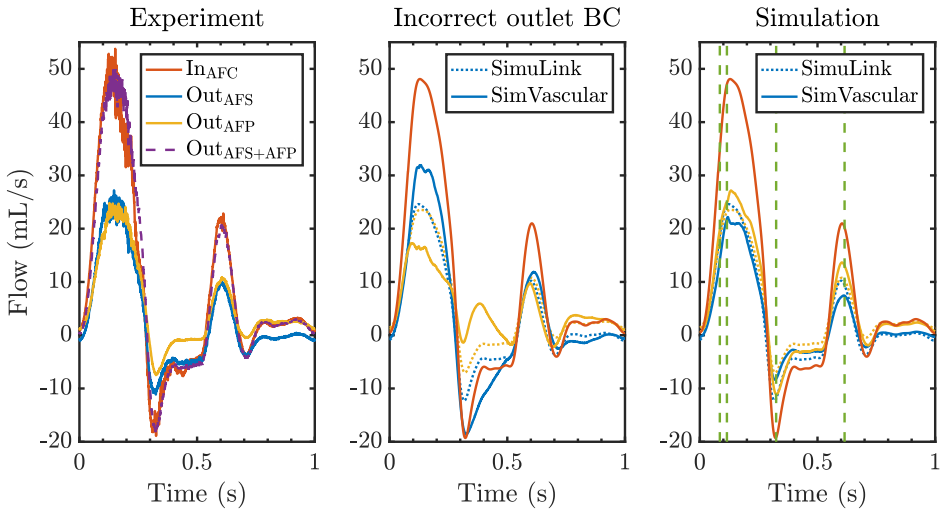

Figure 3.6: Flow BC measured by the surface integral of PIV vectors for the second stenotic model with compliance setting 1 (left). Simulated BC with a 0D-SimuLink RCR-model and the SimVascular 3D-flowsolver with equal RCR-settings (middle). Simulated BC with adapted RCR-values for the 3D-flowsolver (right).

Table 3.1: Simulation parameters

Mean outflow (mL/s)	Coronal	Sagittal
Model 1 , compliance 1	9.4	8.6
Model 1 , compliance 2	9.3	8.6
Model 2, compliance 1	7.9	8.7

tions of 10-15%.

3.3.2 Qualitative comparison

Table 3.2 shows an overview of the flow characteristics for the 3 measurements. Model 2 is characterized by higher inlet Reynolds number as its measured boundary conditions showed higher flow rates. For several key parts of the cardiac cycle, the measured and computed velocity fields in the coronal plane for model 1 (compliance setting 1) are shown in figure 3.7. Flow contours show a qualitatively good agreement for the majority of the cardiac cycle, including peak systolic and diastolic flow. At the end of peak systole and in the transition to backflow, some differences arise between the PIV and CFD results. In the PIV measurements, a subtle jet emerges at the late systolic peak, of which part is alternatively shed into the AFS and AFP at the bifurcation (Fig. 3.7b). The CFD results, in contrast, show a smooth decline after peak systole. For backflow, the CFD results show a relatively disordered transition when flow reverses, while the PIV field remains well-ordered when reversing direction (Fig. 3.7c). The small jet at peak systole for PIV and the differences in transition towards backflow displayed similar discrepancies between the CFD and PIV results for model 1 with compliance settings 2 (not shown).

Table 3.2: Simulation parameters

Input	M1, C1	M1, C2	M2, C1
BMF density (kg.m^{-3})	1212	1212	1212
BMF viscosity (mPa.s)	4.48	4.48	4.48
Mean flow rate (mL/s)	6.5	6.6	8.4
Cycle duration (s)	1	1	1
mean (max) inlet Reynolds	250(1413)	255(1413)	323(1861)
inlet Womersley number	5.8	5.8	5.8

BMF = blood mimicking fluid, M1 = Model 1, M2 = Model 2, C = compliance setting

For the stenotic model, 2D-velocity contours are shown in figure 3.8. Throughout systole, unaveraged results show turbulent fluctuations in length and direction of the post-stenotic jet (not shown).

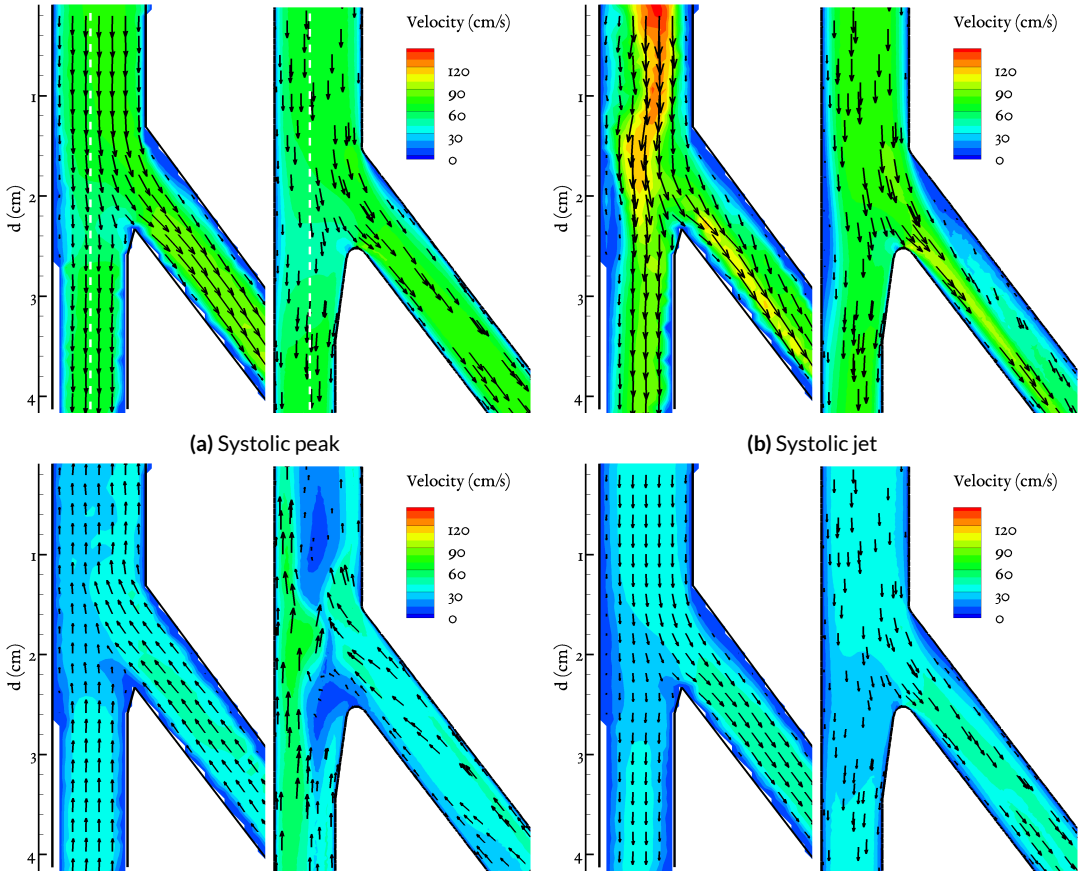

(a) Systolic peak

(b) Systolic jet

(c) Backflow

(d) Diastolic peak

Figure 3.7: PIV (left) and CFD (right) velocity fields for the control model. The time instance of the plots within the cardiac cycle is marked by dashed green lines in sequential order in Fig. 3.4

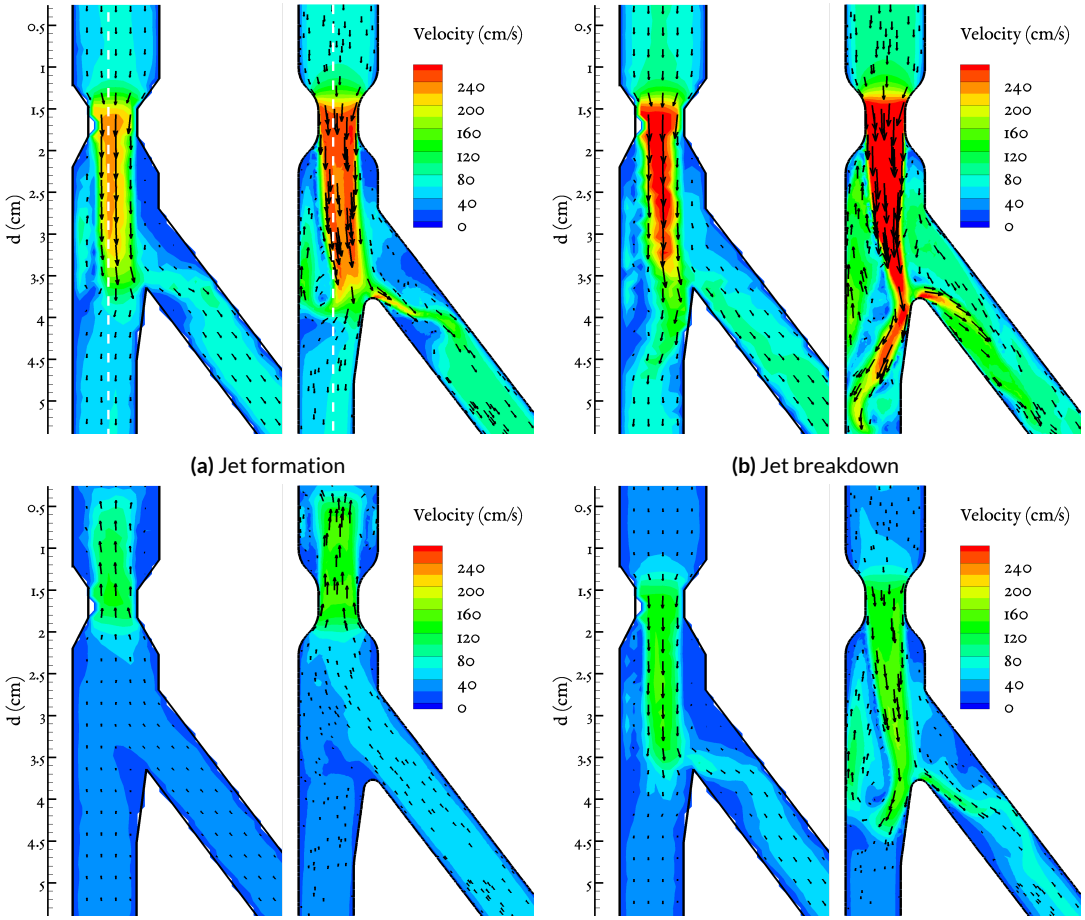

(a) Jet formation

(b) Jet breakdown

(c) Backflow

(d) Diastolic peak

Figure 3.8: PIV (left) and CFD (right) velocity fields for the stenotic model. The time instance of the plots within the cardiac cycle is marked by dashed green lines in sequential order in Fig. 3.6

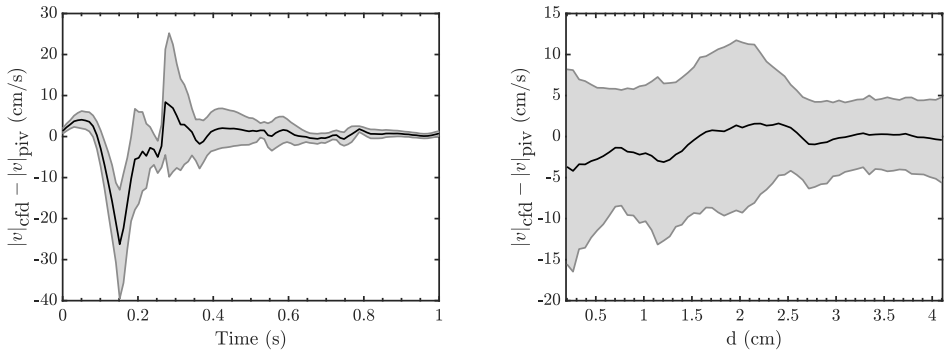

(a) Line-averaged error over time

(b) Time-averaged error along line

Figure 3.9: The error (difference) between 2D velocity magnitude in the PIV and CFD results for model 1, compliance 1. The shaded error bar shows the standard deviation of the spatial or time variation in the error.

Both CFD and PIV show time-averaged flow profiles to filter the effect of the chaotic fluctuations in the post-stenotic turbulent region. In the first two figures, the formation of the post-stenotic jet and its development is seen. Jet velocity in the throat is higher for the CFD simulations (280 vs 230 cm/s) and CFD predicts several breakdowns of the jet against the inner bifurcating wall with strong recirculation in the post-stenotic area, of which one instance is shown (Fig. 3.8b). PIV results show a more modest jet that fluctuates in direction but does not grow fully to reach the inner bifurcation wall. Also during peak diastole, a similar but gentle clash of the jet with associated transient strong recirculation in the post-stenotic area is observed in CFD predictions. Besides the jet breakdown, the velocity contours of PIV and CFD show a strong resemblance, also in the transition towards backflow.

3.3.3 Quantitative comparison

Velocity magnitudes over time along the dotted white lines (Figs. 3.7a and 3.8a) were collected for a quantitative comparison between the PIV and CFD results. Only the two velocity components in the coronal plane were used for analysis. The velocity magnitude error for model 1 with compliance settings 1 on the line averaged over time and plotted against position, and vice versa, are shown in Fig. 3.9. The main error that stands out in the time domain is the small jet formation at the end of systole in the CFA, during which the PIV model shows higher centerline velocities by about 25 cm/s. During backflow, the CFD simulation predicts higher centerline velocities, also seen in figure 3.7c. The time-averaged error shows that the error is more or less evenly distributed along the line but shows more variation in the CFA than in the SFA. Error results for model 1 with compliance settings 2 showed similar deviations (not shown).

For model 2, the magnitude of the error is larger owing to the overall higher velocities, but the er-

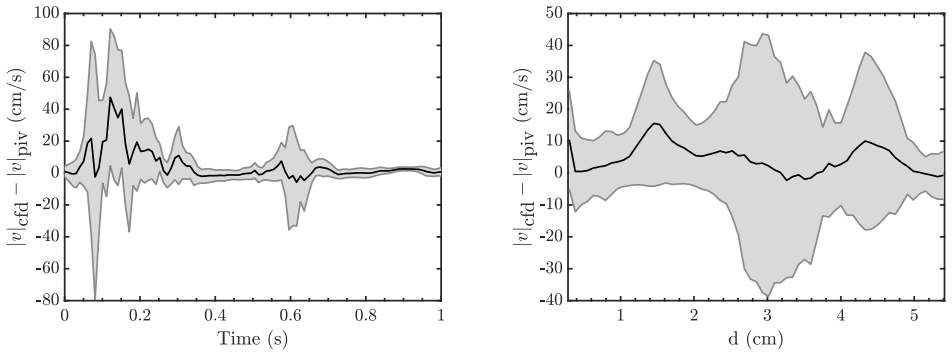

(a) Line-averaged error over time **(b)** Time-averaged error along line

Figure 3.10: The error (difference) between 2D velocity magnitude in the PIV and CFD results for model 2, compliance 1. The shaded error bar shows the standard deviation of the error in the spatial or time domain.

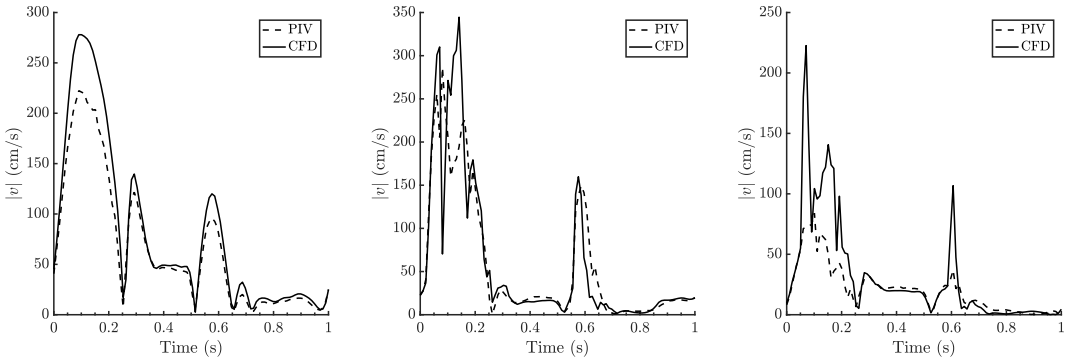

(a) Stenosis throat (d = 1.5 cm) **(b)** End of jet (d = 3.0 cm) **(c)** Proximal SFA (d = 4.3 cm)

Figure 3.11: At three individual points in the white line shown in figure 3.11, specified by distance d, velocity over time is shown.

ror is also more localized in time and space. Fig. 3.10a shows that CFD results predict velocities that are on average 40 cm/s higher than its PIV counterpart during peak systole, with less exaggerated differences during peak flow in diastole. The error is in absolute terms highest in the stenotic throat and in the jet region, illustrated by the large error bars there in Fig. 3.10b. For the three locations with highest error, pointwise velocity over time for PIV and CFD is plotted in Fig. 3.11. The plots show that CFD consistently estimates higher velocities in the throat of the stenosis (left), with less structured errors in the post-stenotic jet region (middle) and substantially higher velocities for CFD in the proximal SFA (right). The latter corresponds to the jet breakdown (Fig. 3.8b), which only occurs in the CFD predicted flow field.

3.4 Discussion

Despite heterogeneity in the flow conditions of the experimental measurements, the comparison of the PIV and CFD predicted velocity fields generate a few key insights in the simulation approach taken that need further study and refinement. Overall, the general flow characteristics in the control and stenotic models visualized with PIV were well represented by CFD simulations, generating a degree of confidence in the modeling approach to simulate complex pulsatile flow patterns in narrowed and bifurcating arteries. Still, a few characteristic differences were present between the PIV and CFD results, most of which are explainable and may be solved through different approaches.

The first is the different transition towards backflow during flow reversal. In the experimental model, this reversal occurred in a relatively smooth fashion and was only slightly stronger near the walls than in the center of the vessel. In the CFD results, initiation of flow reversal occurred prominently near the wall (3.7c), with subsequent flow reversal in the center of the lumen. This qualitative difference can be readily attributed to the Dirichlet inlet boundary during backflow, which imposes an analytic Womersley profile in which backflow is initiated at the wall. Due to the proximity of the inlet in the model (length of the CFA was 44 mm, or 5 vessel diameters), the effect of the inlet seems to extend to the level of the bifurcation also during backflow. Removal of the velocity specification at the inlet is unfeasible, except for in closed-loop boundary conditions where pressure is additionally passed on by the upstream lumped parameter network (see section 6.1), but these require additional modeling choices. Instead, the Dirichlet boundary may be moved further upstream by appending the model with flow extensions, in order for the boundary to have less impact on the domain of interest. Alternatively, the choice for a plug-flow or parabolic inlet profile may be more appropriate in cases of rapid transition to backflow. Validity of both these approaches can be tested with the current validation data.

Second, the post-stenotic jet in the stenotic model behaved more turbulent in the CFD results compared to its PIV counterpart. Two mechanisms may contribute to this difference, possibly in combination. First, the point-wise velocity comparison in the throat of the stenosis demonstrates that the CFD model exhibits consistently higher velocities in the domain, with differences as high as 25% during systole. Absolute values of PIV-results were based on the reference diameter of the AFP vessel, which can cause overestimation of velocity if the AFP was not imaged in its centerplane. The higher Reynolds number corresponds to a stronger dominance of convective forces and associated turbulence, which can lead to further jet growth and its collapse at the bifurcation wall. The observation that an analogous form of jet breakdown is also seen at lower flowrates during peak diastole (Fig 3.7d) contradicts this reasoning, though. Alternatively, the turbulent kinetics may not have been resolved on sufficiently small scales in the CFD calculations, whose computational mesh was only assessed for convergence on a lower value of steady flow (15 mL/s compared to peak systolic flow of

60 mL/s). With a current size of 1.2 million cells with about 0.3-0.4 mm edge size in the jet region, this seems a likely cause. If the viscous energy loss that occurs predominantly on these smallest scales is not modeled, the jet can retain unrealistic high rates of kinetic energy and behave in the manner observed. An estimation of the Kolmogorov microscale size for this particular problem can provide more insight in whether mesh sizing was insufficient. Assessing whether further mesh refinement reduces turbulent intensity can empirically demonstrate the problem. If true, the implications of the incorrect jet modeling on clinically relevant measures like total pressure loss and time-averaged wall shear stress should be assessed.

If these problems are resorted, most importantly the effect of the inflow boundary, a useful extension of this validation study is to investigate the duplex-derived flow quantification. For clinical application of the modeling approach of chapter 2, uncertainty of clinical duplex ultrasound can be estimated by using the validation data to assess the deviation of centerline-based volumetric flow rate from the true volumetric flow. Especially for the AFP, that in most cases can only be measured proximal to the bifurcation, this can quantify the impact of doing so on CFD's upper bound accuracy when using duplex data from sites of undeveloped flow. This discussion will conclude with a number of practical errors with the measurement set-up that limit validation accuracy due to variability in experimental conditions.

One of these is the manifestation of a jet-like structure in the PIV control model at the end of systole. The jet appeared to incidentally jump from one daughter branch to the other. Its somewhat irregular behavior was not expected in the control model, and may relate to sources of error in the current measurements. Practical issues with the experimental setup in general limited the extent to which an error analysis was useful, for example for providing an error quantification related to input uncertainties of the CFD model.[82] As can be observed in the experimental inflow profiles of the control model (Figs. 3.4 and 3.5), a sudden drop in flowrate occurred during peak systole with subsequent high frequency oscillations in its amplitude, which was not observed for the stenotic model. These seem to suggest a problem with the piston pump or at some other part in the inflow area of the flow loop. One problem during the experiments was that the level of blood mimicking fluid (BMF) in the reservoir was not high enough, as the piston pump occasionally sucked in some air from the reservoir. This air slowly built up in the pump's compression chamber from where it was manually removed a few times. The presence of air in the compression chamber induces unwanted compliance in the system, which limits the pump's output volume due to air's compressibility and may additionally have created unforeseen oscillations in flow and pressure, leading to the observed oscillations in flow rate. The unwanted compliance in the pump also generated variance across measurement conditions for different models, such as the different flowrates between coronal and sagittal recordings.

An additional error was the geometry of model 1, which was accidentally broken and glued dur-

ing production, causing the central lumen lines of the model to be slightly out of plane. This has likely caused the discrepancy between inlet and outlet mass flow rates and thus necessitates the production of a new phantom for more accurate validation measurements.

Not fully understood is the shape of the flow waveforms, which contained two phases of backflow. The introduction of a short backflow phase after the diastolic peak is likely attributable to the pump's aortic valve, which allows flow leakage that is intentionally comparable to the heart's aortic valve. The presence of a quadriphasic profile is occasionally seen on duplex measurements, so its presence is not necessarily unrealistic. The second unexpected backflow feature is the short increase in backflow before the onset of diastolic forward flow. The dynamics of the backflow valve closure at the end of backflow may play a role, perhaps generating a small backflow boost by pushing fluid through the valve when closing.

3.5 Conclusion

If both complicating factors of transitional flow and an inlet close to the arterial location of interest are absent in clinical research applications of the CFD method tested, this validation study suggests that the simulations predict the characteristics of the flow field accurately if inputted with the right geometry and boundary conditions. It therefore legitimizes the effort of performing studies on the simulation's predictive ability for disease progression and treatment complications. For the present case of post-stenotic transitional flow with a Dirichlet inlet close to the domain of interest, the modeling shortcomings need further addressing before the effect of differential outlet compliance on wall shear stress can be answered. Also for a more informative input uncertainty validation of the CFD model, these topics should be resorted and the experimental set-up better controlled.

In design, one plus one equals three or sometimes more.

Josef Albers

4

Serial stenotic lesions

4.1 Introduction

Patients with critical limb ischemia are often diagnosed with multiple stenotic lesions in the femoropopliteal trajectory, possibly combined with lesions in the iliac or tibial arteries. Treatment of lesions that significantly impede blood flow to the periphery are indicated to improve conditions for wound healing. Even in ischemic lesions that warrant amputation, pre-surgical revascularization can be beneficial to optimize oxygen and nutrient supply to the newly created stump. However, patients with critical limb ischemia typically have significant co-morbidity, which carries increased procedural risks of revascularization. For isolated stenoses, well-established criteria are present to assess hemodynamical significance of a stenosis (peak systolic velocity ratio (PSVR) > 2.5 on duplex or an area-reduction of over 75% on anatomic imaging)[4], allowing for clear cut-offs in clinical decision making. In the typical CLI patient, multiple non-critical stenoses, based on their individual assessment, may however combine to induce a significant hemodynamical impairment. Also for patients with intermittent claudication (IC), a subset of patients may present with multiple borderline (50-70%) stenoses.

A criterium or formula for when multiple insignificant stenoses combined become hemodynamically limiting, and thus warrant treatment, is currently lacking. Also for other areas, such as the coronary and renal arteries, a decent understanding of the combined hemodynamic effect of two closely spaced stenotic lesions would aid in making proper treatment decisions. Especially because in these areas, the flow-limiting effect of the lesion can hardly be judged by patient symptoms, which are hard to quantify for cardiac and renal flow impairment. For multiple stenoses, duplex PSVR[69]

and anatomic evaluation are inadequate to quantify their combined effect. Accurate evaluation is currently only possible by obtaining the pressure gradient over the lesions through invasive pressure measurements. For peripheral arteries, however, no expert consensus currently exists on the definition of a hemodynamically significant stenosis on the basis of pressure drops.[83] Official guidelines[4] define a threshold of 5- 10 mmHg for systolic pressure in resting flow or 10-15 mmHg in hyperemia. More recent recommendations for iliac stenoses recommend a cut-off of 10 mmHg for systolic pressure at rest flow and 20 mmHg during hyperemia.[83]

The pressure-flow characteristics of isolated concentric and eccentric stenoses of various shapes have been documented well.[84] For steady flow, the pressure drop can be related to the flow rate by equation 4.1, in which the constants k_1 and k_2 depend on stenosis geometry. The first linear term reflects the energy loss due to viscous forces and is dominant for mild stenoses (say less than 50%) or low Reynolds numbers. The second term reflects non-linear energy losses, caused by flow recirculation and possibly turbulence behind the stenoses, and it is the main constituent of the pressure drop in isolated significant (75% area-reduction) stenoses. Experimental measurements on the effect of eccentricity on the constants have been performed. For moderate flow rates (Reynolds numbers ranging from 100-1000),[85] eccentricity does not play a major role and the pressure drop is determined mainly by the area reduction and morphologic shape (e.g. circular opposed to non-circular). For higher flow rates (Reynolds numbers >1000), stenosis eccentricity does become important, giving roughly twice as high pressure drops for circular eccentric stenosis compared to its concentric counterpart.[86]

$$\Delta P = k_1 Q + k_2 Q^2 \tag{4.1}$$

Multiple studies have addressed the effect of two sequantial concentric stenoses in steady flow. Whether their individual resistance can be mutually added depends on whether the first stenosis on its own produces a significant pressure drop due to jet expansion (a convective energy loss), and on whether the second stenosis is close enough to interfere with relaminarization of the jet. This depends on the interstenotic distance, Reynolds number and stenosis severity. For increasingly smaller distances between the stenoses (less than the relaminarization length, say at most 10D for most stenoses and flow rates), the total pressure drop becomes less than the sum of the two individual stenoses, due to the convective energy losses of the first stenosis being limited by the second. Generally speaking, the effect of two isolated regions has been reported to linearly add up when the interstenotic distance is more than four diameters for severe and significant concentric stenoses (> 90%), and more than one diameter for insignificant stenoses (50%),[84] although these distances also heavily depend on flow rate.

Moreover, these observations were only made for concentric stenoses, not for more common eccentric stenoses. The convective energy loss of eccentric stenoses is more profound and more com-

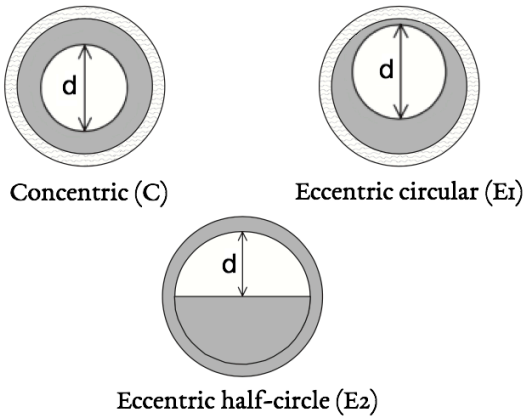

Figure 4.1: Axial cross-section of the three stenotic shapes modeled: one concentric and two eccentric stenoses. The lumen diameter d equals D/$\sqrt{2}$ for the upper circular geometries, and D/2 for the lower half-circle shape. Adapted from Dodds [85]

plex, which may produce unforeseen interactions between multiple eccentric stenoses. This study aims to investigate these effects for two non-significant stenoses through computational simulations, with the goal to provide clinical directions if possible.

4.2 Methods

Starting from three basic stenotic shapes, the pressure drop over a wide set of serial stenotic configurations under a steady inflow condition was investigated by CFD. All three stenoses types, shown in Fig. 4.1 have a 50% area reduction, so the circular geometries have a diameter d of D/$\sqrt{2}$. The length of the stenoses was arbitrarily chosen as 1D, which excludes the smooth transition region. To minimize the influence of boundary conditions, a healthy inflow part of 3D and an outflow part of 10D were added to the models.

Flow was simulated through the three stenoses in isolated setting and through a combination of two stenoses with three different interstenotic lengths: 0D, 3D and 6D (Fig. 4.2). For the 0D setting, no healthy vessel is in between the stenosis and the stenosis is essentially a single stenosis of double length. For the 3D and 6D scenarios each, nine combinations of first and second stenosis shape are possible. In addition, for the settings with two eccentric stenoses, the rotation angle can be varied from 0-180°. For these cases, rotation angles of 0, 90 and 180 degrees were chosen, yielding a range of 17 unique combinations for the 3D and 6D distances each. Combined with the single and double-length stenosis, a total of 40 stenosed geometries result. The geometries were designed in SolidWorks, with lofting applied to smoothly bridge healthy and stenotic parts.

The open-source SimVascular software [42] was used to mesh the inner geometry with tetrahedral

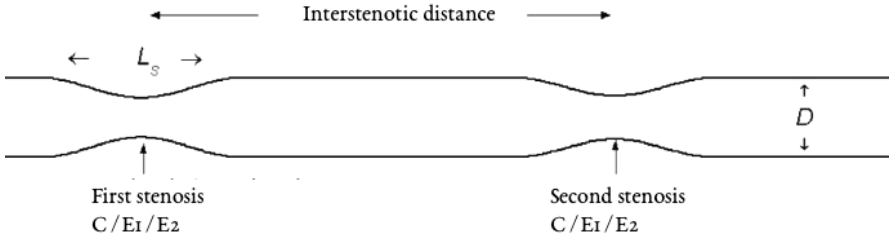

Figure 4.2: For serial stenotic lesions, the type of first and second stenosis is varied, as well as three interstenotic distances. Adapted from Bertolotti et al. [69]

elements, combined with a thin three-element prismatic boundary layer. Blood was considered as a Newtonian fluid and the vessel walls were modeled as rigid. A parabolic inflow profile corresponding to a Reynolds number of 933 (based on mean velocity) was set. For this flow rate, the stenoses under investigation are subclinical (pressure drop <5 mmHg) and turbulent effects play a minor role, if any (Reynolds number behind the stenosis 1800). At the outlet, a resistance boundary was prescribed that yielded a distal pressure of 80 mmHg, although other values would not effect the pressure drop across the stenosis in the absence of wall motion. The simulation settings are presented in table 4.1. Solutions were considered converged if the combined mass and momentum residual was lower than 1×10^{-4}. The end point was the pressure difference between the inlet and outlet boundary. Mesh convergence was therefore assessed by doubling the mesh size until the pressure difference changed no more than 1%.

Table 4.1: Simulation settings

Parameter	Value
Blood density (kg.m^{-3})	1059
Blood viscosity (Pa.s)	3.5×10^{-3}
Inflow rate (mL.s^{-1})	15
Reynolds number	933

4.3 Results

For a single stenosis with a length of 1D, the pressure drops were of insignificant value (<5 mmHg). The pressure drop of the half-circle (E2) stenosis was markedly higher than the other two shapes (table 4.2). The velocity contours in Fig. 4.3 reveal that peak velocity for all three stenoses are of sim-

ilar order at about 1400 mm/s. The E1 stenosis generates one recirculation region at the site of area expansion, after which flow stabilizes. The E2 stenosis, in contrast, generates a more pronounced second area of stagnant flow further downstream, at the opposite site of the first recirculation zone.

Table 4.2: Pressure drops for a single stenosis

Stenosis shape	Abbreviation	Pressure drop (mmHg)
Concentric	C	2.3
Eccentric circular	E1	3.0
Eccentric half-circle	E2	4.7

For the double stenoses, the combinations that involve two E2 stenoses show the highest pressure drops. For all combinations, the pressure fall does not exceed the sum of the two individual stenoses combined. Further observations include that doubling the length of a stenosis (the 0D combinations) increases the pressure drop only marginally compared to the pressure fall for the original length in table 4.2. When inspecting the effect of interstenotic distance (3D vs 6D), it is clear that increasing the spacing between the stenoses leads to a higher pressure drop, although this effect is not very strong for most cases. One exception is the C and E2 combination, which has a higher pressure drop for a 3D interstenotic distance (6.3 vs 5.8 mmHg). Finally, the effect of varying the rotation angle between two eccentric stenoses is relevant for most geometries. A 90 degree angle is worst for all cases, with a slightly more pronounced effect for 3D interstenotic distances compared to 6D. The rotation effect is highest for the combination of two E2 stenoses with a 90 degree rotation, giving a 20% increase in pressure drop (from 6.4 to 7.6 mmHg) compared to a 0 degree rotation.

All these effects have a relatively small influence on the pressure drop compared to the shapes of stenoses involved. To illustrate, the last column in the table presents the percentage of the pressure drop compared to the sum of the pressure drops across the individual stenoses taken from table 4.2.

$$K_s = \frac{\Delta P_{\mathrm{ss}}}{\Delta P_{\mathrm{s1}} + \Delta P_{\mathrm{s2}}} \tag{4.2}$$

with ss for the serial stenoses combination and s1 and s2 for the individual stenoses. This ratio is relatively constant across all combinations (excluding the 0D stenoses, which are in fact single stenoses), with a mean and standard deviation of 0.8 ± 0.06.

Figure 4.4 shows velocity contours for a selection of double eccentric models. The first two models show that a second E2 stenosis generates stronger secondary flow in the poststenotic region relative to the same configuration with an E1 second stenosis. The second (180 degrees) and third model (90) highlight the effect of the relative angle between the stenoses. In the 90 degree model, very

Table 4.3: Pressure drops for the various combinations of double stenoses

First stenosis	Second stenosis	Interstenotic distance	Rotation angle	Pressure drop (mmHg)	Ks
C	C	0D	-	3.0	0.63
		3D	-	3.9	0.82
		6D	-	4.2	0.89
	E1	3D	-	4.2	0.80
		6D	-	4.5	0.84
	E2	3D	-	6.3	0.89
		6D	-	5.8	0.82
E1	E1	0D	-	3.3	0.56
	C	3D	-	4.2	0.84
		6D	-	4.6	0.89
	E1	3D	0	4.2	0.72
			90	4.9	0.82
			180	4.8	0.81
	E1	6D	0	4.8	0.81
			90	5.0	0.85
			180	4.7	0.79
	E2	3D	0	5.6	0.73
			90	6.7	0.87
			180	5.5	0.72
	E2	6D	0	6.1	0.79
			90	4.61	0.87
			180	5.9	0.73
E2	E2	0D	-	4.9	0.52
	C	3D	-	5.6	0.80
		6D	-	6.1	0.86
	E1	3D	0	5.5	0.72
			90	6.1	0.80
			180	5.9	0.77
	E1	6D	0	6.4	0.84
			90	6.4	0.84
			180	6.3	0.82
	E2	3D	0	6.4	0.68
			90	7.6	0.81
			180	6.3	0.67
	E2	6D	0	7.2	0.77
			90	7.8	0.83
			180	7.0	0.75

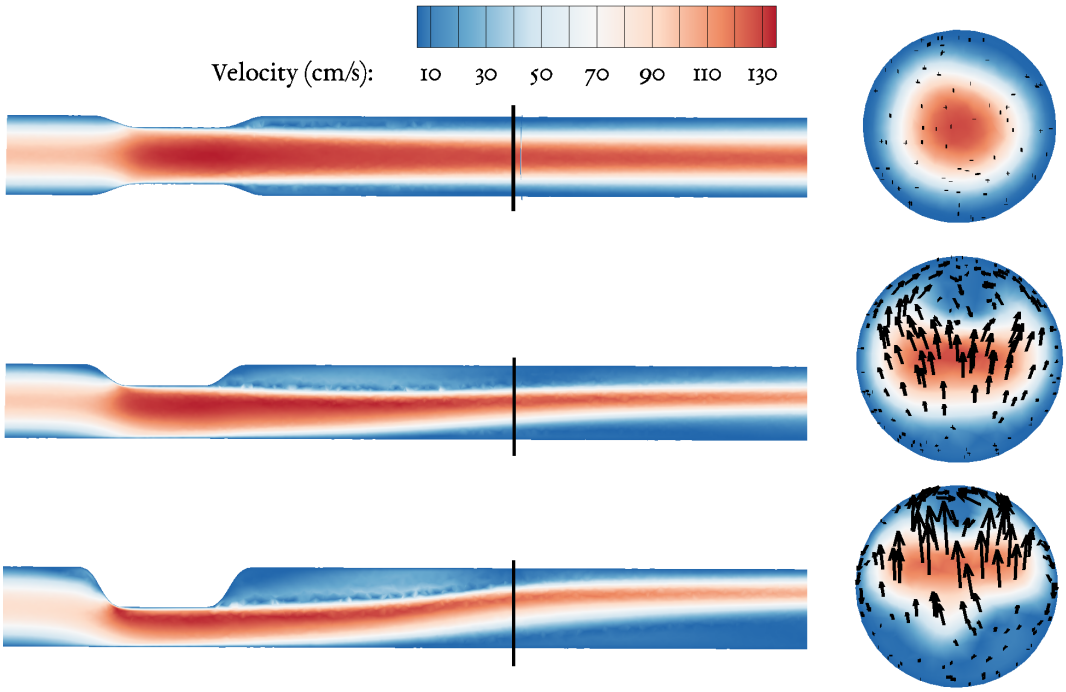

Figure 4.3: Velocity contours of single stenotic lesions in two planes. From top to bottom: C, E1, E2 stenosis. The axial plane on the right was taken at approximately 3D behind the stenosis, marked by the black line. Secondary flow vectors in the axial planes are scaled to magnitude, with a maximum of 92 mm/s in the E2 model.

strong secondary flow vortices reside in the second stenosis, generating strong helical flow in the poststenotic region. The second (3D) and fourth (6D) model differ in the interstenotic distance. The 6D model exhibits an additional recirculation zone in the interstenotic region.

4.4 Discussion

Deciding whether to treat two subclinical stenoses that are in close proximity to each other can be a tough decision, as their interaction is not a trivial addition of their individual effect. Traditional measures like the Duplex PSVR do not reflect the potentially doubled pressure loss from two stenoses, but can only assess the severity of the more severe stenosis.[69] The results of the present study suggests that for stenoses of equal anatomic and functional severity, eccentricity is the most important predictor of whether two subclinical stenoses combined bear hemodynamical significance. Especially eccentricity interpreted as irregular stenosis shape (non-circular) negatively impacts the energy loss through a stenosis, in line with previous measurements for a single stenosis.[86] In none of the cases was the pressure drop across two stenoses worse than the sum of their individual effects. In fact, the most important observation is that the pressure drop over two lesions in close proximity

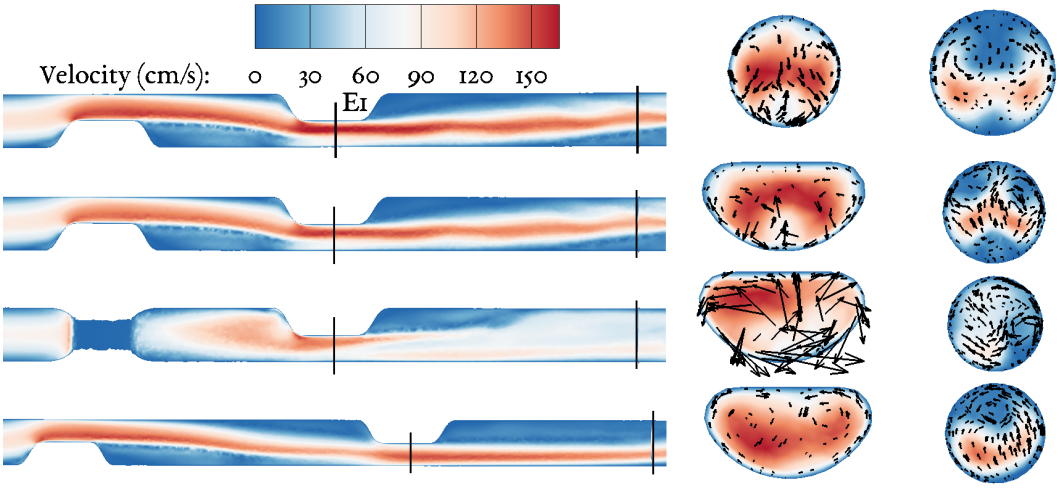

Figure 4.4: Velocity contours of four double stenotic lesions in two planes. All stenosis are E2 shape if not marked different. The axial planes on the right were taken through the second stenosis and approximately 4D downstream of the second stenosis, marked by the black lines. Secondary flow vectors in the axial plane are scaled to magnitude, with a maximum of 580 mm/s in the second stenosis of the 90 degree model (third from the top).

was equal to 75-85% of the sum of the pressure drop over the individual stenoses in isolated setting.

Of all combinations simulated, about half of the double lesions gave a possibly significant pressure drop of >5 mmHg for steady flow. In all of them, the E2 stenosis was involved, which is not surprising as this stenosis on its own produced a near significant pressure drop of 4.7 mmHg. Whether these pressure drops would be of clinical significance is hard to say, as it depends on the flow rate increase upon vasodilation in demanding conditions. For systolic flow rates, in which the flow rate is typically more than twice the current flow rate (15 mL/s), it is very likely that this pressure drop amplifies towards significant values >10 mmHg, as the pressure drop increases with the square of flow in this regime. For patients with critical limb ischemia, typical flow rates are probably lower and thresholds for significance may not be reached. Another complexity for increasing flow rates for the present case of multiple stenoses is that the domain of influence of the first stenosis is likely to grow. A larger part of this domain is then captured by the second stenosis, which implicates that the combined effect of the two stenoses becomes less severe. The scenario of increased flow is a natural choice to simulate as next step.

For arterial sites that experience relatively steady flow, like the coronary and renal arteries, the current results represent a reasonable approximation to the physics involved. The mathematical analysis by Young [84] of the pressure losses involved in unsteady flow predicts that for modestly unsteady flows, the mean pressure loss is closely resembled by the pressure loss of a steady flow. For modest pulsatile flows where peak flow equated twice the mean flow value, in-vitro pressure measurements of a double stenosis indeed have confirmed that pressure drops over two 70%-area stenoses are simi-

lar for pulsatile and steady flow.[69]

For modeling stenoses in the arteries of the leg, a separation may be useful on the basis of clinical Rutherford or Fontaine classification. Patients with critical limb ischemia (CLI) typically have monophasic flow which is probably well approximated by steady flow simulations. Patients with intermittent claudication are more likely to exhibit stronger flow pulsatility, in which case the physiology of pressure drops becomes more difficult and the simulation of pulsatile flow may be necessary. Regions of flow separation between the stenoses may quickly grow during systole and detach during flow deceleration, after which they are convected through one of the stenoses. Additionally, wall motion may become a relevant contributor to pressure dynamics, especially since the cross-sectional area transitions create highly localized differences in pressure. The current CFD solver contains a coupled momentum method that integrates a linearized description of wall motion into the Navier-Stokes equation[67] and this method has been validated against in-vitro pressure measurements in a stenotic phantom with deformable wall.[68]

Multiple stenotic lesions are far more common in patients with CLI, though. For the most relevant clinical application of CFD the use of steady flow models may therefore be appropriate. Although the current simulations demonstrated a simple 80% rule for two 50% stenoses, the total pressure drop probably becomes increasingly unpredictable for lesions of differing grades, shape and flow rates. Clinical application of CFD based pressure predictions in CLI patients needs validation with invasive pressure measurements. A prospective cohort study can be set up in which CLI patients planned for revascularization are subjected to additional pressure measurements during endovascular treatment. Such a study can simultaneously address whether pressure gradients have the ability to predict improved clinical outcome of intervention. For patients with CLI, the presence of distal tibial stenoses, which are hard to detect, may complicate the overall value of pressure gradients. Nonetheless, CFD should in theory be able to quantify the contribution of stenoses in the femoropopliteal arteries to a reduced ankle-brachial index without prior knowledge on the status of the tibial arteries.

Water is fluid, soft and yielding. But water will wear away rock, which is rigid and cannot yield. As a rule, whatever is fluid, soft, and yielding will overcome whatever is rigid and hard.

Lao Tzu

5

Patient-specific simulations of proximal edge stenosis of covered endografts

5.1 Introduction

For above-the-knee femoropopliteal disease, endovascular devices are seemingly reaching a point where their long-term patency results are at level with traditional venous bypass surgery. Even for total chronic occlusions (TASC D lesions if extending 20 cm in length[8]), the heparin-bonded Viabahn covered stentgraft (Gore and associates, Flagstaff, AR, USA), placed with the percutaneous intentional extraluminal revascularization technique (PIER),[87] exhibits patency comparable to bypass surgery with 3-year primary-assisted patency rates of 71%.[88] Two-year results of the randomized SuperB trial (Surgical bypass versus percutaneous bypass trial), recently accepted for publication, demonstrate similar patency and better 30-day quality of life for the endovascular approach due to a faster recovery rate.

Still, with two to three-year primary patency rates of of 59-63%[89,88] for the Viabahn covered stentgraft, complications and re-interventions are common in this group. Especially stent thrombolization can have a major patient impact if intra-arterial urokinase treatment is complicated by a hemorrhage-induced compartment syndrome, necessitating two surgical operations to relieve and in a later stage close the pressurized compartment. Stent thrombolization is likely related to edge stenosis of the Viabahn, which is frequently seen at the proximal edge or in the native vessel immediately proximal to the stentgraft. Although possibly less common after (1) the manufacturer has added a contoured proximal edge to prevent inwards folding of the stent, and (2) care is taken to

limit oversizing of the stent compared to the healthy vessel lumen to 20%, the problem still persists and appears to predispose towards stent thombolization and occlusion if not managed.[90] High resolution ex-vivo imaging of the Viabahn deployment in ex-vivo porcine model with subsequent CFD still showed malappositioning of the contoured proximal edge of the stent, with a miniscule flow lumen between the graft PTFE lining and arterial wall. Steady-flow CFD showed multidirectional regions of recirculation in these spaces, associated with areas of low wall shear stress and hypothesized to be a key initiation site of edge stenosis.[12]

Occlusion of the SFA commonly extends proximally upwards at or close to the level of the femoral bifurcation, as the proximal SFA is not accompanied by major sidebranches in most patient anatomies. The proximal edge of the Viabahn is therefore placed in the proximal SFA at the level of the bifurcation or slightly downstream of it. Therefore, flow disturbances induced by the flow division at the bifurcation may relate to thrombolization of the Viabahn stentgraft downstream of the bifurcation. If areas of recirculating flow persist over the cycle at the level of the contoured edge, thrombosis that was initiated at the malappositioned edges may further develop into full thrombolization of the stentgraft. If true, visualizing flow patterns after stent placement can help assess whether treatment was successful on local hemodynamic grounds and quantify a patient's individualized risk on complications. Patient follow-up and concomittant anti-coagulation therapy can then be optimized on a patient level. In complement, predicting how endovascular procedures will change local flow patterns before treatment has potential to improve treatment planning. To explore the clinical usability of CFD for both strategies in case of SFA treatment with the Viabahn, two cases for which CFD has been applied retrospectively will be discussed.

5.2 Methods

The two patient-specific simulations presented here have been performed by the CFD pipeline outlined in chapter 2. In summary, segmentation is performed with vmtkLab and meshing and CFD computations with the SimVascular software. The mesh was composed of tetrahedrals and a prismatic boundary layer, with a local refinement at the femoral bifurcation (twice as many tetrahedrals per cubic mm). The mesh was considered converged if area-averaged WSS for steady flow at the first 5 cm of the proximal AFS changed no more than 5% with a doubling of mesh size. A Womersley profile was imposed at the AFC inlet, based on duplex-derived flow rate. The distal AFS and AFP vasculature was modeled with RCR-outlets, tuned to match duplex flow rates. The accuracy of tuning will be reported per individual case. Starting from the steady state solution for the mean flow rate, five cardiac cycles were simulated to reach a periodic solution, from which the last was used for analysis. Velocity streamlines and contours at the femoral bifurcation and in the proximal SFA will be visualized for parts of the cardiac cycle. The time-averaged magnitude of wall shear stress

(TAWSS) over one cycle is additionally shown, evaluated as

$$\mathrm{TAWSS} = \frac{1}{T}\int_0^T |\tau_\mathrm{w}|\,\mathrm{d}t \tag{5.1}$$

5.3 Case 1 - recurrent proximal edge stenosis

A 63-year old female with a persistent ulcus cruris on her right lower leg was treated in September 2014 for two total occlusions located in the right external iliac artery (EIA) and the superficial femoral artery (SFA). Besides unilateral PAD, the patient had no other cardiovascular history and had ceased smoking. After surgical groin cutdown and femoral access, both occlusions could be successfully subintimally passed and treated with angioplasty and the heparin-bonded Viabahn stentgraft. A 10 x 0.8 cm Viabahn was deployed in the EIA immediately downstream of the bifurcating internal iliac artery, and for the SFA,a 25 x 0.6 cm Viabahn was deployed at the level of the adductor channel up to 3-4 cm downstream of the bifurcating profunda femoral artery. A thromboendarterectomy of the common femoral and remaining 3-4 cm SFA was performed and sutured in conjunction with synthetic patch angioplasty. Completion angiography demonstrated successful vessel revascularization and three patent tibial arteries.

Dual anti-platelet was prescribed for 3 months and regular follow-up using duplex ultrasound showed good patency without signs of obstruction in the EIA and SFA trajectory at 1.5 and 6 months post-treatment. At 8 months after treatment, the patient presented with a sudden increase in claudication symptoms due to secondary occlusion of the SFA and the fibular artery, successfully resolved with intra-arterial urokinase treatment. A proximal edge stenosis of the SFA Viabahn was seen on angiography and treated with balloon angioplasty (not shown). At the start of 2017, two weeks after a switch from clopidogrel to acetylsalicyclic acid due to side-effects, a second occlusion of the SFA Viabahn occurred. The occlusion was again treated with urokinase treatment, complicated by a hemorrhage-induced compartment syndrome. Recurrence of the proximal edge stenosis was observed and treated with a drug-eluting balloon (DEB, Fig. 5.1). Following fasciotomy and split-skin graft procedures, therapeutic anticoagulation (acenocoumarol) was prescribed to prevent future thrombotic events. The distal vasculature was evaluated with CTA (Fig. 5.1c) and duplex in this period, both showing excellent patency of the SFA without restenosis and good distal run-off. Nonetheless, routine duplex follow-up demonstrated occlusion of the SFA Viabahn half a year later, which has been left untreated in the absence of significant symptoms.

Flow simulations To explore if local flow patterns could have helped in predicting the third thrombotic event, pulsatile CFD simulations were performed based on the CTA and duplex scans made within two months after the drug-eluting balloon angioplasty. The segmented vessel lumen is

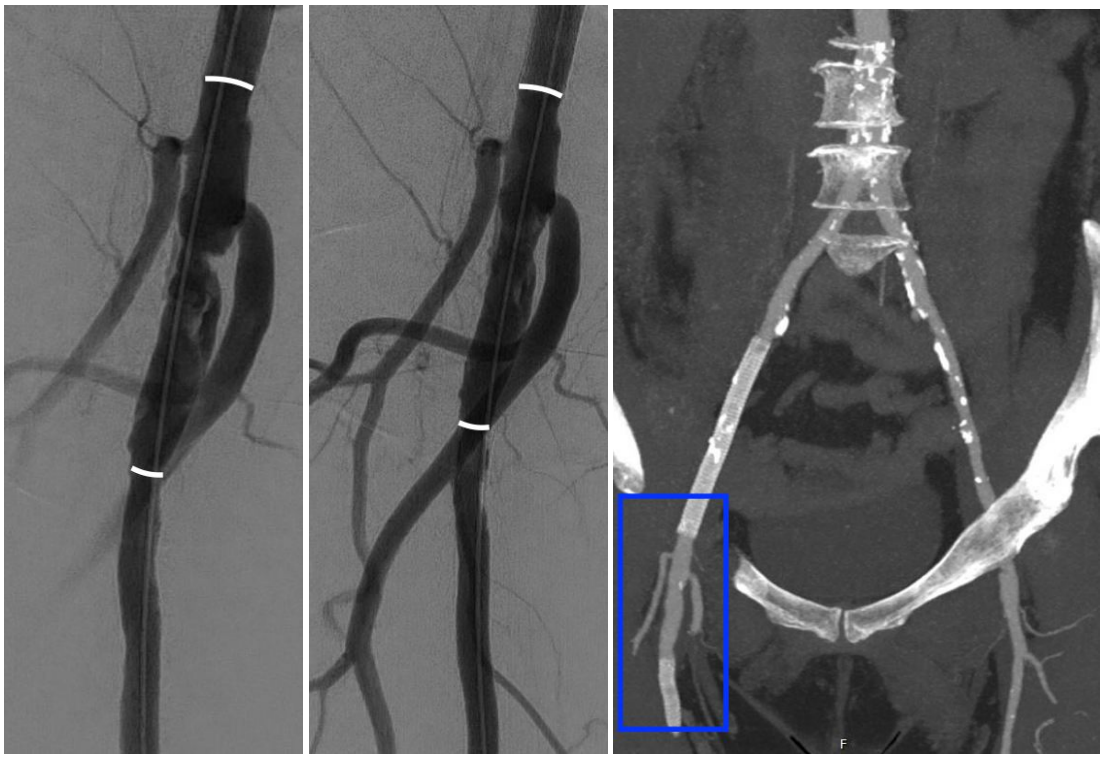

(a) DSA before DEB **(b)** DSA after DEB **(c)** Coronal CTA-slice 1 month after DEB

Figure 5.1: Case 1 - Femoral bifurcation scans. Periprocedural DSA scans (Jan '17) show the vessel lumen before and after angioplasty with a drug-eluting balloon (DEB). The CT-scan confirms that no restenosis had occurred 1 month after DEB treatment. The white lines in the DSA scans mark the distal edges of the EAI and SFA Viabahn stentgrafts.

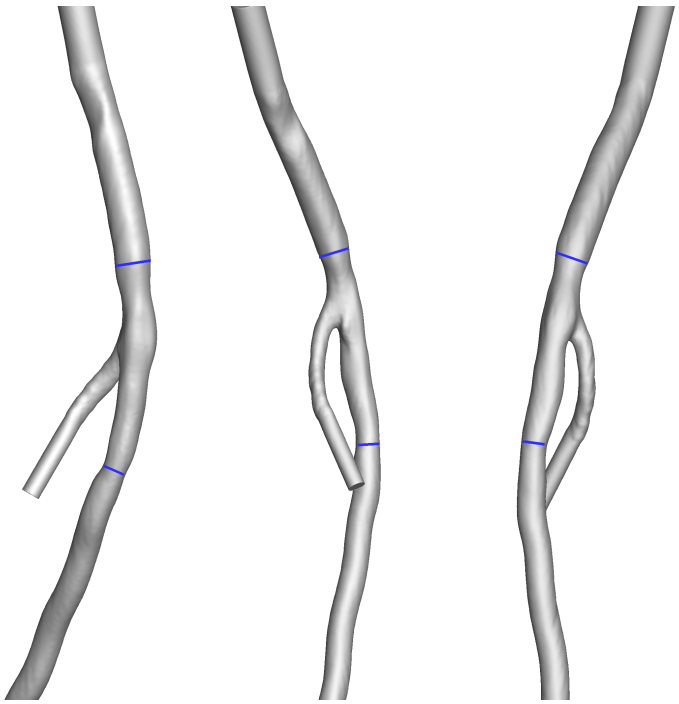

Figure 5.2: Case 1 - anatomy. The two blue lines demark the distal end of the EIA Viabahn and the proximal edge of the SFA Viabahn.

shown in Fig. 5.2. A slight narrowing of the EIA Viabahn can be seen, caused by minor calcification. Otherwise, the segmented trajectory is unobstructed, with some subtle diameter variations at the proximal SFA, where a synthetic patch constitutes part of the vessel wall and which has been treated with a drug eluting balloon 1 month prior to the CT.

On duplex-derived flowrates (Fig. 5.3 left), a very brief phase of backflow was present in the CFA, but was not visible in the SFA and PFA signals. It was assumed that this backflow arose from the PFA when tuning the RCR values, as the PFA centerline velocity profile is captured in a region of undeveloped flow close to the bifurcation, possibly in a region where flow does not reverse. Otherwise, inflow equaled outflow within small limits and the tuned outflow signals matched well with duplex. Overall simulation settings are presented in table 5.1.

Instantaneous velocity streamlines and contours for three key phases of the cardiac cycle are shown in Fig. 5.4. During flow deceleration, flow separates from the wall in the proximal SFA proximally at the outer side of the bifurcation, and a bit more distal at the inner side of the bifurcation. Less consistent regions of flow separation are also present behind the CFA narrowing and more distal in the SFA, which are contained within the heparin-bonded Viabahn graft.

Cycle-averaged wall shear stress is visualized in Fig. 5.5, clearly reproducing the adverse focal sites of flow separation in the proximal SFA, with strikingly low WSS values smaller than 0.05 Pa. The lo-

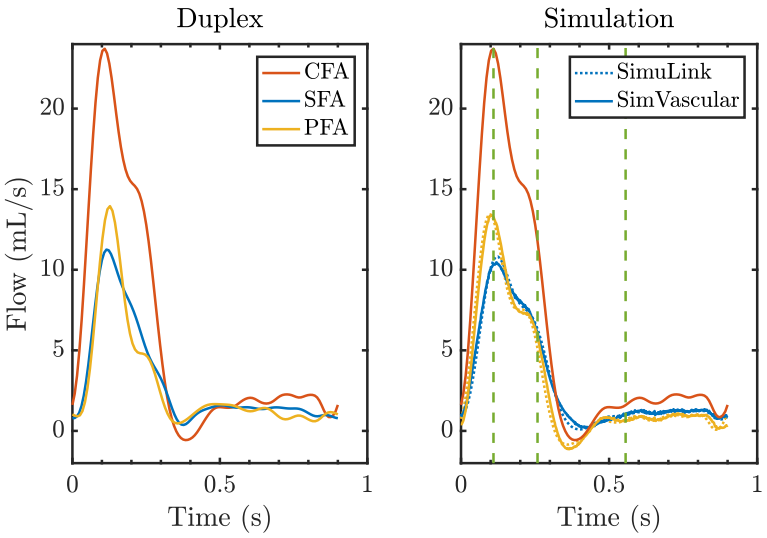

Figure 5.3: Case 1 - measured and simulated boundary conditions. The CFA signal is used as input for the simulation and therefore equal. Green dotted lines mark time instances for which streamlines are plotted in figure 5.4.

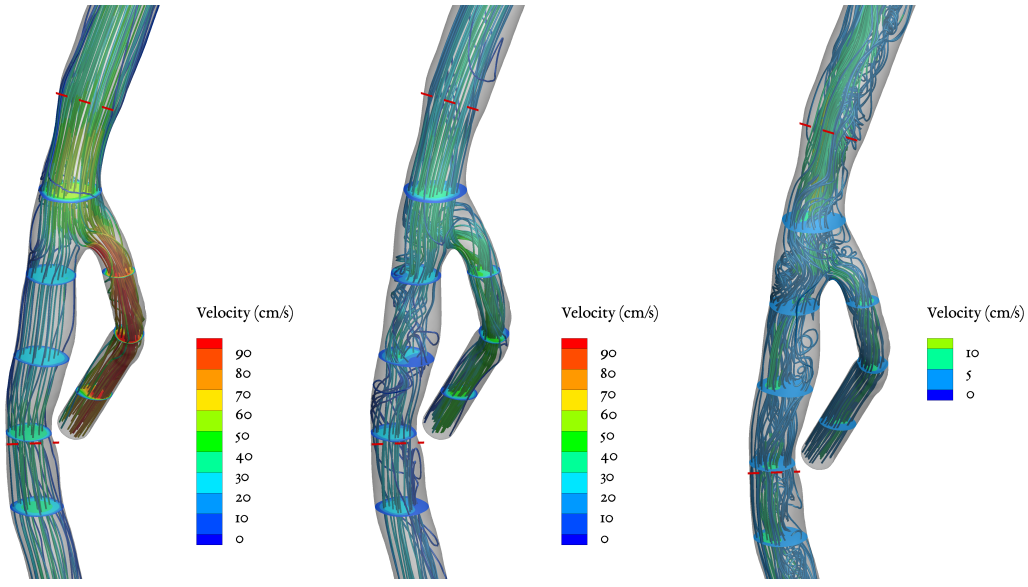

(a) Peak systole **(b)** Systolic deceleration **(c)** Diastole

Figure 5.4: Case 1 - streamlines and velocity contours for the three phases of the cardiac cycle marked in figure 5.3. The color map for diastole encompasses a smaller scale compared to systole.

Table 5.1: Case 1 - simulation parameters

	AFC	AFS	AFP
Diameter (mm)	7	5	5
Mean (max) inlet Re	101 (250)		
Inlet Womersley number	5.7		
R_{prox} ($kg\,mm^{-4}\,s^{-1}$)		1.45×10^{-4}	2.39×10^{-5}
C ($mm^2\,s^2\,kg^{-1}$)		266	296
R_{dist} ($kg\,mm^{-4}\,s^{-1}$)		4.83×10^{-3}	4.7×10^{-3}
Hematocrit	0.3		
Kinematic viscosity ($mm^2\,s^{-1}$)	2.77		

calized region of minimal WSS is situated at the site where the previous near-edge stenosis developed (Fig 5.1a). In contrast, CTA and Duplex showed a healthy bifurcation and SFA on contemporary anatomic and hemodynamic grounds, with good tibial artery run-off. Half a year later, however, the SFA was occluded. CFD results highlight a focal region of very low wall shear stress and disturbed flow near the inflow of the Viabahn stent that persists throughout a large part of the cardiac cycle. Importantly then, CFD results may be able to predict stent thrombolization in cases where traditional CTA and duplex assessment fail to do so. Performing CFD simulations in a wider cohort of Viabahn patients is therefore warranted, to investigate if CFD-visualized regions of low wall shear stress can differentiate between cases of good stent patency and stent thrombolization.

If the focal area of local wall shear stress does indeed correlate with adverse stent patency, the next challenge is to design a treatment approach, preferably endovascular, that either (1) modifies flow to reduce its separation at the inflow region of the stent or (2) covers the vessel wall at the areas where it is exposed to minimal shear stress. The complicated physics of flow separation in patient-specific anatomies renders intuitive assessment of how a treatment changes flow dynamics likely to fail. Instead, endovascular or surgical treatment may be virtually simulated with computer-aided design software after which the modified geometry can be simulated with CFD to see if regions of low WSS have been alleviated.[91] The second case demonstrates this strategy for a relatively simple treatment: inflation of upstream stenotic lesions with percutaneous balloon angioplasty.

5.4 Case 2 - upstream common femoral artery stenosis

A 78 year-old male, with a history of coronary bypass grafting, diabetes and disabling intermittent claudication not responding to exercise treatment, was diagnosed with a bilateral total occlusion of

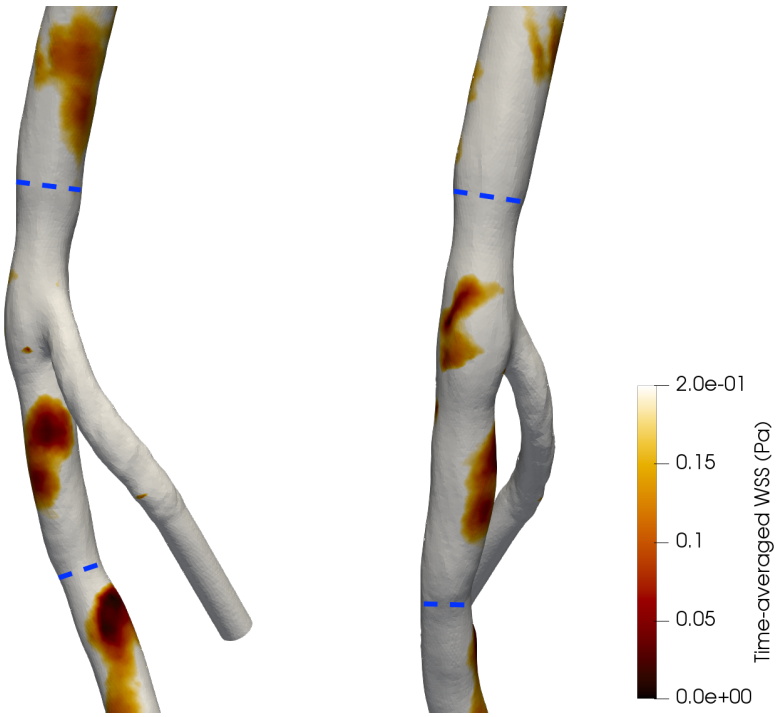

Figure 5.5: Case 1 - mean wall shear stress over one cardiac cycle. Blue lines depict the Viabahn borders.

the SFA (ankle-brachial index right 0.76 and left 0.64). The left side was treated first in 2015, with a combined thrombo-endarterectomy of the common femoral artery and recanalization of the SFA with a heparin-bonded Viabahn stentgraft with PIER. Two Viabahn stentgrafts were deployed (distal 25 x 0.6 cm and proximal 15 x 0.7 cm), proximally landing at the origin of the SFA. Completion angiography demonstrated three patent tibial arteries after which the arteriotomy was closed with a synthetic patch.

Regular follow-up with duplex ultrasound demonstrated a 50% stenosis of the common femoral artery, which was treated with percutaneous transluminal balloon angioplasty (PTA) to improve inflow of the Viabahn. No recurrent stenosis was observed on Duplex at three-month follow-up, but on 6-month follow-up a 50% restenosis of the left AFC resurfaced, albeit with a normal left ankle-brachial index of 0.99 . At the same time, exercise treatment for the right leg had proved inadequate and common femoral thrombo-endarterectomy and SFA recanalization with a Viabahn were planned for the right side. Although no clear-cut indication was present for treating the recurrent stenosis of the left CFA, the right-sided thrombo-endarterectomy provided a means to simultaneously approach the left CFA through endovascular cross-over of the aortic bifurcation and perform angioplasty with a drug-eluting balloon (DEB). Half a year later, regular follow-up showed an occluded Viabahn at the right side, an in-stent stenosis of the left Viabahn (at a location in the distal

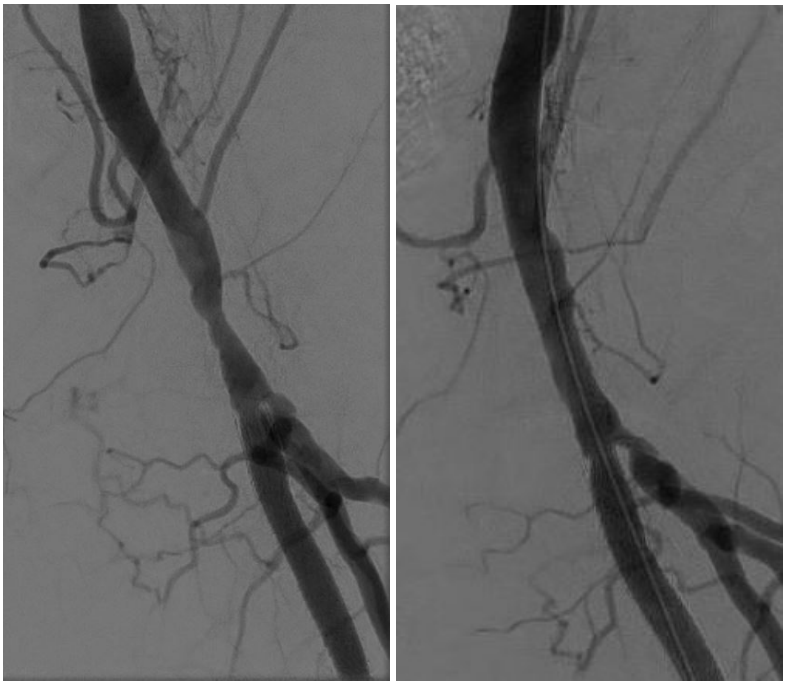

(a) DSA before DEB **(b)** DSA after DEB

Figure 5.6: Case 2 - PTA treatment of the CFA stenosis upstream of the Viabahn stentgraft in the SFA.

femoral artery, far downstream from the segmented domain) and a proximal stenosis in the profunda femoral artery, all without significant symptoms. The in-stent stenosis was treated with PTA 6 months before this report was written, with good peri-procedural outflow, and the left SFA has shown no signs of occlusion at the time of writing.

Flow simulations In the present case, the arterial access provided during endarterectomy of the right common femoral artery facilitated the decision to perform PTA of the hemodynamically insignificant stenosis upstream of the Viabahn. No additional arterial puncture was needed, reducing risk of treatment, and therefore the expected benefit, better durability of the downstream Viabahn stentgraft, outweighed the risk of treatment. If, however, arterial access had not been available, the decision to treat would have been less evident. To explore how CFD can be used in predicting treatment effect on local flow, the flow dynamics before and after DEB angioplasty were simulated.

The anatomic effects of balloon angioplasty were virtually replicated with vmtkLab. Although most likely not developed with that intention, its mathematical shape evolution procedure could be leveraged to mimick the growth of a cylindrical shape (the PTA balloon) inside the stenosed vessel (Fig. 5.7b). This was accomplished by strongly reducing the image gradient-based advection force

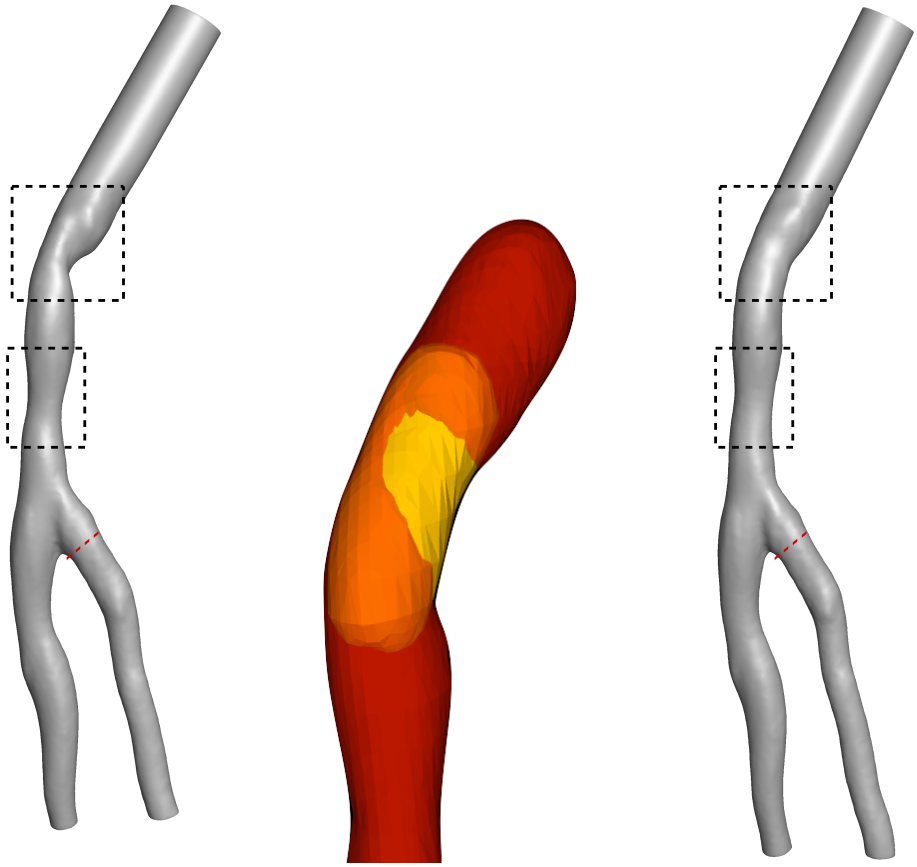

(a) CTA-based geometry before PTA **(b)** Virtual PTA with vmtkLab **(c)** Simulated geometry after PTA

Figure 5.7: Case 2 - oblique lateral view of the geometry before and after virtual PTA treatment. Flow extensions were appended to the CFA inlet to reasonably impose a Womersley profile. The two lesions shown by black markers were expanded with virtual balloon angioplasty, the red lines point to the approximate proximal edge of the implanted Viabahn stentgraft. The middle figure illustrates the virtual ballooning angioplasty for the proximal eccentric stenosis.

Table 5.2: Case 2 - simulation parameters

	AFC	AFS	AFP
Diameter (mm)	9	6.5	6.5
Mean (max) inlet Re	135 (1015)		
Inlet Womersley number	7.2		
R_{prox} ($kg\,mm^{-4}\,s^{-1}$)		3.82×10^{-5}	2.39×10^{-5}
C ($mm^2\,s^2\,kg^{-1}$)		954	1360
R_{dist} ($kg\,mm^{-4}\,s^{-1}$)		2.6×10^{-3}	1.89×10^{-3}
Hematocrit	0.36		
Kinematic viscosity ($mm^2\,s^{-1}$)	2.9		

(the third weight in Eq. 2.1) and tuning the inflation and curvature weights to produce a realistic result, e.g. one where the inflated lumen was smooth in shape and only slightly diminished in profile compared to neighbouring healthy regions. Full anatomic data (CTA) was only available before the DEB procedure, so the accuracy of the PTA simulation could not be compared against the actual anatomic result of the DEB procedure.

Next, both the pre-DEB and post-DEB geometries were simulated with the same boundary conditions derived from duplex data measured two weeks before the CTA-scan. Model and simulation characteristics are presented in table 5.2. Duplex data showed biphasic flow signals in the CFA and PFA, contrasted by triphasic flow in the SFA (Fig. 5.8). In the simulations the CFA biphasic profile was imposed as inlet and the SFA triphasic profile was therefore reduced to a biphasic one. The PFA duplex signal had a low signal-to-noise ratio and the oscillation seen in peak velocity was considered as noise and therefore not modeled in the boundary conditions for the simulations. Since the mean flowrate in the SFA and PFA combined was about 15% lower than CFA inflow, mean outflow in the SFA and PFA was increased by 15% in the simulations. Flow rate division over the outlets was almost equal in simulations of pre-treatment and post-treatment geometry, reflecting the dominance of the boundary conditions over the 3D-geometry in driving the flow division.

Figure 5.9 shows the CFD results in terms of velocity and cycle-averaged wall shear stress. In the pre-treatment case with two mild stenoses, flow enters the bifurcation during peak systole with high velocities (roughly 300 cm/s), causing flow to split distally in the bifurcation and enter the SFA (on the right side in this lateral view) with high velocities. In the post-treatment geometry, the flow dividing region is more gradual and more upstream relative to the bifurcation. In both cases, areas of flow recirculation develop at the outer walls of the bifurcation, which continue to grow during deceleration. The recirculating flow in the SFA is most prominent and relevant, as it is in close prox-

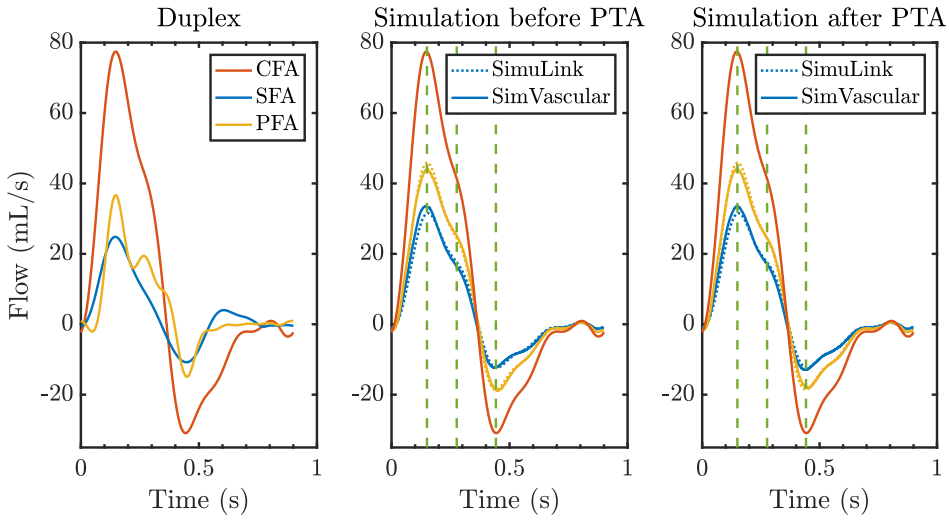

Figure 5.8: Case 2 - boundary conditions measured on duplex and used for the two simulations. The green dotted lines mark the time instances for which streamlines are plotted in figure 5.9.

imity to the Viabahn's proximal edge (red dotted line). During deceleration in the pre-treatment geometry, flow in the SFA recirculation zone shows marked helical upwards patterns with relatively high velocities. For the post-treatment case, flow in the SFA recirculation area is less structured with lower near-wall velocities. During backflow, blood flow is seen to reverse at the outer walls of the bifurcation and shows a well-structured profile during peak backflow, except for some recirculation downstream from the CFA stenosis in the untreated model.

Contours of cycle-averaged wall shear stress show relatively high values (>0.4 Pa), with a few isolated spots with minimum WSS stress on the order of 0.1-0.2 Pa. Surprisingly, these areas of somewhat low WSS are more prevalent in the post-treatment geometry. Moreover, at the onset of the SFA a region of low WSS newly appears in the simulated post-treatment case that was not present before treatment. In the non-treated model with a minor stenosis, the strong spiraling flow with relatively high velocity elevates WSS in this region and the slight stenosis may therefore possibly protect the inflow region of the Viabahn stentgraft from areas of low WSS. If assuming WSS below 0.4 Pa is adverse, a cut-off value based on ex-vivo studies and often used in literature with the lack of a clinical measure, [92,16] the Viabahn endograft may be considered to be at risk. However, this WSS cut-off is based on correlations between wall-shear stress and intimal thickness or other indicators of atherosclerosis, not with risk on thrombolization, which may only become significant at lower cut-off values than those used for atherosclerosis.

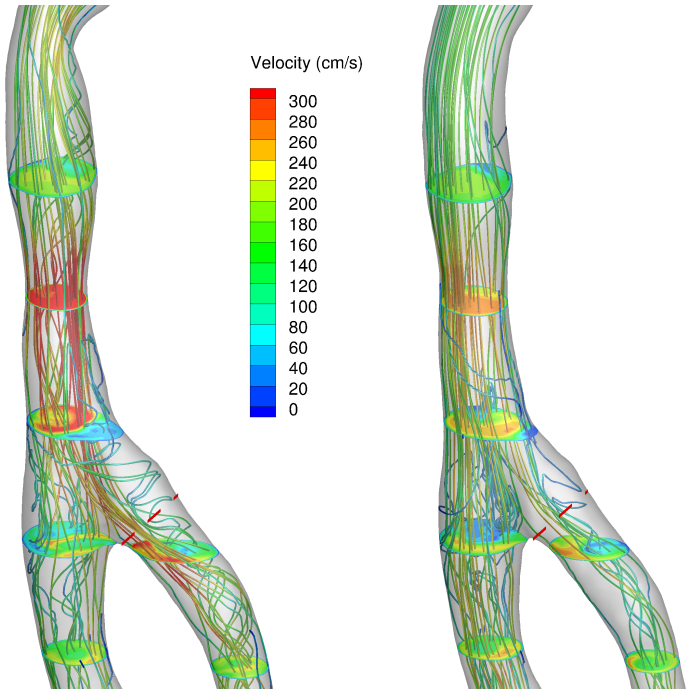

(a) Peak systole

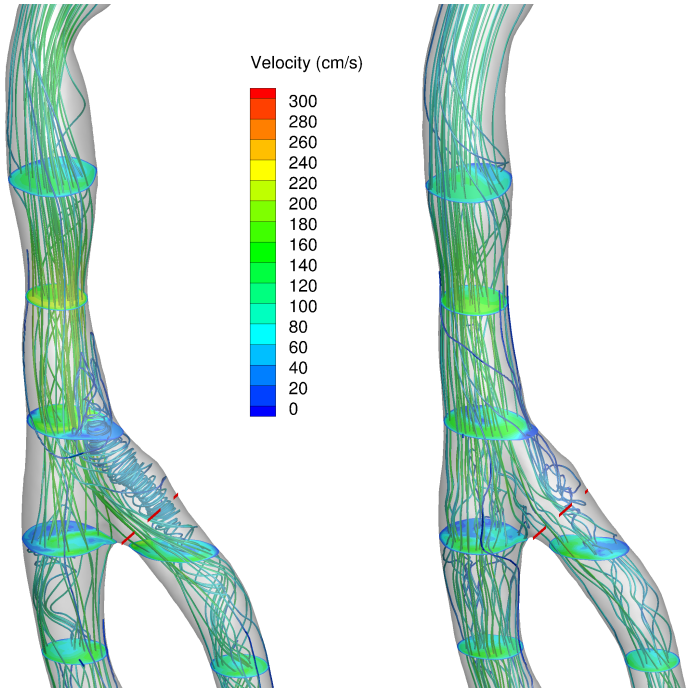

(b) Systolic deceleration

Figure 5.9: Case 2 - Velocity streamlines, contours and wall shear stress. Left: before PTA, right: after PTA. The three phases shown of the cardiac cycle are marked in figure 5.8.

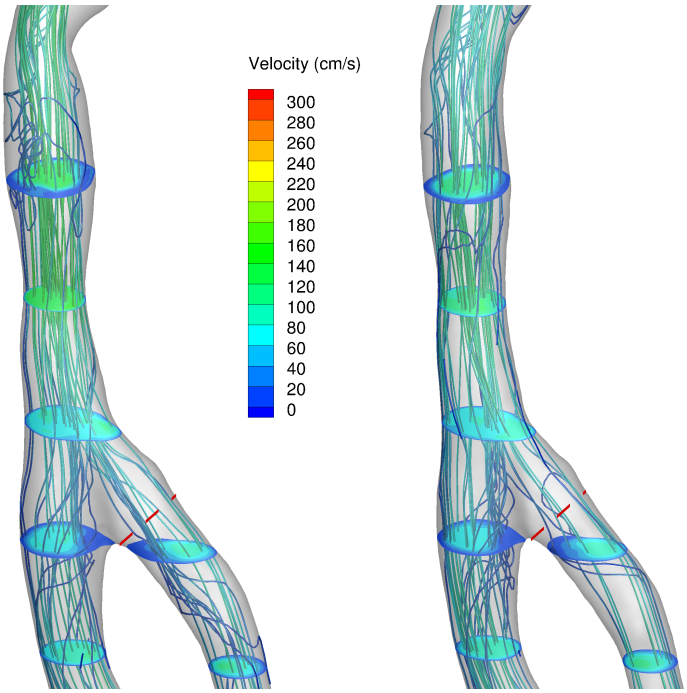

(c) Peak backflow

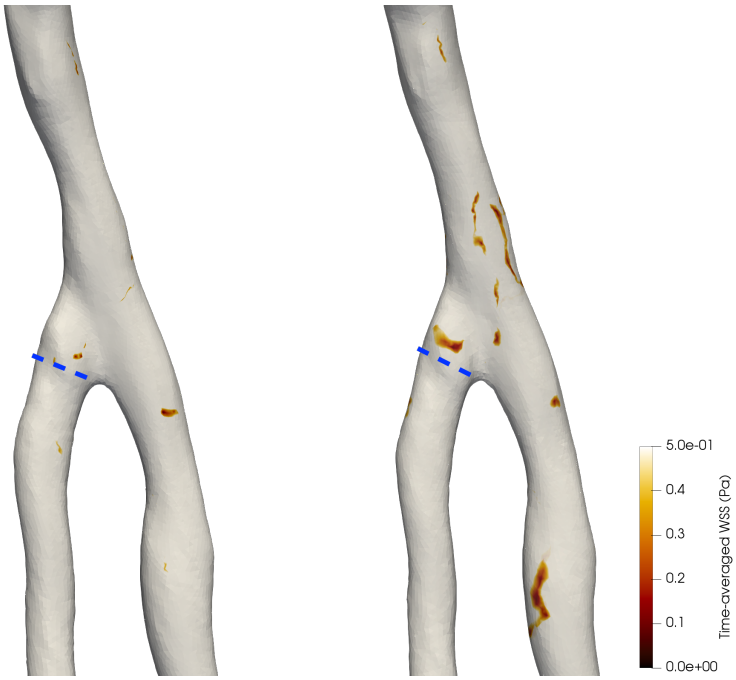

(d) Wall shear stress

Figure 5.9: Case 2 - Velocity streamlines, contours and wall shear stress. Left: before PTA, right: after PTA. The three phases shown of the cardiac cycle are marked in figure 5.8.

5.5 Discussion

The hemodynamic significance of blood's velocity profile in the development of proximal edge stenosis and thrombolization of the Viabahn stentgraft is unknown, but is likely to play an important role. Simulated velocity profiles in the two femoral bifurcation geometries indeed show prominent regions of flow separation in the proximal SFA that, if sustained over the cardiac cycle, can lead to localized regions of very low wall shear stress. In the first case, this region was localized in a geometry unobstructed by stenoses with patent tibial vessels, and no other abnormalities were reported on radiologic or duplex examination. Flow simulations by CFD, in contrast, show areas of significantly low wall shear stress (< 0.05 Pa). The Viabahn stentgraft in the second case was considered at risk due to subcritical upstream stenosis in the common femoral artery, which was treated to reduce the risk on stent thrombolization. Here CFD analysis shows tiny spots of medium-low WSS (0.3-0.4 Pa) before PTA treatment. A wall-shear stress classification by CFD thus predicts that the Viabahn in the first case has most thrombotic risk, contradicting contemporary clinical assessment, which would conclude that the Viabahn stentgraft in the second case was more at risk due to the upstream stenosis. Six months later, however, occlusion of the stentgraft occurred in the first case, in line with the risk stratification put forward by CFD. Whether the Viabahn in the second case would still be patent if PTA had not been performed, as simulated wall shear stress profiles suggested no major risk, is logically unknown. For an infrainguinal bypass, a previous study showed that stenoses with a <50% diameter reduction in a location proximal to the bypass did not effect bypass graft patency if left untreated.[93] For the Viabahn stentgraft, the treatment of an asymptomatic proximal inflow stenosis in the CFA may similarly be unnecessary in a majority of cases.

In deciding when to treat or not, virtual treatment of a patient's anatomy followed by CFD analyses could provide valuable information on the treatment effect's on local flow dynamics. If both the treatment procedure can be accurately simulated and the CFD boundary conditions after treatment predicted with reasonable accuracy, this empowers individualized predictions of whether treatment improves local flow dynamics. Individualized benefits of an intervention can then be balanced against procedural risks to reach more informed and personalized treatment decisions. Also, procedural technicalities, such as the length of the vessel to treat with covered endograft, can be optimized such that the extent of endothelium exposed to low wall shear stress conditions is minimal after treatment. In the following, the limitations of the present approach to simulating balloon angioplasty will be discussed, as well as more sophisticated techniques for simulating complex treatments like stent deployment and modeling a treatment's potential effect on flow distribution throughout the major arteries.

For simulating treatment procedures, geometric shape inflation of a cylindrical shape was used to model balloon angioplasty. The vessel diameter after ballooning was kept fractionally smaller than

its healthy surroundings to secure a smooth transition. This may not have been unrealistic, as 1 out of 3 vessels shrink by over 5% due to inwards vascular remodeling after PTA.[94] Obviously, the PTA simulation needs validation based on 3D imaging scans made after PTA. Virtual surgery is an especially relevant complement to CFD simulations, and its current capabilities for more complicated procedures like stent placement will be discussed in chapter 6. Theoretically, virtual simulation of deployment of a Viabahn stentgraft is possible. The relevance of doing so for the edge stenosis and in-stent thrombolization addressed here is arguably minor, as, with a thickness of about 150 μm, the stent is not expected to impact global flow behavior through mechanical interactions. Its impact on post-operative anatomy is additionally expected to be minor as the stentgraft conforms to the original anatomy by virtue of its flexibility and it usually features a circular lumen throughout, except at places of severe calcification.

The two case studies presented here demonstrate the feasibility of using CFD to estimate the distribution of wall shear stress in patient-customized models of the femoral artery. More specifically, the models used were individualized for patient geometry, duplex centerline velocity measurements in the major femoral arteries and viscosity. Patient-specific blood pressure was also modeled, but does not influence the velocity profiles in the absence of wall motion. Wall motion, blood's non-linear viscosity and possible non-periodicity of pressure and flow rate[44] were not modeled. Although these are likely to impact the magnitude of wall shear stress profiles by 10-20%, they typically do not impact the qualitative distribution of wall shear stress patterns (discussed in chapter 2) and are therefore not expected to change the clinical implication of the observations made in these case studies.

A more important limitation is the derivation of flow rates in the AFC, AFP and AFS that was based on retrospective duplex velocity data and vessel diameter measured on CTA. On duplex reports, a rough description is given of the measured location (e.g. distal SFA), but it is unclear which precise location was used to store the velocity profile. It was therefore difficult to tell accurately determine the corresponding diameter on CTA and whether this location was in close proximity to upstream stenoses or substantial curvature, which can cause deviations from the assumed Womersley profile used to compute volumetric flow rates. Especially for case 2, the flow rate reconstructed in the CFA may have been overestimated due to the two mild stenoses present in the CFA. These difficulties in reconstructing the boundary conditions reflect general limitations of performing CFD simulations on retrospective data. A logical next step, also considering the potentially meaningful clinical implications of CFD simulations in the two case studies, is to set up a prospective CFD study for a cohort treated with a covered endograft in the SFA. For such a study, peri-operative imaging with rotational angiography or post-operative imaging with CTA-scans must preferably be included in addition to routine follow-up to allow accurate geometry reconstruction. Then, the incidence of edge stenosis or stent thrombolization in a follow-up period of 1-2 years can be correlated with a

CFD-based measure of wall shear stress, in order to assess the predictive ability of CFD for stentgraft complications.

6

Future directions: CFD in occlusive and aneurysmatic disease

Next to the clinical applicability of CFD in the quantification of serial stenotic lesions in the femoropopliteal arteries and in the prediction and perhaps prevention of Viabahn thrombolization, numerous other topics of vascular surgery may be well served by CFD. Its capability in non-invasively computing pressure drops and visualizing areas of adverse flow patterns is a powerful addition to imaging techniques. Besides, its versatility in accepting virtually modified geometries or boundary conditions carries promising prospects for a synergy with the simulation of vascular interventions. Both technical advancement in CFD methodology as well as clinical needs will dictate the areas where CFD may add value to healthcare. This chapter combines clinical and technical perspectives to identify topics in vascular surgery that have promising potential for the adoption of CFD in its clinical workflow. Depending on the topic, the technological readiness, the prospects for cohort generation or other aspects are shortly discussed. The section first treats a more technical review of virtual treatment simulation with CFD, after which research opportunities in occlusive disease, surgical anastomotic techniques and aneurysmatic disease are presented.

6.1 Virtual surgery

Besides computational modeling of blood flow, the mechanical simulation of how complex endovascular devices conform to a patient's unique anatomy is finding its adoption in clinical workflows,[95] most notably for the simulation of transcatheter aortic valve implantation.[96] Although structural

and fluid mechanical simulations are non-trivial techniques in their own right to become acquainted with, developments have been ongoing for modeling mechanical simulation of device deployment with subsequent CFD simulations for hemodynamical evaluation of device performance. This is exemplified by a recent study showing feasibility of CFD's prediction of regurgitation after simulated TAVI deployment in 60 patient cases.[97]

In vascular surgery, augmenting CFD with mechanical simulation of peripheral stent and stentgraft deployment has potential to offer substantial advancements in the prediction of overall treatment success, both technically and hemodynamically. Compared to TAVI deployment, simulating peripheral stent deployment is arguably less complex, and numerous examples have been reported[55,98,99,100] for bare metal stents, typically employing commercial structural solvers. An implementational challenge is that well-tuned material models need to be customized to a stent's individual mechanical characteristics by time-intensive mechanical testing. For covered stentgrafts, the mechanical linking of struts through the graft material, as well as graft contact with the wall become exceedingly difficult to simulate, although possible, as has been demonstrated for a modular Talent endograft[101] as well as more recently in select case studies of tortuous aneurysms.[102]

If treatment procedures can be successfully simulated, a challenge for subsequent CFD simulations is that treatment typically alters flow distributions throughout the body. If significant, these changes must be reflected in the flow boundary conditions, which can be an involving task. If the resistance of the 3D-hemodynamical domain is substantially altered, for instance after revascularization of an occluded vessel, it is probably hard to predict how peripheral resistance in the distal microcirculation individually responds in the treated and ipsilateral leg. In most cases a patient's flow rate before the time of occlusion will be available and assuming the flow rate after treatment will restore to the same level as before occlusion may be an adequate approximation.

In more complex cases involving treatment of multiple branches, a closed-loop model of the lower body arterial tree can be applied to model the physiologic drivers of time-dependent flow rate distribution to both legs. SimVascular has built-in coupling alghoritms for embedding the 3D arterial domain of interest into a closed-loop 0D-network of resistive, capacative and inductive components.[66] Flow rate at the inlet of the 3D-model is then no longer prescribed as a Dirichlet boundary, but extracted from a coupling with the 0D closed-loop model of the lower body circulation. The inlet is set as a combined Dirichlet-Neumann boundary that prescribes flow and pressure passed on by the upstream 0D-network, similar to the treatment of outlet boundaries. Closed-loop models have the downside of being labour-intensive by their need for refined and case-dependent strategies for tuning model parameters.

6.2 Occlusive disease

As a generalization of the application towards serial stenoses discussed in chapter 4, non-invasive determination of translesional pressure drops have promising applications at other sites of arterial stenoses in which current diagnostic modalities have limited predictive power. Two especially relevant clinical challenges are renal artery stenosis and equivocal iliac artery stenosis.

Renal artery stenosis is a frequent cause of uncontrolled hypertension and progressive renal insufficiency, with a prevalence estimated at 4.3% in autopsy studies.[103] Treatment of renal artery stenosis by percutaneous balloon angioplasty with stent placement can improve hypertension control and renal function and thereby significantly reduce a patient's risk on future cardiovascular events.[104] A diagnosis cannot be reliably made on clinical symptoms and current diagnostic procedures are not well able to predict whom benefits from treatment, with modern MRI-derived[105] and duplex diagnostics[106] demonstrating only 50% specificity at reasonable sensitivity. In contrast, post-hoc analyses of invasive translesional pressure measurements in the renal artery show specificity of 80% at similar sensitivity levels.[107] CFD has potential to accurately assess the pressure gradient, also under hyperemia, and therefore become a reliable non-invasive predictor of treatment success for renal artery stenosis. The accuracy of the CFD predicted pressure drops can be validated in retrospective or prospective cohorts where translesional pressure drop has been measured invasively.

For iliac artery stenosis, stenoses with a diameter reduction of 50-75% on angiography show a wide variety of pressure drops, ranging from 5 - 50 mmHg at rest flow.[108] Although accurate diagnosis by invasive pressure measurements is recommended, preferably in a hyperemic state through administration of a vasodilating drug, this is not routinely performed for several practical reasons.[83] With the advancement of thin-wire pressure catheters, clinical interest in translesional pressure measurements is growing and hyperemic measures like fractional flow reserve (the pressure ratio of the downstream and upstream mean pressure in hyperemic conditions) have been reported to be feasible in iliac stenoses.[109] Meanwhile, the validity of two-dimensional CFD, which assumes axisymmetric flow, in predicting pressure gradients in iliac artery stenoses on the basis of rotational angiograhy has recently been demonstrated. Obvious advantages of a 2D-method are its ease of implementation and short computational times, yet it is unable to reproduce secondary flows that can become significant in highly eccentric stenoses or serial stenoses, as was shown in chapter 4. The 2D-solver that was validated against invasive systolic pressure drop during hyperemia used a steady flow assumption, for which the SimVascular 3D-solver is expected to achieve a computational time in the order of minutes on a well-optimized cluster. Extracting geometrical data from a CTA-scan made before a potential intervention is likely preferable, as invasive angiography can then be prevented if the equivocal stenosis is marked non-significant with CFD.

From a computational standpoint, more complex clinical challenges in occlusive disease are

formed by plaque vulnerability in carotid artery stenosis and flow around stentgrafts that are not apposed to the wall. Carotid artery stenosis is typically not flow-limiting owing to the extensive collateral circulation in the cerebral vasculature. Instead, its main risk is atheroma rupture in high-grade stenosis, after which parts of the vessel wall or small thrombi formed on its exposed surface can be shed with the flow and induce a stroke through obstruction of a downstream cerebral vessel.[110] Pressure and shearing forces by the fluid contribute to stress forces within plaques and areas of high wall shear stress have been hypothesized to induce atheroma rupture. Although the imaging requirements and relatively low incidence of stroke make correlations hard to establish, retrospective studies seem to reach consensus that structural plaque stress computed by partitioned fluid-structure simulations is a more sensitive predictor than high wall shear stress alone.[111,110,112] Therefore, until comprehensive mechanical solvers able to simulate stress distribution within the wall become part of user-friendly blood flow simulation packages, this clinical problem is probably best addressed by dedicated biomechanical research labs.

Simulating the flow of blood around stents is another challenging computational exercise, but particularly relevant for explaining the failure of stents used in complex branching anatomies, such as the aorto-iliac bifurcation. Kissing stents inserted from the iliac arteries and simultaneously expanded with balloon angioplasty are often used for treating occlusive iliac artery disease. However, through the inflation of two cylindrical shapes in an encompassing cylinder a mismatch area outside of the two stents is inevitably created that can induce stagnant flow, either in the apex of the bifurcation for bare metal stents or at the inflow region for covered kissing stents.[113] The presence and extent of these recirculation zones in vivo will depend in complex ways on the stent configuration used in relation to the patient's anatomy, which CFD can potentially elucidate. Some technical challenges have to be addressed in order to do so. The presence of stent material in what is normally flow lumen may render conventional segmentation and meshing techniques unsuccessful and thus require a modified approach. In addition, the small scales of stent and graft material necessitates small mesh sizes at their boundary, increasing computational cost of the simulations. Development of an efficient approach is relevant if strong associations between recirculation zones and stent failure are found, as likely only computational techniques can pre-operatively predict if the combination of stent characteristics and patient anatomy will predispose to significant recirculation zones.

6.3 Surgical anastomosis techniques

Anastomoses are used in vascular surgery to create new connections between arteries and veins. An artery and vein in the arm can be anastomosed intentionally to create an arteriovenous fistula used for hemodialysis access. Other anastomoses typically involve the use of a venous or synthetic graft to bypass an occluded artery by connecting the graft to the healthy artery proximal and distal to

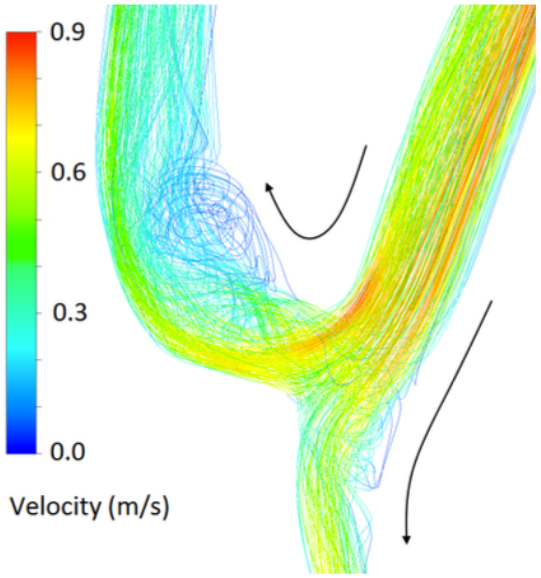

Figure 6.1: Flow separation in an arteriovenous fistula. Reproduced from Guess et al. [73]

the occlusion. A common complication is the onset of stenosis at the anastomotic sites, with subsequent thrombolization if left untreated or undetected. For autogenous infrainguinal vein grafts, intermediate lesions were seen to develop in 20% of newly created bypasses at a mean of 4 months after implantation,[114] but occlusion can be reasonably well prevented with appropriate follow-up and PTA if necessary, providing assisted primary patency of 85% at 2 years.[115] For arteriovenous shunts, juxta-anastomotic stenosis has been reported in approximately 38% of newly created shunts and resulted in non-maturation for 50% of the forearm fistulas, compared to roughly 10% failure in those without stenosis.[116] In addition, the fistulas with stenoses that did mature were characterized by more frequent post-operative interventions.

Considering the high incidence of restenosis and its severe complications, it would be particularly relevant to visualize flow patterns at the arteriovenous anastomosis in patient cohorts. The high prevalence of juxta-anastomic stenosis in arteriovenous fistula is likely in part due to the significant curvature that blood follows when traversing from the artery into the vein, which has in PC-MRI measurements and simulations been seen to induce flow separation from the inner wall.[73,117] Importantly, one of those studies employed both a rigid wall and a partitioned fluid-structure interaction model, in which the wall's mechanical properties were differentiated between the artery and the vein. Differences in predicted wall shear stress of 12% were present between the fluid and FSI model, but the wall shear stress distribution was very similar. The results of both models were compared with in vivo PC-MRI and both the fluid model and FSI model showed excellent agreement with the region of flow separation at the inner anastomotic wall (Fig 6.1).

Therefore, the rigid wall SimVascular solver applied to patient-specific fistula models with the methodology presented in chapter 2 is expected to be a sufficiently accurate modeling approach to predict flow separation and wall shear stress distribution and investigate its relation with juxta-anastomotic stenosis and shunt failure. If needed, the deformable wall SimVascular solver may be used to predict the magnitude of wall shear stress more accurately at roughly twice the computational cost if arterial and venous mechanical properties are considered equal, or a few times more if they are modeled with separate characteristics. For the patient data needed, the most relevant consideration is the acquisition of full 3D imaging data. CT-scans are not routinely made for shunt planning or on follow-up, and may be contra-indicated for patients who still have a functioning kidney, although evidence is sparse for the additive harm of contrast media in end-stage renal disease.[118] Retrospective studies based on CT-scans made for other purposes may be a feasible first step. To obtain imaging data for a potential prospective patient study, MRA may be an alternative modality, although costly in comparison. In both cases, it would be of interest to investigate the effect of anastomosis curvature, vessel diameters, individualized anatomy and flow rate division on the extent of flow separation and possible correlations with restenosis and shunt failure. The acquired insights may be useful in improving anastomosis techniques tailored to individualized anatomic features. A possible extension is the use of CFD in virtual treatment planning, where various sites and technical characteristics of surgically feasible anastomes are simulated to select the one optimal in terms of flow characteristics. An exciting technical advancement for treatment planning is the incorporation of optimization in the modeling pipeline, after which various characteristics of the surgical procedure can be automatically and iteratively optimized to minimize a pre-defined cost function.[91] Likely candidates for the cost-function in case of restenosis include a wall-shear stress derived measure, but major clinical flow studies are deemed necessary before such functions can be reasonably defined.

6.4 Aneurysmatic disease

Research on rupture and growth of abdominal aortic aneurysms has justifiably started from CT-based structural analysis of stress distribution in the aneurysm, and more recently these have been augmented with CFD to augment the calculation of plaque wall stress with blood's mechanical forces[119] in the quest for a diagnostic that adds predictive power to the aneurysm's diameter. Although significant results in small samples have been found, a limited study size and heterogeneity has thus far limited generizability and clinical applicability.[120] In addition, endovascular treatment of abdominal aneurysms now often enables treatment of patients with significant comorbidities and rupture of aneurysms smaller than current diameter cut-offs is not very common,[121] limiting the added value of a new rupture predictor to some extent.

Instead, a focus on the complications of endovascular treatment, which still persist for modern devices, may bear more clinical relevance. The most relevant complications are type I endoleaks from the proximal or distal graft attachment sites. Although the clinical impact is less severe, type II endoleaks also deserve attention due to their frequent incidence. Late type I endoleaks are often associated with progression of aneurysmatic disease at the neck or common iliac artery. For the iliac artery a hemodynamic component of blood's outflow pattern from the stentgraft may relate to the progression of disease, especially if an aneurysmatic iliac artery wider than 2 cm is used as landing zone.[122] Continued growth of the common iliac aneurysm may evolve into a type Ib endoleak, and the growth rate can perhaps be related to and predicted by the way that blood exits the stentgraft into the iliac aneurysm. Although the meshing of the stent may require a customized meshing strategy for CFD computations, retrospective input data for CFD is likely available in substantial quantity owing to the use of both duplex and CTA-scans in EVAR follow-up. The possibly relevant effects of wall-motion on flow may also be investigated with SimVascular's deformable solver.

For type II endoleaks, ambiguity still exists on whether aggressive treatment can save patients from the risks seen for persisting (>6 months) type II endoleaks,[123] or whether a more conservative approach is warranted as most type II endoleaks resolve spontaneously. To which category a type II endoleak belongs may relate to the extent of collateral connections between for instance the IMA and SMA artery. Instead of the proposed 3D-hemodynamic simulations suggested throughout this chapter, here the use of 0D or lumped parameter networks can be an elegant diagnostic solution. Similar to the quantification of collateral flow,[124] a coupled network of resistors and capacitances with values based on CTA-scan diameters can model the extent to which pressure is transmitted through collateral vascularization towards the aneurysm sac. The cases where predicted transmitted pressure exceeds a certain threshold may discriminate persistent endoleaks that warrant treatment from self-resolving endoleaks.

7 Conclusion

This thesis has started with the selection of numerical tools that can cost-effectively simulate the mechanics of three-dimensional, pulsatile blood flow in the femoral artery bifurcation. In a (silico) bench to bedside fashion, a validation study was first performed, followed by flow simulation in idealized stenotic geometries and ending at the intended goal of flow simulation in two patient cases. The findings will be summarized in analogous order.

Full patient-specific computational models of blood flow require the segmentation of the anatomy of interest and info on flow rates in the arteries under investigation. Tools to extract these from CTA and duplex ultrasound were built due to the readily availability of these modalities in patients with femoral artery disease. Peri-procedural rotational angiography was tested with as of yet limited success. The meshing and 3D flowsolver routines from SimVascular were used due to their customized advantages and speed for blood flow simulation.

Triphasic flow was experimentally visualized in a healthy and significantly stenosed model of the femoral bifurcation by particle image velocimetry to validate the numerically predicted results. The results showed good qualitative agreement for most of the cardiac cycle with deviation of the numerical results during bulk flow reversal due to effects of the Womersley inlet boundary. For the stenotic model, the simulations predicted jet growth and breakdown not seen in the experimental results, possibly caused by not resolving the turbulent characteristics on sufficiently small scales. Overall capability of the solver for predicting physiologic velocity fields was demonstrated, with further evaluation needed to assess the influence of the inlet boundary during backflow and on the impact of not fully resolving turbulence in transitional flow.

Subsequently, the combined effect of two subcritical tandem stenoses in close proximity on the

pressure drop was investigated in 40 idealized geometries by mixing three stenotic shapes of 50% area-reduction in various configurations. At steady flow for Reynolds numbers of 1800 (15 mL/s in the femoral artery), representative of CLI patients, non-circular shape was a strong determinant of pressure drop, with a smaller role for eccentricity. Combining two stenoses confirmed that the pressure drop never exceeded the sum of the individual stenoses, but equaled 75-85% of the sum of their respective individual pressure drop. The largest pressure drops were found for increasing inter-stenotic distance and 90-degree rotation angles between eccentric stenoses due to strong secondary flow, but these effects were less strong compared to the non-circular geometry. Results in patients are likely to depend strongly on stenosis size and geometry with no easily predictable outcomes by simple approximations. Non-invasive clinical pressure quantification by CFD of multiple stenoses in CLI patients with a computational model of steady flow is therefore indicated.

The third study addressed CFD's potential value of predicting the common complications of proximal edge stenosis and stent thrombolization after treatment of occlusions in the SFA with the Viabahn covered stentgraft. Retrospective CTA and duplex data in two case studies were used to visualize flow and wall shear stress distribution at the inflow area of the stentgraft. One case demonstrated a focal area of very low wall shear stress (<0.1 Pa) at the stent's inflow area. In contrast, anatomic and functional evaluation demonstrated good patency of the femoral arteries and decent tibial run-off. The stentgraft nonetheless occluded under the use of anti-coagulation within 6 months. The case demonstrated CFD's potential in predicting complications in cases where current imaging equipment fail to do so. To investigate this hypothesis, a prospective study in which patients receive an additional rotational angiography or CTA-scan following the Viabahn procedure is indicated.

With the method developed and partially validated, other clinical topics in vascular surgery for which CFD-simulated flow features can augment diagnosis and treatment start to open up. Especially its use in non-invasively (1) quantifying pressure drops for renal artery and iliac artery stenosis, (2) for improving understanding of arteriovenous shunt failure and (3) for predicting type Ib endoleaks or diagnosing the contribution to aneurysm sac pressure by a type II endoleak show promising clinical applications for which current simulation techniques are already applicable. Cohort studies for these three clinical areas are indicated to elicit CFD's value in vascular surgery.

References

[1] Meijer, W. T., Hoes, A. W., Rutgers, D., Bots, M. L., Hofman, A., & Grobbee, D. E. (1998). Peripheral arterial disease in the elderly: The Rotterdam Study. *Arteriosclerosis, thrombosis, and vascular biology*, 18(2), 185–92.

[2] Criqui, M. H. & Aboyans, V. (2015). Epidemiology of Peripheral Artery Disease. *Circulation Research*, 116, 1509–1526.

[3] Hardman, R. L., Jazaeri, O., Yi, J., Smith, M., & Gupta, R. (2014). Overview of classification systems in peripheral artery disease. *Seminars in Interventional Radiology*, 31(4), 378–388.

[4] Norgren, L., Hiatt, W., Dormandy, J., Nehler, M., Harris, K., Fowkes, F., et al. (2007). Inter-Society Consensus for the Management of Peripheral Arterial Disease (TASC II). *Journal of Vascular Surgery*, 45(1), S5–S67.

[5] Abdulhannan, P., Russell, D. A., & Homer-Vanniasinkam, S. (2012). Peripheral arterial disease: A literature review. *British Medical Bulletin*, 104(1), 21–39.

[6] Olin, J. W., White, C. J., Armstrong, E. J., Kadian-Dodov, D., & Hiatt, W. R. (2016). Peripheral Artery Disease. *Journal of the American College of Cardiology*, 67(11), 1338–1357.

[7] Hiatt, W. R., Armstrong, E. J., Larson, C. J., & Brass, E. P. (2015). Pathogenesis of the Limb Manifestations and Exercise Limitations in Peripheral Artery Disease. *Circulation Research*, 116(9), 1527–1539.

[8] Jaff, M. R., White, C. J., Hiatt, W. R., Fowkes, G. R., Dormandy, J., Razavi, M., Reekers, J., & Norgren, L. (2015). An Update on Methods for Revascularization and Expansion of the TASC Lesion Classification to Include Below-the-Knee Arteries: A Supplement to the Inter-Society Consensus for the Management of Peripheral Arterial Disease (TASC II). *Journal of Endovascular Therapy*, 22(5), 663–677.

[9] Garcia, L. A., Rosenfield, K. R., Metzger, C. D., Zidar, F., Pershad, A., Popma, J. J., Zaugg, M., Jaff, M. R., Lei, L., Liu, Y., Hadley, G. L., & Arch, V. S. (2017). SUPERB final 3-year outcomes using interwoven nitinol biomimetic supera stent. *Catheterization and Cardiovascular Interventions*, 89(7), 1259–1267.

[10] Dake, M. D., Ansel, G. M., Jaff, M. R., Ohki, T., Saxon, R. R., Smouse, H. B., Machan, L. S., Snyder, S. A., O'Leary, E. E., Ragheb, A. O., & Zeller, T. (2016). Durable clinical effectiveness with paclitaxel-eluting stents in the femoropopliteal arteryclinical perspective. *Circulation*, 133(15), 1472–1483.

[11] Saxon, R. R., Chervu, A., Jones, P. A., Bajwa, T. K., Gable, D. R., Soukas, P. A., Begg, R. J., Adams, J. G., Ansel, G. M., Schneider, D. B., Eichler, C. M., & Rush, M. J. (2013). Heparin-bonded, expanded polytetrafluoroethylene-lined stent graft in the treatment of femoropopliteal artery disease: 1-year results of the VIPER (Viabahn Endoprosthesis with Heparin Bioactive Surface in the Treatment of Superficial Femoral Artery Obstru. *Journal of Vascular and Interventional Radiology*, 24(2), 165–173.

[12] Al-Hakim, R., Lee, E. W., Kee, S. T., Seals, K., Varghese, B., Chien, A., Quirk, M., & McWilliams, J. (2017). Hemodynamic analysis of edge stenosis in peripheral artery stent grafts. *Diagnostic and Interventional Imaging*, 98(10), 729–735.

[13] Libby, P., Ridker, P. M., & Hansson, G. K. (2011). Progress and challenges in translating the biology of atherosclerosis. *Nature*, 473(7347), 317–325.

[14] DeBakey, M. E., Lawrie, G. M., & Glaeser, D. H. (1985). Patterns of atherosclerosis and their surgical significance. *Ann Surg*, 201(2), 115–131.

[15] Ku, D. N. & Giddens, D. P. (1983). Pulsatile flow in a model carotid bifurcation. *Arterioscler Thromb Vasc Biol*, 3, 31–39.

[16] Chiu, J.-J. & Chien, S. (2014). Effects of disturbed flow on vascular endothelium: Pathophysiological Basis and Clinical Perspectives. *Physiologic Reviews*, 91(1).

[17] Frangos, S. G., Gahtan, V., & Bauer, S. (1999). Localization of Atherosclerosis. *Arch Surg*, 134, 1142–1149.

[18] Himburg, H. A., Grzybowski, D. M., Hazel, A. L., LaMack, J. A., Li, X. M., & Friedman, M. H. (2004). Spatial comparison between wall shear stress measures and porcine arterial endothelial permeability. *Am J Physiol Heart Circ Physiol*, 286(5), H1916–22.

[19] Glagov, S., Zarins, C., Giddens, D. P., & Ku, D. N. (1988). Hemodynamics and atherosclerosis. Insights and perspectives gained from studies of human arteries. *Archives of Pathology and Laboratory Medicine*, 112(10), 1018–1031.

[20] Gimbrone, M. A. & García-Cardeña, G. (2013). Vascular endothelium, hemodynamics, and the pathobiology of atherosclerosis. *Cardiovascular Pathology*, 22(1), 9–15.

[21] Peiffer, V., Sherwin, S. J., & Weinberg, P. D. (2013). Computation in the rabbit aorta of a new metric - the transverse wall shear stress - to quantify the multidirectional character of disturbed blood flow. *Journal of Biomechanics*, 46(15), 2651–2658.

[22] Holenstein, R. & Ku, D. N. (1988). Reverse flow in the major infrarenal vessels–a capacitive phenomenon. *Biorheology*, 25(6), 835–42.

[23] Blair, J., Glagov, S., & Zarins, C. K. (1990). Mechanism of superficial femoral artery adductor canal stenosis. *Surgical forum*, 41, 359–360.

[24] Chi, J., Chiu, B., Cao, Y., Liu, X., Wang, J., Balu, N., Yuan, C., & Xu, J. (2013). Assessment of femoral artery atherosclerosis at the adductor canal using 3D black-blood MRI. *Clinical Radiology*, 68(4), 213–221.

[25] Wood, N. B., Zhao, S. Z., Zambanini, A., Jackson, M., Gedroyc, W., Thom, S. A., Hughes, A. D., & Xu, X. Y. (2006). Curvature and tortuosity of the superficial femoral artery: a possible risk factor for peripheral arterial disease. *Journal of Applied Physiology*, (pp. 1412–1418).

[26] Ku, D. N. (1997). Blood flow in arteries. *Annual Review of Fluid Mechanics*, 29(1), 399–434.

[27] Eckhardt, B., Schneider, T. M., Hof, B., & Westerweel, J. (2007). Turbulence Transition in Pipe Flow. *Annual Review of Fluid Mechanics*, 39(1), 447–468.

[28] Varghese, S. S., Frankel, S. H., & Fischer, P. F. (2007). Direct numerical simulation of stenotic flows, Part 2: Pulsatile flow. *Journal of Fluid Mechanics*, 582, 281.

[29] Sabbah, H. N. & Stein, P. D. (1976). Turbulent Blood Flow in Humans. *Circulation Research*, 38(6), 513–525.

[30] Rosenfeld, M. (1995). A numerical study of pulsating flow behind a constriction. *Journal of Fluid Mechanics*, 301(-1), 203.

[31] Sheu, T. W. & Hsu, M. C. (2009). Finite-element simulation of incompressible viscous flows in moving meshes. *Numerical Heat Transfer, Part B: Fundamentals*, 56(1), 38–57.

[32] Lyne, W. H. (1971). Unsteady viscous flow in a curved pipe. *Journal of Fluid Mechanics*, 45(01), 13.

[33] Berger, S. A. & Jou, L.-d. (2000). Flows in Stenotic Vessels. *Annual Review of Fluid Mechanics*, 32, 347–382.

[34] Morris, P. D., Narracott, A., von Tengg-Kobligk, H., Silva Soto, D. A., Hsiao, S., Lungu, A., Evans, P., Bressloff, N. W., Lawford, P. V., Hose, D. R., & Gunn, J. P. (2016). Computational fluid dynamics modelling in cardiovascular medicine. *Heart*, 102(1), 18–28.

[35] Taylor, C. A., Fonte, T. A., & Min, J. K. (2013). Computational fluid dynamics applied to cardiac computed tomography for noninvasive quantification of fractional flow reserve: Scientific basis. *Journal of the American College of Cardiology*, 61(22), 2233–2241.

[36] Hirsch, C. (2007). *Numerical Computation of Internal and External Flows*. Chichester: John Wiley and Sons, 2nd edition.

[37] Zienkiewicz, O., Taylor, R., & Nithiarasu, P. (2014). *The Finite Element Method for Fluid Dynamics*. Elsevier Academic Press, 6th edition.

[38] Versteeg, H. K. & Malalaserkera, W. (2007). *An Introduction to Computational Fluid Dynamics*. Pearson Education Limited, 2nd edition.

[39] Antiga, L., Piccinelli, M., Botti, L., Ene-Iordache, B., Remuzzi, A., & Steinman, D. A. (2008). An image-based modeling framework for patient-specific computational hemodynamics. *Medical and Biological Engineering and Computing*, 46(11), 1097–1112.

[40] De Santis, G., Mortier, P., De Beule, M., Segers, P., Verdonck, P., & Verhegghe, B. (2010). Patient-specific Computational Fluid Dynamics: Structured mesh generation from coronary angiography. *Medical and Biological Engineering and Computing*, 48(4), 371–380.

[41] Lesage, D., Angelini, E. D., Bloch, I., & Funka-Lea, G. (2009). A review of 3D vessel lumen segmentation techniques: Models, features and extraction schemes. *Medical Image Analysis*, 13(6), 819–845.

[42] Updegrove, A., Wilson, N. M., Merkow, J., Lan, H., Marsden, A. L., & Shadden, S. C. (2017). SimVascular: An Open Source Pipeline for Cardiovascular Simulation. *Annals of Biomedical Engineering*, 45(3), 525–541.

[43] Campbell, I. C., Ries, J., Dhawan, S. C., Quyyumi, A. A., Taylor, W. R., & Oshinski, J. N. (2012). Effect of Inlet Velocity Profiles on Patient-Specific Computational Fluid Dynamics Simulations of the Carotid Bifurcation. *Journal of Biomechanical Engineering*, 134(5).

[44] Vignon-Clementel, I. E., Figueroa, C. A., Jansen, K. E., & Taylor, C. A. (2010). Outflow boundary conditions for 3D simulations of non-periodic blood flow and pressure fields in deformable arteries. *Computer methods in biomechanics and biomedical engineering*, 13(5), 625–640.

[45] Javadzadegan, A., Lotfi, A., Simmons, A., & Barber, T. (2015). Haemodynamic analysis of femoral artery bifurcation models under different physiological flow waveforms. *Computer Methods in Biomechanics and Biomedical Engineering*, 19(11), 1143–53.

[46] Appanaboyina, S., Mut, F., Löhner, R., Putman, C., & Cebral, J. (2009). Simulation of intracranial aneurysm stenting: Techniques and challenges. *Computer Methods in Applied Mechanics and Engineering*, 198(45-46), 3567–3582.

[47] Morbiducci, U., Gallo, D., Massai, D., Consolo, F., Ponzini, R., Antiga, L., Bignardi, C., Deriu, M. a., & Redaelli, A. (2010). Outflow conditions for image-based hemodynamic models of the carotid bifurcation: implications for indicators of abnormal flow. *Journal of biomechanical engineering*, 132(9), 091005.

[48] Kruse, R. R., Doomernik, D. E., Maltha, K. V., Kooloos, J. G., Kozicz, T. L., & Reijnen, M. M. (2017). Collateral artery pathways of the femoral and popliteal artery. *Journal of Surgical Research*, 211, 45–52.

[49] Westerhof, N., Bosman, F., De Vries, C. J., & Noordergraaf, A. (1969). Analog studies of the human systemic arterial tree. *Journal of biomechanics*, 2(2), 121–143.

[50] Gill, R. (1979). Pulsed Doppler with B-mode imaging for quantitative blood flow measurement. *Ultrasound in Medicine & Biology*, 5(3), 223–235.

[51] Willink, R. & Evans, D. H. (1995). Volumetric blood flow calculation using a narrow ultrasound beam. *Ultrasound in Medicine and Biology*, 21(2), 203–216.

[52] Womersley, J. R. (1955). Method for the Calculation of Velocity, Rate of Flow and Viscous Drag in Arteries when the Pressure Gradient is known. *Journal of Physiology*, 127, 553–563.

[53] McGah, P. M., Nerva, J. D., Morton, R. P., Barbour, M. C., Levitt, M. R., Mourad, P. D., Kim, L. J., & Aliseda, A. (2015). In vitro validation of endovascular Doppler-derived flow rates in models of the cerebral circulation. *Physiological Measurement*, 36(11), 2301–2316.

[54] Hussain, S. T., Wood, R. F. M., & Bland, M. (1996). Observer variability in volumetric blood flow measurements in leg arteries using duplex ultrasound. *Ultrasound in Medicine & Biology*, 22(3), 287–291.

[55] Morlacchi, S., Chiastra, C., Gastaldi, D., Pennati, G., Dubini, G., & Migliavacca, F. (2011). Sequential Structural and Fluid Dynamic Numerical Simulations of a Stented Bifurcated Coronary Artery. *Journal of Biomechanical Engineering*, 133(12), 121010.

[56] Yilmaz, F. & Gundogdu, M. Y. (2008). A critical review on blood flow in large arteries; relevance to blood rheology, viscoisty models and physiologic conditions. *Kore-Australia Rheology Journal*, 20(4), 197–211.

[57] Lee, S.-W. & Steinman, D. A. (2007). On the Relative Importance of Rheology for Image-Based CFD Models of the Carotid Bifurcation. *Journal of Biomechanical Engineering*, 129(2), 273.

[58] Morbiducci, U., Gallo, D., Massai, D., Ponzini, R., Deriu, M. A., Antiga, L., Redaelli, A., & Montevecchi, F. M. (2011). On the importance of blood rheology for bulk flow in hemodynamic models of the carotid bifurcation. *Journal of Biomechanics*, 44(13), 2427–2438.

[59] Gharahi, H., Zambrano, B. A., Zhu, D. C., DeMarco, J. K., & Seungik Baek, P. (2013). Computational fluid dynamic simulation of human carotid artery bifurcation based on anatomy and blood flow velocity measured with magnetic resonance imaging. *International Journal of Advances in Engineering Sciences and Applied Mathematics Computationa*, 8(1), 1–9.

[60] Kenner, T. (1989). The measurement of blood density and its meaning. *Basic Research in Cardiology*, 84(2), 111–124.

[61] Zingg, W., Sulev, J. C., & Morgan, C. D. (1970). Relationship between viscosity and hematocrit in blood of normal persons and burn patients. *Canadian journal of physiology and pharmacology*, 48(3), 202–205.

[62] Randles, A., Frakes, D. H., & Leopold, J. A. (2017). Computational Fluid Dynamics and Additive Manufacturing to Diagnose and Treat Cardiovascular Disease. *Trends in Biotechnology*, 35(11), 1049–1061.

[63] Esmaily-Moghadam, M., Bazilevs, Y., & Marsden, A. L. (2015). A bi-partitioned iterative algorithm for solving linear systems arising from incompressible flow problems. *Computer Methods in Applied Mechanics and Engineering*, 286, 40–62.

[64] Whiting, C. H. & Jansen, K. E. (2001). A stabilized finite element method for the incompressible Navier – Stokes equations using a hierarchical basis. *International Journal for Numerical Methods in Fluids*, 35(February 2000), 93–116.

[65] Esmaily Moghadam, M., Bazilevs, Y., Hsia, T. Y., Vignon-Clementel, I. E., & Marsden, A. L. (2011). A comparison of outlet boundary treatments for prevention of backflow divergence with relevance to blood flow simulations. *Computational Mechanics*, 48(3), 277–291.

[66] Marsden, A. L. & Esmaily-Moghadam, M. (2015). Multiscale Modeling of Cardiovascular Flows for Clinical Decision Support. *Applied Mechanics Reviews*, 67(3), 030804.

[67] Figueroa, C. A., Vignon-Clementel, I. E., Jansen, K. E., Hughes, T. J. R., & Taylor, C. A. (2006). A coupled momentum method for modeling blood flow in three-dimensional deformable arteries. *Computer Methods in Applied Mechanics and Engineering*, 195(41-43), 5685–5706.

[68] Kung, E. O., Les, A. S., Figueroa, C. A., Medina, F., Arcaute, K., Wicker, R. B., McConnell, M. V., & Taylor, C. A. (2011). In vitro validation of finite element analysis of blood flow in deformable models. *Annals of Biomedical Engineering*, 39(7), 1947–1960.

[69] Bertolotti, C., Qin, Z., Lamontagne, B., Durand, L.-G., Soulez, G., & Cloutier, G. (2006). Influence of multiple stenoses on echo-Doppler functional diagnosis of peripheral arterial disease: a numerical and experimental study. *Annals of biomedical engineering*, 34(4), 564–74.

[70] Varghese, S. S., Frankel, S. H., & Fischer, P. F. (2008). Modeling Transition to Turbulence in Eccentric Stenotic Flows. *Journal of Biomechanical Engineering*, 130(1), 014503.

[71] Pal, A., Anupindi, K., Delorme, Y., Ghaisas, N., Shetty, D. A., & Frankel, S. H. (2014). Large Eddy Simulation of Transitional Flow in an Idealized Stenotic Blood Vessel: Evaluation of Subgrid Scale Models. *Journal of Biomechanical Engineering*, 136(7), 071009.

[72] Tan, F. P. P. (2011). Comparison of LES of Steady Transitional Flow in an Idealized Stenosed Axisymmetric Artery Model With a RANS Transitional Model. *Journal of Biomechanical Engineering*, 133(5), 051001.

[73] Guess, W. P., Reddy, B. D., McBride, A., Spottiswoode, B., Downs, J., & Franz, T. (2017). Fluid-structure interaction modelling and stabilisation of a patient-specific arteriovenous access fistula. *ArXiv e-prints*.

[74] Esmaily-Moghadam, M., Bazilevs, Y., & Marsden, A. L. (2013). A new preconditioning technique for implicitly coupled multidomain simulations with applications to hemodynamics. *Computational Mechanics*, 52(5), 1141–1152.

[75] Lysenko, D. A., Ertesvåg, I. S., & Rian, K. E. (2013). Modeling of turbulent separated flows using openfoam. *Computers and Fluids*, 80(1), 408–422.

[76] Zhou, M., Sahni, O., Kim, H. J., Figueroa, C. A., Taylor, C. A., Shephard, M. S., & Jansen, K. E. (2010). Cardiovascular flow simulation at extreme scale. *Computational Mechanics*, 46(1), 71–72.

[77] Chen, Q., Smith, C. Y., Bailey, K. R., Wennberg, P. W., & Kullo, I. J. (2013). Disease location is associated with survival in patients with peripheral arterial disease. *Journal of the American Heart Association*, 2(5), 12–14.

[78] Frydrychowicz, A., Winterer, J. T., Zaitsev, M., Jung, B., Hennig, J., Langer, M., & Markl, M. (2007). Visualization of iliac and proximal femoral artery hemodynamics using time-resolved 3D phase contrast MRI at 3T. *Journal of Magnetic Resonance Imaging*, 25(5), 1085–1092.

[79] Barber, T. J. & Simmons, A. (2011). Large eddy simulation of a stenosed artery using a femoral artery pulsatile flow profile. *Artificial Organs*, 35(7), 155–160.

[80] Boersen, J. T., Groot Jebbink, E., Van de Velde, L., Versluis, M., Lajoinie, G., Slump, C. H., de Vries, J.-P. P. M., & Reijnen, M. M. P. J. (2017). The Influence of Positioning of the Nellix Endovascular Aneurysm Sealing System on Suprarenal and Renal Flow: An In Vitro Study. *Journal of Endovascular Therapy*, 24(5), 677–687.

[81] Thielicke, W. & Stamhuis, E. J. (2014). PIVlab - Towards User-friendly, Affordable and Accurate Digital Particle Image Velocimetry in MATLAB. *Journal of Open Research Software*, 2(1), e30.

[82] Paliwal, N., Damiano, R., Varble, N., Tutino, V., Dou, Z., Siddiqui, A., & Meng, H. (2017). Methodology for CFD Validation for Medical Use: Application to Intracranial Aneurysm. *Journal of Biomechanical Engineering*, 139.

[83] de Boer, S. W., Heinen, S. G., van den Heuvel, D. A., van de Vosse, F. N., & de Vries, J. P. (2017). How to define the hemodynamic significance of an equivocal iliofemoral artery stenosis: Review of literature and outcomes of an international questionnaire. *Vascular*, 25(6), 598–608.

[84] Young, D. (1979). Fluid mechanics of arterial stenosis. *Journal of Biomechanical Engineering*, 101, 157–175.

[85] Dodds, S. R. (2002). The haemodynamics of asymmetric stenoses. *European Journal of Vascular and Endovascular Surgery*, 24(4), 332–337.

[86] Novakova, L., Kolinsky, J., Adamec, J., Kudlicka, J., & Malik, J. (2016). Vascular stenosis asymmetry influences considerably pressure gradient and flow volume. *Physiological Research*, 65(1), 63–69.

[87] Reekers, J. A., Kromhout, J. G., & Jacobs, M. J. H. M. (1994). Percutaneous intentional extraluminal recanalisation of the femoropopliteal artery. *European Journal of Vascular Surgery*, 8(6), 723–728.

[88] Golchehr, B., Kruse, R., Van Walraven, L. A., Lensvelt, M. M., Zeebregts, C. J., & Reijnen, M. M. (2015). Three-year outcome of the heparin-bonded Viabahn for superficial femoral artery occlusive disease. *Journal of Vascular Surgery*, 62(4), 984–989.

[89] Lammer, J., Zeller, T., Hausegger, K. A., Schaefer, P. J., Gschwendtner, M., Mueller-Huelsbeck, S., Rand, T., Funovics, M., Wolf, F., Rastan, A., Gschwandtner, M., Puchner, S., Beschorner, U., Ristl, R., & Schoder, M. (2015). Sustained Benefit at 2-Years for Covered Stents Versus Bare-Metal Stents in Long SFA Lesions: The VIASTAR Trial. *CardioVascular and Interventional Radiology*, 38(1), 25–32.

[90] Weinstock, B. S. (2014). Covered stents in the treatment of superficial femoral artery disease. *Vascular Disease Management*, 11(4 PG - E76-E86), E76–E86.

[91] Marsden, A. L. (2014). Optimization in Cardiovascular Modeling. *Annual Review of Fluid Mechanics*, 46(1), 519–546.

[92] Hathcock, J. J. (2006). Flow effects on coagulation and thrombosis. *Arteriosclerosis, Thrombosis, and Vascular Biology*, 26(8), 1729–1737.

[93] Treiman, G. S., Ashrafi, A., & Lawrence, P. F. (2000). Incidentally detected stenoses proximal to grafts originating below the common femoral artery: Do they affect graft patency or warrant repair in asymptomatic patients? *Journal of Vascular Surgery*, 32(6), 1180–1189.

[94] Wyttenbach, R., Gallino, A., Alerci, M., Mahler, F., Cozzi, L., Di Valentino, M., Badimon, J. J., Fuster, V., & Corti, R. (2004). Effects of percutaneous transluminal angioplasty and endovascular brachytherapy on vascular remodeling of human femoropopliteal artery by noninvasive magnetic resonance imaging. *Circulation*, 110(9), 1156–1161.

[95] Votta, E., Le, T. B., Stevanella, M., Fusini, L., Caiani, E. G., Redaelli, A., & Sotiropoulos, F. (2013). Toward patient-specific simulations of cardiac valves: State-of-the-art and future directions. *Journal of Biomechanics*, 46(2), 217–228.

[96] Grbic, S., Mansi, T., Ionasec, R., Voigt, I., Houle, H., John, M., Schoebinger, M., Navab, N., & Comaniciu, D. (2013). Image-based computational models for TAVI planning: From CT images to implant deployment. In *Lecture Notes in Computer Science* (pp. 395–402).

[97] De Jaegere, P., De Santis, G., Rodriguez-Olivares, R., Bosmans, J., Bruining, N., Dezutter, T., Rahhab, Z., El Faquir, N., Collas, V., Bosmans, B., Verhegghe, B., Ren, C., Geleinse, M., Schultz, C., Van Mieghem, N., De Beule, M., & Mortier, P. (2016). Patient-Specific Computer Modeling to Predict Aortic Regurgitation after Transcatheter Aortic Valve Replacement. *JACC: Cardiovascular Interventions*, 9(5), 508–512.

[98] De Santis, G., Trachet, B., Conti, M., De Beule, M., Morbiducci, U., Mortier, P., Segers, P., Verdonck, P., & Verhegghe, B. (2013). A computational study of the hemodynamic impact of open- Versus closed-Cell stent design in carotid artery stenting. *Artificial Organs*, 37(7).

[99] Auricchio, F., Conti, M., De Beule, M., De Santis, G., & Verhegghe, B. (2011). Carotid artery stenting simulation: From patient-specific images to finite element analysis. *Medical Engineering and Physics*, 33(3), 281–289.

[100] Gundert, T. J., Marsden, A. L., Yang, W., & LaDisa, J. F. (2012). Optimization of Cardiovascular Stent Design Using Computational Fluid Dynamics. *Journal of Biomechanical Engineering*, 134(1), 011002.

[101] De Bock, S., Iannaccone, F., De Santis, G., De Beule, M., Van Loo, D., Devos, D., Vermassen, F., Segers, P., & Verhegghe, B. (2012). Virtual evaluation of stent graft deployment: A validated modeling and simulation study. *Journal of the Mechanical Behavior of Biomedical Materials*, 13, 129–139.

[102] Perrin, D., Badel, P., Orgeas, L., Geindreau, C., rolland du Roscoat, S., Albertini, J. N., & Avril, S. (2016). Patient-specific simulation of endovascular repair surgery with tortuous aneurysms requiring flexible stent-grafts. *Journal of the Mechanical Behavior of Biomedical Materials*, 63, 86–99.

[103] Sawicki, P. T., Kaiser, S., Heinemann, L., Frenzel, H., & Berger, M. (1991). Prevalence of renal artery stenosis in diabetes mellitus–an autopsy study. *Journal of internal medicine*, 229(6), 489–92.

[104] Textor, S. C., Misra, S., & Oderich, G. S. (2013). Percutaneous revascularization for ischemic nephropathy: The past, present, and future. *Kidney International*, 83(1), 28–40.

[105] Bommart, S., Cliche, A., Therasse, E., Giroux, M. F., Vidal, V., Oliva, V. L., & Soulez, G. (2010). Renal artery revascularization: Predictive value of kidney length and volume weighted by resistive index. *American Journal of Roentgenology*, 194(5), 1365–1372.

[106] Bruno, R. M., Daghini, E., Versari, D., Sgrò, M., Sanna, M., Venturini, L., Romanini, C., Di Paco, I., Sudano, I., Cioni, R., Lerman, L. O., Ghiadoni, L., Taddei, S., & Pinto, S. (2014). Predictive role of renal resistive index for clinical outcome after revascularization in hypertensive patients with atherosclerotic renal artery stenosis: A monocentric observational study. *Cardiovascular Ultrasound*, 12(1).

[107] van Brussel, P. M., van de Hoef, T. P., de Winter, R. J., Vogt, L., & van den Born, B.-J. (2017). Hemodynamic Measurements for the Selection of Patients With Renal Artery Stenosis. *JACC: Cardiovascular Interventions*, 10(10), 973–985.

[108] Udoff, E., Barth, K., Harrington, D., Kaufman, S., & White, R. (1979). Hemodynamic Significance of Iliac Artery Stenosis: Pressure Measurements During Angiography. *Radiology*, 132, 289–293.

[109] Murata, N., Aihara, H., Soga, Y., Tomoi, Y., Hiramori, S., Kobayashi, Y., Ichihashi, K., & Tanaka, N. (2015). Validation of pressure gradient and peripheral fractional flow reserve measured by a pressure wire for diagnosis of iliofemoral artery disease with intermediate stenosis. *Medical Devices: Evidence and Research*, 8, 467–472.

[110] Leach, J. R., Rayz, V. L., Soares, B., Wintermark, M., Mofrad, M. R., & Saloner, D. (2010). Carotid atheroma rupture observed in vivo and FSI-predicted stress distribution based on pre-rupture imaging. *Annals of Biomedical Engineering*, 38(8), 2748–2765.

[111] Teng, Z., Canton, G., Yuan, C., Ferguson, M., Yang, C., Huang, X., & Zheng, J. (2010). 3D Critical Plaque Wall Stress Is a Better Predictor of Carotid Plaque Rupture Sites Than Flow Shear Stress: An In Vivo MRI-Based 3D FSI Study. *Journal of Biomechanical Engineering*, 132(3), 031007.

[112] Huang, X., Yang, C., Zheng, J., Bach, R., Muccigrosso, D., Woodard, P. K., & Tang, D. (2014). Higher critical plaque wall stress in patients who died of coronary artery disease compared with those who died of other causes: A 3D FSI study based on ex vivo MRI of coronary plaques. *Journal of Biomechanics*, 47(2), 432–437.

[113] Groot Jebbink, E., Goverde, P. C. J. M., van Oostayen, J. A., Reijnen, M. M. P. J., & Slump, C. H. (2014). Innovation in aortoiliac stenting: an in vitro comparison. *Journal of Medical Imaging*, 9036, 90361X.

[114] Mills, J. L., Wixon, C. L., James, D. C., Devine, J., Westerband, A., & Hughes, J. D. (2001). The natural history of intermediate and critical vein graft stenosis: Recommendations for continued surveillance or repair. *Journal of Vascular Surgery*, 33(2), 273–280.

[115] Van Oostenbrugge, T. J., De Vries, J. P. P., Berger, P., Vos, J. A., Vonken, E. P., Moll, F. L., & De Borst, G. J. (2014). Outcome of endovascular reintervention for significant stenosis at infrainguinal bypass anastomoses. *Journal of Vascular Surgery*, 60(3), 696–701.

[116] Allon, M., Robbin, M. L., Young, C. J., Deierhoi, M. H., Goodman, J., Hanaway, M., Lockhart, M. E., & Litovsky, S. (2013). Preoperative venous intimal hyperplasia, postoperative

arteriovenous fistula stenosis, and clinical fistula outcomes. *Clinical Journal of the American Society of Nephrology*, 8(10), 1750–1755.

[117] Grechy, L., Iori, F., Corbett, R. W., Gedroyc, W., Duncan, N., Caro, C. G., & Vincent, P. E. (2017). The Effect of Arterial Curvature on Blood Flow in Arterio-Venous Fistulae: Realistic Geometries and Pulsatile Flow. *Cardiovascular Engineering and Technology*, 8(3), 313–329.

[118] Dawson, P. (2002). Contrast agents in patients on dialysis. *Seminars in Dialysis*, 15(4), 232–236.

[119] Chandra, S., Raut, S. S., Jana, A., Biederman, R. W., Doyle, M., Muluk, S. C., & Finol, E. A. (2013). Fluid-Structure Interaction Modeling of Abdominal Aortic Aneurysms: The Impact of Patient-Specific Inflow Conditions and Fluid/Solid Coupling. *Journal of Biomechanical Engineering*, 135(8), 081001.

[120] Indrakusuma, R., Jalalzadeh, H., Planken, R. N., Marquering, H. A., Legemate, D. A., Koelemay, M. J., & Balm, R. (2016). Biomechanical Imaging Markers as Predictors of Abdominal Aortic Aneurysm Growth or Rupture: A Systematic Review. *European Journal of Vascular and Endovascular Surgery*, 52(4), 475–486.

[121] Aggarwal, S., Qamar, A., Sharma, V., & Sharma, A. (2011). Abdominal aortic aneurysm: A comprehensive review. *Experimental and Clinical Cardiology*, 16(1), 11–15.

[122] Griffin, C. L., Scali, S. T., Feezor, R. J., Chang, C. K., Giles, K. A., Fatima, J., Huber, T. S., & Beck, A. W. (2015). Fate of aneurysmal common iliac artery landing zones used for endovascular aneurysm repair. *Journal of Endovascular Therapy*, 22(5), 748–759.

[123] Jones, J. E., Atkins, M. D., Brewster, D. C., Chung, T. K., Kwolek, C. J., LaMuraglia, G. M., Hodgman, T. M., & Cambria, R. P. (2007). Persistent type 2 endoleak after endovascular repair of abdominal aortic aneurysm is associated with adverse late outcomes. *Journal of Vascular Surgery*, 46(1), 1–8.

[124] Kruse, R. R., Vinke, E. J., Poelmann, F. B., Rohof, D., Holewijn, S., Slump, C. H., & Reijnen, M. (2016). Computation of blood flow through collateral circulation of the superficial femoral artery. *Vascular*, 24(2), 126–133.